NATIONAL INSTITUTE FOR FUSION SCIENCE

Contributions to 29th European Physical Society Conference
on Plasma Physics and Controlled Fusion
(Montreux, Switzerland, 17-21 June 2002)
from NIFS

(Received - July 1, 2002)

July 2002

RESEARCH REPORT
NIFS Series

TOKI, JAPAN

Contributions to 29th European Physical Society Conference on Plasma Physics and Controlled Fusion (Montreux, Switzerland, 17-21 June 2002) from NIFS

Abstract

. 22 contributed papers to the 29th European Physical Society Conference on Plasma Physics and Controlled Fusion (Montreux, Switzerland, 17-21 June 2002) from the activity of NIFS are collected in this report.

P-1.073	J.Miyazawa	Global Confinement Characteristics of Neon Plasmas in LHD
P-1.074	R.Sakamoto	Ablation and Subsequent Density Redistribution of Fueling Pellets Injected into LHD Plasmas
P-1.075	H.Yamada	Energy Confinement and Heat Transport in Extended High Density Regime of NBI Heated Plasmas on LHD
P-1.076	Y.Takeiri	High-Energy and High-Power NBI Heating Experiments in LHD
P-1.077	H.Funaba	Transport Analysis of ECH Overlapped NBI Plasmas in LHD
P-1.078	K.Yamazaki	Experimental Analysis and Predictive Simulation of Transport Barrier in LHD and CHS Plasmas
P-1.079	S.Yamamoto	Energetic Ion Driven MHD Instabilities in High Beta LHD Plasmas
P-1.080	Y.Narushima	Study of Ideal External Mode in LHD
P-1.083	M.Osakabe	Redistribution of Energetic Particles by MHD bursts on Large Helical Device
P-1.102	J.F.Lyon	Spatially Resolved Measurements of Energetic Neutral Particle Distributions in the Large Helical Device
P-1.126	N.Tamura	Impurity Transport Study by Means of Tracer-Encapsulated Solid Pellet in LHD
P-2.120	V.Y.Sergeev	Evaluations of the Optimal Pellet Injection Parameters and Expected Detector Signals for the PCX Diagnostics on LHD
P-4.010	M.Y.Tanaka	Formation of Dissipative Vortex and Anomalous Viscosity in a Rotating Plasma
P-4.012	S.Yoshimura	Potential Structure and Quasi-neutrality Breaking of Plasma Hole
P-4.061	K.Toi	Transport Studies of Dimensionally-Similar Low-Energy-Density Plasmas in CHS Heliotron/Torsatron
P-4.065	T.Ozaki	Spatial Distribution of High-Energy Particle on NBI and ECH Plasmas of Large Helical Device
P-4.086	S.Okamura	Equilibrium and Boundary Structure of Quasi-axisymmetric Stellarator CHS-qa
P-5.039	S.Toda	Theoretical Study of Structure and Dynamics of Radial Electric Field in Helical Plasmas
P-5.052	K.Matsuoka	Prospect of Strongly Inward Shifted Configuration in CHS
P-5.059	H.Sugama	Kinetic and Fluid Simulations of the Collisionless Slab Ion Temperature Gradient Driven Turbulence
P-5.064	R.Kumazawa	Parameter Range of ICRF Heated Plasmas on Large Helical Device
P-5.096	Y.Liu	Two Dimensional Soft X-ray and AXUVD Tomography Based on Magnetic Flux Surfaces

Global Electron Energy Confinement of Neon Plasmas in LHD

J. Miyazawa, H. Yamada, S. Morita, Y. Takeiri, M. Osakabe, K. Narihara, K. Tanaka,

S. Sakakibara, M. Goto, S. Murakami, R. Sakamoto, B.J. Peterson, K. Ida, O. Kaneko,

K. Kawahata, A. Komori, Y. Nakamura, N. Ohyabu, and LHD experimental Group

National Institute for Fusion Science, 322-6 Oroshi-cho, Toki, Gifu 509-5292, Japan

Neon gas puff experiment has been performed on the Large Helical Device (LHD), to investigate the effect of electric charge and mass of plasma ions on the energy confinement property. Here, we focus on the global energy confinement of electrons in the plasmas heated by the neutral beam (NB) injection. The major radius of the magnetic axis, R, and the plasma minor radius, a, are fixed to 3.6 m and 0.62 m, respectively. Meanwhile, the magnetic field strength at the plasma center, B_0, is changed from 1.5 T to 2.893 T.

The relation between the electron (ion) temperature at the plasma center, T_{e0} (T_{i0}), and the volume averaged electron density, $<n_e>$, is plotted in Fig. 1 (a) (Fig. 1 (b)). Only the hydrogen (or the neon) gas is puffed into plasmas denoted as 'hydrogen' (or, 'neon') plasmas. The highest T_{e0} is obtained in the neon plasmas, although the difference from the hydrogen data is not remarkable. As for the T_{i0}, which is plotted in Fig. 1 (b), there is a significant difference between the hydrogen plasmas and the neon plasmas; i.e. T_{i0} of the neon plasmas is more than 1.5 times higher than that of the hydrogen plasmas, in the high B_0 case. In Fig. 1 (c), drawn is the $<n_e>$ dependence of the electron-stored energy, W_{e_kin}, which is estimated from the profiles of $T_e(\rho)$ and $n_e(\rho)$, where $\rho = r/a$ is the normalized radius. The energy confinement time of the helical plasmas usually exhibits the positive dependence on density as summarized in the international stellarator scaling 95 (ISS95) [1]. In the experiment, the positive density dependence of W_{e_kin} can be recognized only in the low-density regime of $<n_e> < 2 \times 10^{19}$ m^{-3} (see Fig. 1 (c)). This 'saturation' of the global confinement in the high-density regime is not fully understood at this moment. In this study, however, our interest lies in the difference between the hydrogen plasmas and the neon plasmas. Therefore, we restrict the density range as $<n_e> < 2 \times 10^{19}$ m^{-3} in the analysis below, to eliminate the saturated data.

In LHD, negative-ion based NB injection systems are adopted and the energy of the beam ions, E_{NB}, is much larger than T_e (typically, $E_{NB} > 150$ keV). This results in the large fraction of the electron heating power, P_{NB_e}, of about 0.8 P_{NB}. Here, 'pure' plasmas are assumed for both of the hydrogen ($Z_{eff} = 1$) and the neon ($Z_{eff} = 10$), to give P_{NB_e}. As seen in Fig. 1 (a) and (b), $T_{i0} < T_{e0}$ is observed in the low-density hydrogen plasmas, and therefore
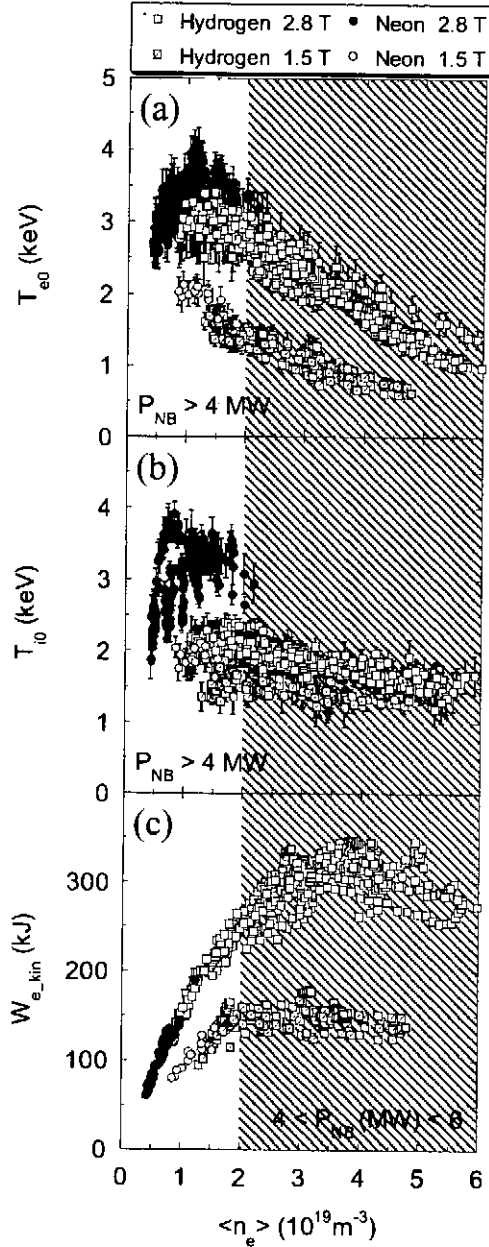
□ Hydrogen 2.8 T • Neon 2.8 T
□ Hydrogen 1.5 T ○ Neon 1.5 T

(a)

T_{e0} (keV)

$P_{NB} > 4$ MW

(b)

T_{i0} (keV)

$P_{NB} > 4$ MW

(c)

W_{e_kin} (kJ)

$<n_e> (10^{19} m^{-3})$

Fig. 1. Distributions of (a) T_{e0}, (b) T_{i0}, and (c) W_{e_kin}, with respect to $<n_e>$.

□ Hydrogen 2.8 T • Neon 2.8 T
□ Hydrogen 1.5 T ○ Neon 1.5 T

T_{e0} (keV)

$P_{NB\_e} / <n_e>$ (MW/$10^{19} m^{-3}$)

Fig. 2. Dependence of T_{e0} on $P_{NB\_e} / <n_e>$. Plotted are the data that satisfy the two criteria; $<n_e> < 2 \times 10^{19} m^{-3}$, and $P_{ei} / P_{NB} < 0.1$.

the heat transfer from the electrons to the ions, P_{ei}, should be considered carefully. The maximum P_{ei} reaches to 1 MW at $<n_e> < 2 \times 10^{19}$ m^{-3} and is not small enough to be neglected. Hereinafter, we eliminate the data that has $P_{ei} / P_{NB} > 0.1$, and neglect P_{ei} to reduce its influence.

The relation between T_{e0} and the electron heating power per an electron, $P_{NB\_e} / <n_e>$, is plotted in Fig. 2. In the range of $P_{NB\_e} / <n_e> < 5$ MW / 10^{19} m^{-3}, T_{e0} increases with $P_{NB\_e} / <n_e>$, and any particular differences between the hydrogen and the neon plasmas can be recognized. The maximum T_{e0} obtained in the neon plasmas can be attributed to the increased heating power due to the small fraction of the NB shine-through power at the low-density regime. Above $P_{NB\_e} / <n_e> > 5$ MW / 10^{19} m^{-3}, however, T_{e0} gradually decreases. The reason why this kind of deterioration occurs is not solved to date. Hereinafter, we adopt one more criterion to eliminate the deteriorated data; i.e. $P_{NB\_e} / <n_e> < 5$ MW / 10^{19} m^{-3}.

Next, we compare the global energy confinement of the electrons in the hydrogen and

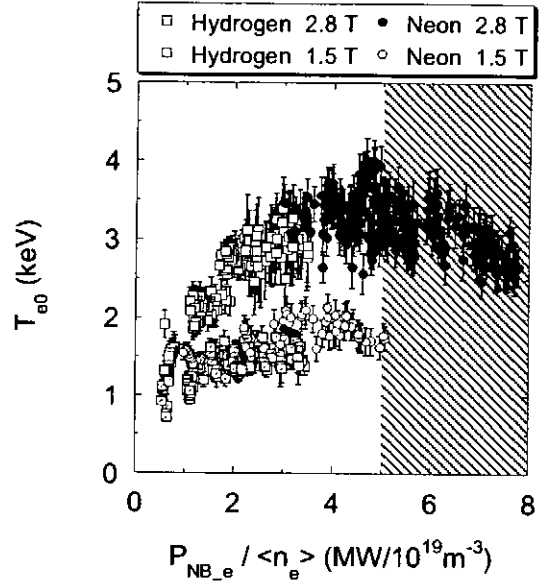the neon plasmas. The non-dimensional regression analysis of the experimental electron energy confinement time, $\tau_{E\_e}^{exp}$ ($\equiv W_{e\_kin} / P_{NB\_e}$) is examined. In the non-dimensional form, $\tau_{E\_e}^{exp}$ can be expressed as

$$\tau_{E\_e}^{exp} \, \Omega_e \propto B_0 \, \tau_{E\_e}^{exp} \propto (\rho_e{}^*)^\phi (\nu^*)^\gamma (\beta_e)^\eta, \tag{1}$$

where Ω_e is the electron gyro frequency, $\rho_e{}^* = \rho_e / a$ is the normalized electron gyro radius, ν^* is the collisionality, and β_e is the normalized electron pressure [2]. For the hydrogen data, however, the linear correlation coefficients of each components are 0.89, 0.35 and 0.54 for $\rho_e{}^*$, ν^*, and β_e, respectively. Here, we neglect the dependence on ν^* and β_e, since these are not strongly correlating with $\tau_{E\_e}^{exp}$. Regression analysis with $\rho_e{}^*$ alone gives;

$$B_0 \, \tau_{E\_e}^{exp} (H) = 3.57 \times 10^{-13} \, (\rho_e{}^*)^{-2.74 \pm 0.07}. \tag{2}$$

As for the neon data, the linear correlation coefficients for each components are 0.91, 0.49 and 0.27 for $\rho_e{}^*$, ν^*, and β_e, respectively. Again, ν^* and β_e are not strongly correlating with $\tau_{E\_e}^{exp}$. Regression analysis with $\rho_e{}^*$ alone results in

$$B_0 \, \tau_{E\_e}^{exp} (Ne) = 1.15 \times 10^{-12} \, (\rho_e{}^*)^{-2.61 \pm 0.09}. \tag{3}$$

In both of the hydrogen and the neon plasmas, $B_0 \, \tau_{E\_e}^{exp}$ is strongly related to $\rho_e{}^*$ and the exponents are identical within the standard deviations. These relations are plotted in Fig. 3 (a). This suggests that both plasmas have similar parameter dependence of the global electron energy confinement. The difference in the coefficients between Eqs. (2) and (3) is possibly due to the small $\rho_e{}^*$ of $\sim 10^{-4}$ (note that even the small difference of 0.1 in the exponents causes an error of factor 2.5 in the coefficients). To compare the coefficients more accurately, we assume a model equation with the exponent of -2.7;

$$\tau_{E\_e}^{fit} \, \Omega_e \propto B_0 \, \tau_{E\_e}^{fit} \propto (\rho_e{}^*)^{-2.7}. \tag{4}$$

In the gyro-Bohm model, where micro-turbulences are considered as the cause of the anomalous energy transport [3, 4], the exponent of -3 is assumed, while it is -2 in the Bohm model, for example (note that $\rho_i{}^*$ is used instead of $\rho_e{}^*$, in these models). Equation (4) can be rewritten using the conventional terms as below;

$$\tau_{E\_e}^{fit} = C_0 \, a^{2.30} R^{0.574} B_0^{0.723} P_{NB\_e}^{-0.574} <n_e>^{0.574}, \tag{5}$$

where C_0 is the fitting parameter, and the units of each terms are; m, m, T, MW, and $10^{19} \, m^{-3}$, for a, R, B_0, P_{NB_e}, and $<n_e>$, respectively. Fitting the data with Eq. (5), the distributions of
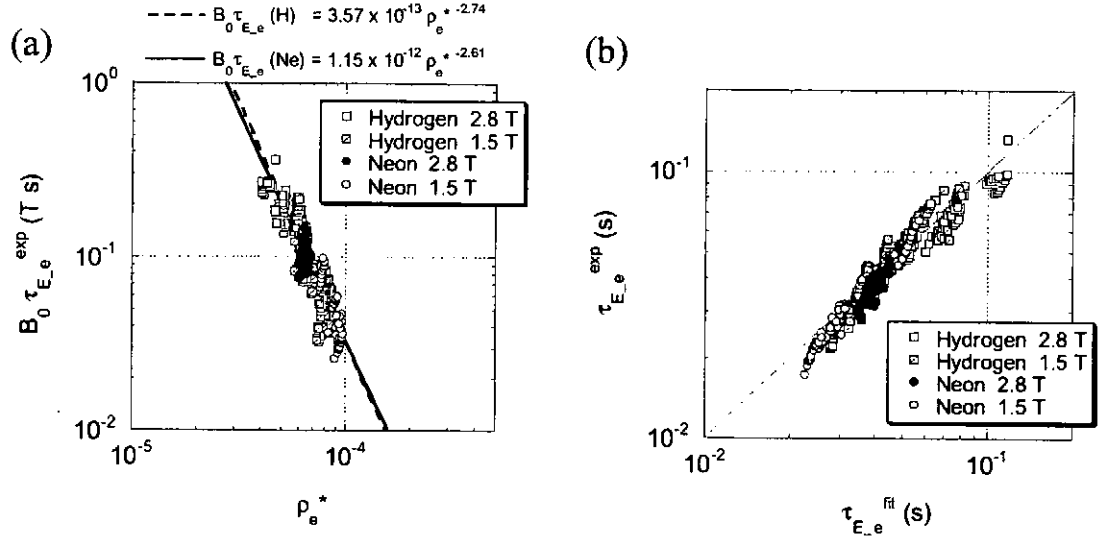
Fig. 3. (a) Dependence of $B_0\ \tau_{E\_e}^{exp}$ on $\rho_e{}^*$, and (b) the comparison of $\tau_{E\_e}^{exp}$ and $\tau_{E\_e}^{fit}$. Plotted are the data that satisfy the three criteria; $<n_e> < 2 \times 10^{19}\,\mathrm{m}^{-3}$, $P_{ei} / P_{NB} < 0.1$, and $P_{NB\_e} / <n_e> < 5\,\mathrm{MW} / 10^{19}\,\mathrm{m}^{-3}$.

$\tau_{E\_e}^{exp}$ in the plasmas with different ion species can be compared. Using hydrogen dataset, $C_0 = 0.060\pm0.007$ is obtained, while $C_0 = 0.056\pm0.004$ is obtained with the neon dataset. In both cases, C_0 is identical within the standard deviations. Assuming $C_0 = 0.06$, $\tau_{E\_e}^{exp}$ and $\tau_{E\_e}^{fit}$ are compared in Fig. 3 (b). As is seen in the figure, $\tau_{E\_e}^{fit}$ well reproduces $\tau_{E\_e}^{exp}$, and its absolute value is similar in both of the hydrogen and the neon plasmas.

These results are contrastive to the Z-mode [5] and the RI-mode [6] in tokamaks, where a reduction of the electron thermal diffusivity induced by the impurity (including the neon) gas puff has been observed. In this study, however, parameter region is limited. Especially, the confinement deterioration at $P_{NB\_e} / <n_e> > 5$ MW / $10^{19}\,\mathrm{m}^{-3}$ is observed only in the neon plasmas. Whether this deterioration will also occur in the hydrogen plasmas, or not, should be examined in the future experiment. The energy confinement of the ions has not been treated in this study. To carry out the conclusive discussion on this, it is necessary to measure the ion temperature profile and the ion density profile.

References

[1] U. Stroth et al., Nucl. Fusion 36, 1063 (1996).

[2] H. Yamada et al., Plasma Phys. Control. Fusion 43, A55 (2001).

[3] R. J. Goldston et al., Bull. Am. Phys. Soc. 34, 1964 (1989).

[4] M. Murakami et al., Phys. Fluids B 3, 2261 (1991).

[5] E. A. Lazarus et al., Nucl. Fusion 25, 135 (1985).

[6] G. R. McKee et al., Phys. Plasmas 7, 1870 (2000).

Ablation and Subsequent Density Redistribution

of Fueling Pellets Injected into LHD Plasmas

R. Sakamoto, H. Yamada, K. Tanaka, K. Narihara, P.T. Lang[1], L.R. Baylor[2], S.K. Combs[2],

P.W. Fisher[2], O. Kaneko, A. Komori, O. Motojima and LHD experimental group

National Institute for Fusion Science, Japan
[1]*Max-Planck-Institut für Plasmaphysik, EURATOM Association, Germany*
[2]*Oak Ridge National Laboratory, USA*

1. Introduction

Pellet fueling has extended the operational region of the Large Helical Device (LHD) plasmas to higher densities, which cannot be attained by gas puffing while maintaining favorable dependence of the energy confinement on the density. However, deterioration of the effective fueling efficiency was observed with increasing heating power and/or plasma temperature. Our previous study has made it clear that the deterioration is due to fast time scale (within several 100 μs) outward density redistribution just after pellet ablation[1]. Similar deterioration is observed in tokamaks with the magnetic low-field-side (LFS) pellet injection, but significant improvement in fueling efficiency has been demonstrated with the magnetic high-field-side (HFS) pellet injection[2][3] in recent tokamak study. The mechanism for the improvement is not yet elucidated but could be caused by an E×B drift that arises from a vertical polarization of ablation cloud due to a ∇B and curvature drift[4]. This tokamak's success motivated studies to optimize injection location on LHD. Noticing the difference between tokamak and LHD on the magnetic structure, pellet injection experiments from the different locations have been carried out on LHD for the purpose of investigating effect of the magnetic structure on the density redistribution.

2. Magnetic Field Structure and Pellet Injection Locations

Experiments were carried out on LHD, a heliotron type magnetic confinement device with continuous winding super-conducting coils. The major radius, averaged minor radius,
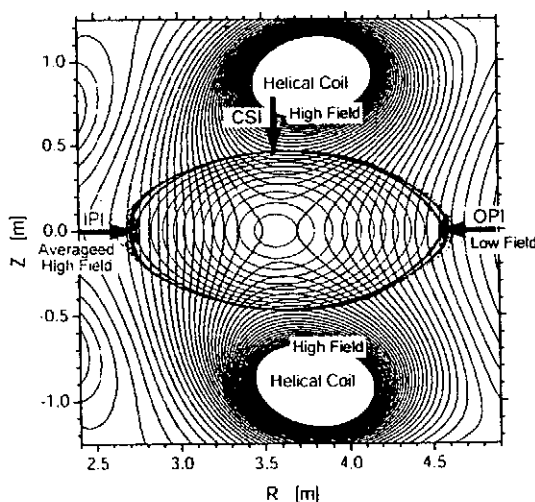

Fig. 1 Magnetic field structure and schematic view of pellet injection location in LHD.

magnetic field and plasma volume are 3.9 m, 0.6 m, 2.9 T and 30 m³, respectively. Because the external coils, namely, a pair of helical coils establish magnetic confinement field, there are the following remarkable magnetic structures on LHD, (1)Fully negative shear and large rotational transform (q<1) at the plasma boundary, (2)saddle point of the magnetic field exist in the plasma center, (3)two kind of the HFS can be defined, i.e. the toroidal averaged-HFS and the local-HFS.

The injection locations are shown in fig. 1. The OPI (outer port injection) is injection from the torus outside and equal to the LFS on tokamak. The IPI (inner port injection) is injection from the averaged-HFS. CSI (coil side injection) is injection from the local-HFS. Typical pellet speed is 1200 m/s at conventional OPI, but because the pellet speed is limited in the curved guide tubes, only slow (up to 300 m/s)[5] pellet injection is available at alternative injection. Specially modified injector with mechanical punch was employed for slow pellets acceleration.

3. Experimental Results and Discussion

Typical temporal changes of electron density and ablation light (H$_\alpha$ intensity) for the high speed OPI case are shown in fig. 2. Line averaged electron density is divided into two part, core density $\bar{n}_e^{core}$ (ρ<0.7) and boundary density $\bar{n}_e^{boundary}$ (ρ>0.7), using multi-chord interferometer. The densities increase during ablation, and then core density begins to decrease just after pellet ablation, whereas boundary density increases continuously. This behavior suggests density redistribution of the core into boundary. The time scale of such density redistribution is several 100 μs.

Predictive pellet deposition profile, which is calculated from the NGS model using ABLATE code[6], is shown in fig. 3. As for alternative injection with slow pellets, a penetration depth of the pellet is shallower than high speed OPI. A temporal changes of electron density and
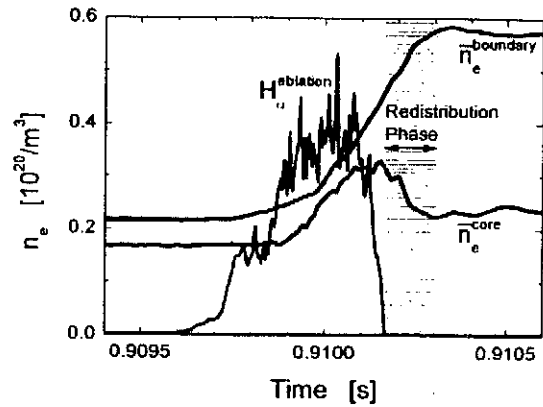

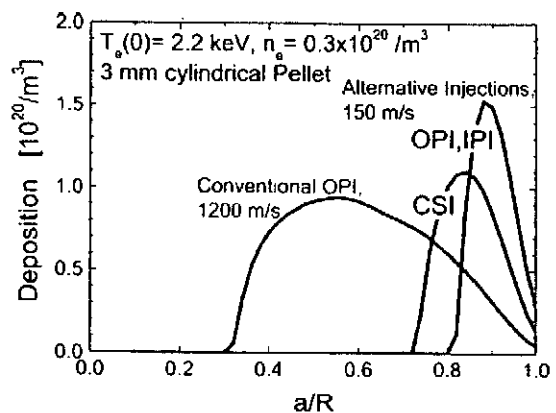Fig. 2 Temporal changes of electron density and H$_\alpha$ intensity at the high speed OPI case.
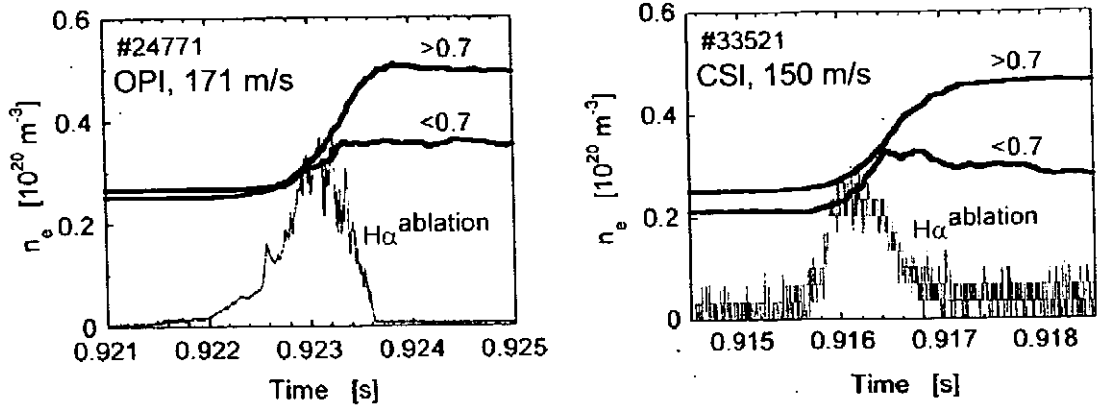

Fig. 3 Predictive penetration depth from the NGS model.

Fig. 4 *Temporal changes of the electron density and H_α intensity at the low speed OPI and CSI.*

ablation light (H_α intensity) for the CSI and OPI are shown in fig. 4. The penetration depths, which are estimated by duration of H_α emission from the ablating pellet, are 0.28 m (OPI) and 0.18 m (CSI). Considering the ablation in an elgodic layer, this penetration depth is consistent with the predicted value from the NGS models. Looking at the contour plot of the magnetic field intensity on poloidal section (fig. 1), OPI and CSI are obviously different from each other in the gradient of the magnetic field. From the direction of ∇B, we have expected preferable density redistribution on CSI case. However the evident density redistribution is not observed on CSI. Though this result is quite different from the behavior in tokamaks, we tried to understand this result from the viewpoint of the E×B drift model.

In consideration of the axis asymmetric field structure on LHD, E×B drift direction on the field line was calculated. For the qualitative discussion, only direction of vector was calculated,

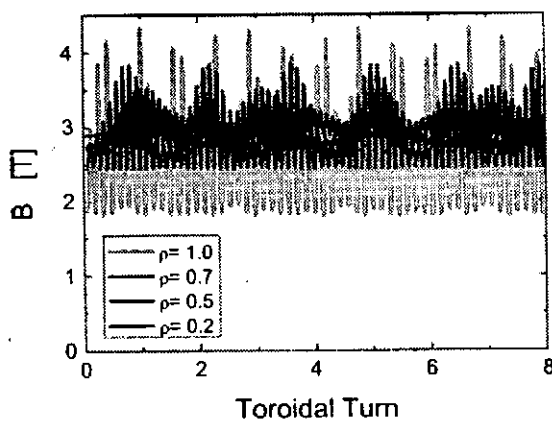***Fig. 5*** *Plot of the magnetic field strength versus toroidal turn on the flux surface of $\rho=1.0$, 0.7, 0.5, 0.2.*
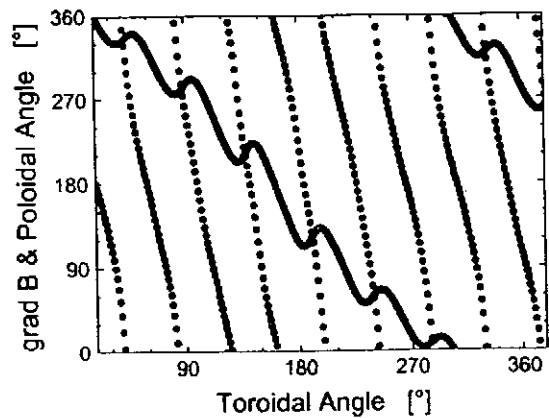
Fig. 6 *Plot of the ∇B direction (same definition as poloidal angle) and poloidal angle versus toroidal angle on the flux surface of $\rho=0.9$.*

i.e. $\mathbf{E} \times \mathbf{B} \simeq -c(\mathbf{B} \times \nabla B) \times \mathbf{B} = -\nabla B$. Fig. 5 shows a plot of the magnetic field strength versus the toroidal turn on the flux surface of ρ=1.0, 0.7, 0.5, 0.2. Due to helical coils, there are helical ripples and large rotational transform at the plasma boundary region where the slow pellet ablates. Therefore the magnetic field strength alternate drastically with short period, while these effect become moderate in the core region of the plasma. The ∇B direction and poloidal angle at the point along the field line that begins at the ablation region of the slow pellet (ρ=0.9), is shown in fig. 6. ∇B makes 9 revolutions during one toroidal turn, i.e. direction of the ∇B polarization alternates with each 1 m moving of the pellet cloud along the field line. Therefore electric field, which drives the density redistribution, cannot be formed sufficiently in the pellet cloud. In addition, large rotational transform rapidly even out the influence of injection location on the density redistribution. Thus the density redistribution behavior on LHD can be understood qualitatively from the ExB drift model.

As for high speed OPI case, helical ripples and rotational transform at the ablation region are relatively small since the pellet ablates in the core region. Thus similar density redistribution to tokamaks could be observed.

4. Summary

Pellet injection experiments from the different locations have been carried out on LHD. Obviously density redistribution that observed in the high speed pellet case did not appear in any alternative pellet injection case. The result looks different from tokamaks, however the behavior could be understood qualitatively from the same ExB drift model.

Reference

[1]R. Sakamoto, et al., Nuclear Fusion, 41 (2001) 381.

[2]P.T. Lang, et al., Physical Review Letters, 79 (1997) 1487.

[3]L.R. Baylor, et al., Fusion Technology, 34 (1998) 425.

[4]P.B. Parks, et al., Physics of Plasmas, 7 (2000) 1968.

[5]S.K. Combs, et al. Fusion Engineering and Design 58-59 (2001) 343.

[6]Y. Nakamura, et al., Nuclear Fusion, 26 (1986) 907.

Energy Confinement and Heat Transport
in Extended High Density Regime of NBI Heated Plasmas on LHD

H.Yamada, S.Murakami, R.Sakamoto, J.Miyazawa, S.Morita, K.Y.Watanabe, K.Narihara,

K.Tanaka, S.Sakakibara, B.J.Peterson, K.Ida, M.Osakabe, S.Inagaki, S.Masuzaki,

G.Rewoldt[1], H.Sugama, O.Kaneko, K.Kawahata, A.Komori, Y.Nakamura, T.Mutoh,

N.Ohyabu, K.Yamazaki, O.Motojima, LHD Experimental Group

National Institute for Fusion Science, Toki, Gifu 509-5292, Japan
1 Princeton Plasma Physics Laboratory, Princeton, NJ 08544, USA

1.Introduction

Confinement studies of net current free plasmas have progressed due to the recent LHD experiments with upgraded heating capability up to 9 MW of NBI. Significant density dependence of the energy confinement time as described in the ISS95 scaling [1] has been demonstrated [2,3] in the extended parameter regimes in LHD. When the plasma profiles are fixed, the density dependence of the energy confinement time, i.e., $\tau_E \propto (\bar{n}_e / P)^{0.6}$ or $\tau_E \propto (\bar{n}_e / P)^{0.5}$ can be interpreted by the gyro-Bohm local heat conduction as $\chi \propto T^{3/2}$ or the Bohm as $\chi \propto T$, respectively. The favorable density dependence observed in LHD is of importance with the prospect of net current-free plasmas with high confinement and high β due to high density operation. Since the density dependence of the global confinement and the temperature dependence of the local transport are two sides of the same physical mechanism, it is also attracting much interest to the physics issue of anomalous transport. However, the existence of this kind of density dependence and its disappearance have been reported from many toroidal experiments. Recent experiments employing a wide range of heating power in LHD also have indicated that the favorable density dependence saturates at
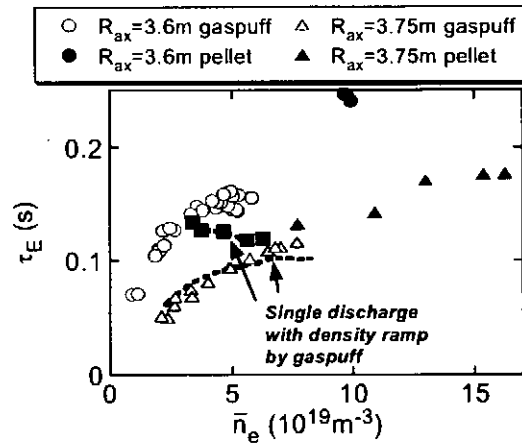

Fig.1 Dependence of energy confinement time on density in the density scan with fixed heating power. Open and Solid symbols denote gas-fueled and pellet-fueled discharges, respectively. Circles and triangles are the cases with Rax=3.6 m and 3.75 m, respectively. Dashed lines : time traces of single discharges with density ramp-up. The heating power is fixed at 4.5 MW and 3.6 MW in the cases with R_{ax}=3.6m and R_{ax}=3.75m, respectively.

a certain density under specific conditions. This paper discusses the cause of this saturation and related characteristics of anomalous transport. Through this study, the response of temperature profile to the heat deposition profile is highlighted, which is contrasted to the concept of *stiffness* or *profile consistency* observed in tokamaks.

2. Experimental Results

Although confinement improvement by shifting the magnetic axis inward has been demonstrated in previous work [2], saturation of the energy confinement time with the increase in density has been observed in gas-fueled NBI-heated plasmas, particularly, with this inward shifted configuration with R_{ax}=3.6 m. Open circles in Fig.1 shows the data in the density flat phase for a series of density scan with the fixed heating power of 4.5MW in the case with R_{ax}=3.6m . The energy confinement time does not increase anymore above $4 \times 10^{19} m^{-3}$. The energy confinement time is derived from the stored energy measured by the diamagnetic loop and the absorbed heating power estimated from the direct measurement of the shine-through power [4] and the Monte-Carlo calculation [5]. Excess gas-puffing to increase density shrinks the plasma and consequently degrades the performance; however, the saturation of the energy confinement has been found well below this condition. The saturated state can be sustained in a quasi-steady state and radiation loss does
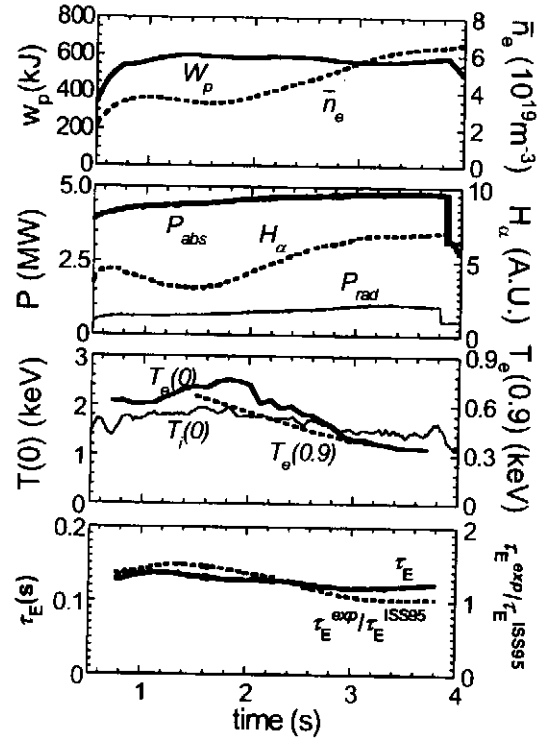

Fig.2 Waveforms of the discharge with density ramp-up. The working gas is hydrogen. Top:Stored energy and line averaged density. 2nd:Absorbed power of NBI, total radiation power, and $H\alpha$ emission. 3rd: The electron temperatures at the center and $\rho=0.9$ measured by the multi-channel Thomson scattering system, and the ion temperatures measured by the crystal spectrometer (Ti XXI). Bottom: Energy confinement time and improvement factor on ISS95.

not play an essential role. The saturation density does not depend on the heating power significantly and shows a weak dependence on the magnetic field strength. The saturation or degradation of confinement is distinguished in the density ramp-up phase by gas-puffing in a single discharge with R_{ax}=3.6 m. The discharge shown in Fig.2 corresponds to the closed squares in Fig.1 with time slices every 0.5s. The line averaged density is doubled from t = 1.5 s to 4.0 s, however, the stored energy and the energy confinement time do not change.

The improvement factor on ISS95 is degraded from 1.6 to 1. The ratio of the radiation power to the absorbed power increases from 16 % to 22 %. Although temperatures decrease with the increase in density, the ratio of decrease of electron temperature is more distinguished in the center than in the edge. Ion temperature is reduced more gradually because of stronger equi-partition of energy with electrons in the higher density regime. The temporal changes of the density and temperature profiles are shown in Fig.3. The density profile remains flat during the ramp-up and the electron temperature becomes broad.

The high density operation prevents the deep penetration of tangentially injected neutral beams and heat deposition moves from the core to the periphery (see Fig.4(a)). This tendency is emphasized with

Fig.3 Left (a): Temporal change of density profile in the discharge with $R_{ax}=3.6$ m illustrated in Fig.2. Right (b): Temporal change of temperature profile.

Fig.4 Left (a) : Profile of power deposition from NBI in the discharge illustrated in Fig.2 with $R_{ax}=3.6m$. Right (b) : Temperature dependence of thermal diffusivity at two radii of $\rho=0.5$ (open circles) and $\rho=0.9$ (solid circles) derived from the power balance analysis of 5 time slices.

the inward-shifted magnetic axis due to the tangent radius of 3.7 m of the NBI beam lines and the broad density profile due to gas-puffing particularly in the ramp-up phase. The local heat transport is investigated for time slices in the density ramp-up phase with $R_{ax}=3.6m$. Although the density dependence going as $\tau_E \propto \bar{n}_e^{0.6}$ is lost completely, the local heat conduction coefficient shows a clear temperature dependence with the power of 1.0 to 1.6 (see Fig.4(b)). Although the discussion whether Bohm or gyro-Bohm it is requires clarification of the dependence on the magnetic field strength, the essential point is that the apparent contradiction between the global confinement and the local transport can be attributed to the change of the heat deposition profile.

In contrast to the case with $R_{ax}=3.6m$, the density dependence of gas-fueled plasmas is sustained in the high density regime close to the detachment of the plasma in the case with $R_{ax}=3.75m$ (see triangles in Fig.1). The degradation due to the density ramp-up is not so distinguished as in $R_{ax}=3.6m$. The heat deposition profile is insensitive to density itself as
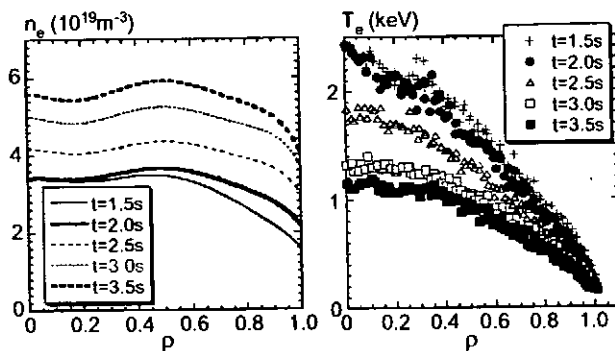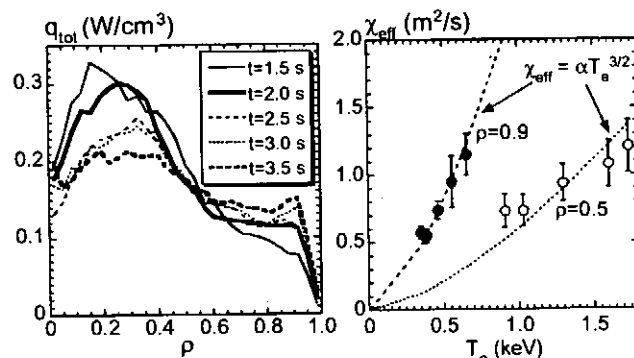
well as its profile (see Fig.5(a)) in this case. The thermal diffusivity shows a clear the temperature dependence as in the case with R_{ax}=3.6m, which is consistent with the behavior of the energy confinement time because of the unchanged heat deposition profile.
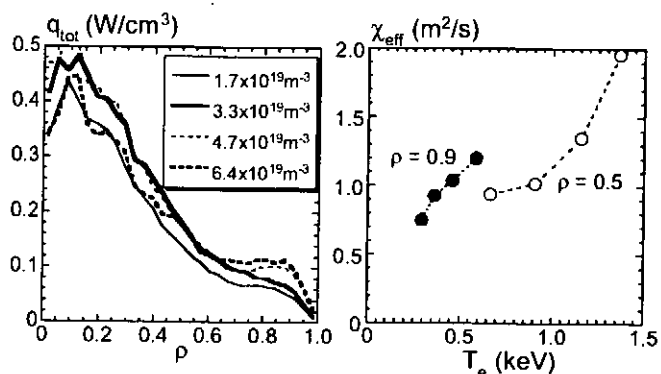
3. Discussions and Conclusions

Major part of an apparent contradiction between the global

Fig.5 Left (a) : Profile of power deposition from NBI in the discharges in the case with R_{ax}=3.75m. Righ t(b) : Temperature dependence of thermal diffusivity at two radii of ρ=0.5 (open circles) and ρ=0.9 (solid circles) derived from the power balance.

energy confinement time and local thermal diffusivity, which has been observed in the case with R_{ax}=3.6m, can be explained by the broadening of heat deposition. These observations indicate that the temperature profile changes straight-forwardly according to the heat deposition profile of the net current free plasmas in LHD. The apparent discrepancy between the global and the local transports suggests that the central heating improves the saturated state. The favorable density dependence can be extended towards much higher density by pellet fueling (see closed circles and triangles in Fig.1)[6] in both cases of R_{ax}=3.6 m and 3.75 m. The peaked density profile realized by pellet fueling promotes the core heating and recovers the intrinsic density dependence when the density is moderate. However, the peripheral heat deposition becomes predominant even in the peaked density profile by pellet injection above $8 \times 10^{19} m^{-3}$, therefore, other mechanism related to confinement improvement is prerequisite to explain the advantage of pellet injection.

References

[1] U.Stroth, M.Murakami, H.Yamada et al., Nucl. Fusion 36 (1996) 1063.

[2] H.Yamada, K.Y.Watanabe, K.Yamazaki et al., Nucl. Fusion 41 (2001) 901.

[3] H.Yamada, A.Komori, N.Ohyabu et al., Plasma. Phys. Control. Fusion 43 (2001) A55.

[4] M Osakabe et al., Rev. Sci. Instrum. 72, 590 (2001)

[5] S.Murakami et al 1995 Trans. Fusion Technol. 27 (1995) 256

[6] R.Sakamoto, H.Yamada, K.Tanaka et al., Nucl. Fusion 41 (2001)381.

High-Energy and High-Power NBI Heating Experiments in LHD

Y. Takeiri, M. Osakabe, K. Ikeda, O. Kaneko, K. Tsumori, Y. Oka, K. Nagaoka,
T. Shimozuma, S. Kubo, S. Morita, M. Yokoyama, H. Funaba, S. Murakami,
J. Miyazawa, K. Narihara, H. Idei, Y. Yoshimura, T. Notake, M. Goto, S. Inagaki,
S. Masuzaki, S. Muto, Y. Nagayama, B. J. Peterson, K. Tanaka, K.Y. Watanabe,
K. Ohkubo, T. Mutoh, H. Yamada, A. Komori, K. Ida, Y. Nakamura, K. Kawahata,
N. Ohyabu, K. Matsuoka, O. Motojima, and LHD Experimental Group

National Institute for Fusion Science, 322-6 Oroshi-cho, Toki 509-5292, Japan

1. Introduction

Achievement of high-temperature plasmas is one of the main goals in the Large Helical Device (LHD), which is the world-largest superconducting helical system. The LHD is equipped with a negative-ion-based neutral beam injection (NBI) system as a main heating device, and the plasma electrons are dominantly heated due to its high injection energy of more than 150 keV (H). Thus, the ion temperature had been below 2.5 keV and lower than the electron temperature. A simple approach to raise the ion temperature is to increase the ion heating power by some means. Another approach, which is more important, is to improve the ion transport by achievement of the neoclassical electron root generating a strong positive electric field. In the 2001 experimental campaign, the third injector was newly installed and the NBI power was much increased, resulting in achievement of a high ion temperature of 5 keV with use of neon gas-puffing. By superimposing the centrally focused intense ECRH microwave on the NB-heated plasma, an internal transport barrier (ITB) was observed in the electron temperature profile, which suggests a formation of the neoclassical electron root. In the followings, the experimental results of high temperature plasmas are presented with transport analyses.

2. Negative-NBI System and ECRH System

The LHD-NBI system was designed for achievement of high-$n\tau T$ plasmas, where the target density is relatively high, more than $3 \times 10^{19} m^{-3}$ [1,2]. The nominal injection energy is as high as 180 keV for the tangential hydrogen injection. Two negative-ion-based NB-injectors of co- and counter-injection were operational in 1998, and one more counter-injector was installed in 2001. The total injection power was increased to 9 MW with a hydrogen beam energy of around 160 keV. The LHD-ECRH system employs two 82.7GHz, two 84 GHz and three 168 GHz gyrotrons, and each microwave is injected into the LHD as a strongly focused Gaussian beam using the vertical and horizontal antenna systems. A high-power ECRH up to 1.8 MW was concentrated within an averaged minor radius of $\rho=0.2$ in an inner magnetic-axis configuration of $R_{axis} < 3.53$ m [3].

3. Achievement of High Ion Temperature with Neon Injection

Since the injection energy is so high that the electron heating power would be dominant, the effective ion heating power should be enhanced to raise the ion temperature. In order to increase the plasma absorption power of the high-energy neutral beams in low-density plasmas, neon gas was injected, instead of hydrogen or helium gas. Figure 1 shows the comparison of the neon-injected plasma with the hydrogen one in $R_{axis}=3.53$m. Although the port-through NBI power is almost the same, around 8 MW, in both cases, the ionized beam power (plasma absorption power), estimated from the shine-through power

measurement [4], is about 1.3 times larger in the neon plasma at t=1.0sec ($n_e=1\times10^{19}$m^{-3}). The ion temperature in the neon plasma is higher by about 1 keV than that in the hydrogen plasma. Figure 2 shows the central ion temperature as a function of the plasma absorption power normalized by the line-averaged electron density for both neon and hydrogen plasmas in R_{axis}=3.6m. Since the Z_{eff} of the neon plasmas is higher, the beam ionization rate is 1.5 – 2 times larger than that in the hydrogen plasmas for low-density target plasmas below 1×10^{19} m^{-3} in R_{axis}=3.6 m. From the comparison of the beam ionization rates between the neon and the

Fig. 1   Time evolution of the plasma parameters for the neon and the hydrogen discharges.

hydrogen plasmas, the Z_{eff} of the neon plasmas is roughly estimated to be 2 times larger than that of the hydrogen plasmas. Assuming that the Z_{eff} of the hydrogen plasmas is around 3, the ion density of the neon plasmas is nearly a half of that of the hydrogen plasmas. Since the electron temperature is not so different, the effective ion heating power rate is double for the neon plasmas. As shown in Fig. 2, the ion temperature in the neon plasmas is increased linearly to the normalized absorption power and reaches 5 keV, while it is lower and is saturated in higher powers in the hydrogen plasmas. Although the effect of the neon gas injection can be explained by the increase in the absorption power and the enhancement of the direct ion heating power with a reduced number of ions, there could be a possibility of improvement of the plasma confinement by the impurity injection.

The transport analyses of the neon plasmas show that the electron transport is not largely changed compared with the hydrogen or helium plasmas. On the other hand, the ion transport cannot be locally analyzed as the ion temperature profile is not measured. The collisionality of neon ions is large and in the plateau regime because the ion collisionality depends on Z^3. The ion thermal diffusivity, roughly estimated by assuming that the ion temperature profile is parabolic, is 2 – 5 m^2/s in the neon plasmas, and is nearly the same as or a little bit larger than that in the hydrogen plasmas the collisionality of which is smaller by 1 – 2 orders of magnitude. The linear increase of the ion temperature in the neon plasma could be ascribed to the neon ions in the collisional
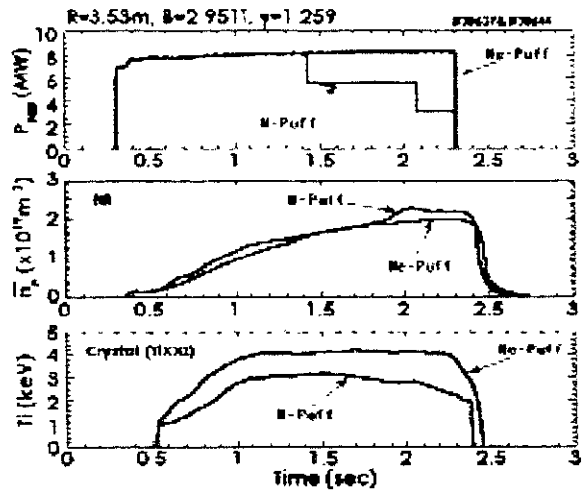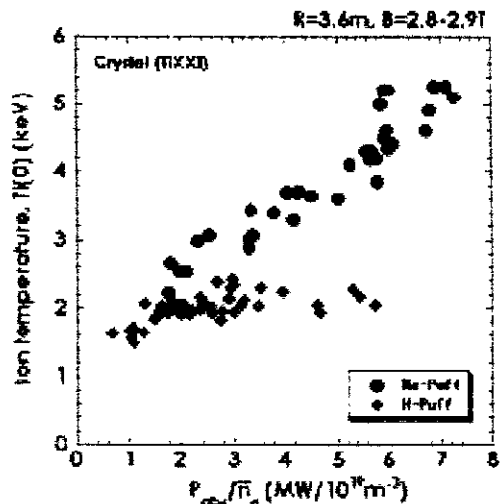

Fig. 2   Central ion temperature as a function of the plasma absorption power normalized by the electron density for the neon and the hydrogen plasmas.
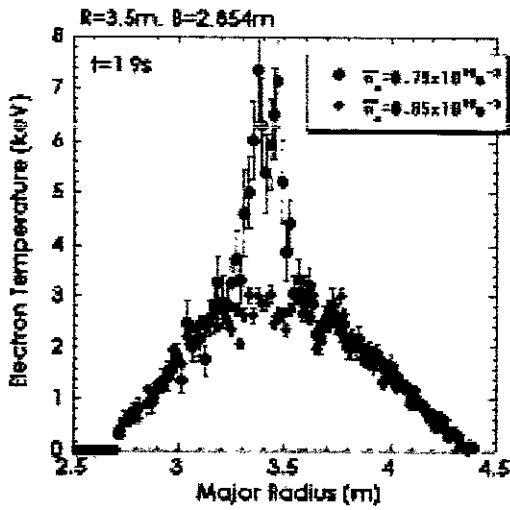
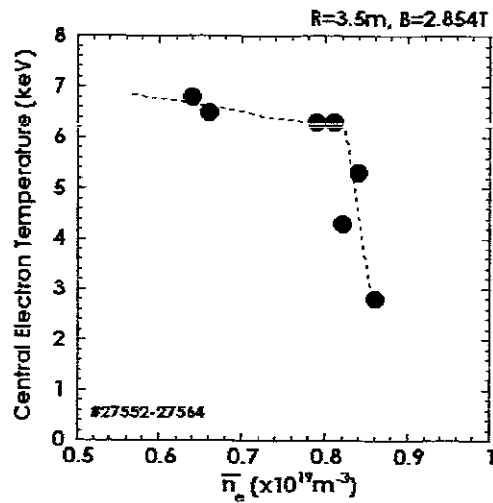Fig. 3   Electron temperature profiles with and without ITB.

Fig. 4   Central electron temperature as a function of the electron density.

plateau regime, while the hydrogen ions in the collisionless 1/v regime could lead to the saturation of the ion temperature in the hydrogen plasma.

4. Formation of Electron Internal Transport Barrier

In the experiments where the centrally focused intense ECRH microwave was superimposed on the NB-heated plasma, the electron temperature shows a centrally peaked profile with a steep gradient inside $\rho=0.3 - 0.4$. An example of this electron ITB (internal transport barrier) profile is shown in Fig. 3. The central electron temperature exceeds 10 keV in a lower density. There exist various kinds of threshold for the electron ITB formation, such as the ECRH power, the NBI power, and the density. Figure 4 shows the central electron temperature as a function of the line-averaged electron density, and the electron temperature profiles with and without ITB are shown in Fig. 3 at around the threshold densities. The electron transport is much improved in a region of the ITB formation. Figure 5 shows the electron thermal diffusivity χ_e as a function of the collisionality normalized by $v_{eq} = \varepsilon_h^{3/2} v_T \iota M/2\pi R$ at $\rho=0.2$ in the case of the ITB formation with an ECRH power threshold at $n_e=0.3\times10^{19}m^{-3}$. When a small ECRH power (180kW) is added to the NBI plasma, the T_e at $\rho=0.2$ is increased a little and the χ_e is much increased. With a larger ECRH power (280kW) the electron ITB profile is formed and the T_e at $\rho=0.2$ is raised, and then the χ_e is much reduced. The reduction of the χ_e at the threshold suggests the transition of neoclassical ion root to electron root. At this transition a strong positive radial electric field of around 50 kV/m is generated in the theoretical ambipolar flux calculation [5], although the electric field is not measured. However, the χ_e in the ITB profile is one-order of magnitude larger than the theoretical one in the neoclassical electron root, as shown in Fig. 5. The experimentally observed χ_e reduction in the ITB formation could be attributed to the suppression of the anomalous transport due to the electric field shear at a boundary of the ITB formed by the transition of the electric field [6].

Figure 6 shows a $T_e - n_e$ diagram for both ITB and no-ITB profiles at $\rho=0.2$. In the figure, the local ITB formation at $\rho=0.2$ is judged by the gradient of T_e, $dT_e/d\rho$, at $\rho=0.2$, i.e., no ITB formation for $dT_e/d\rho<1$, ITB formation for $dT_e/d\rho>5$, and marginal ITB formation
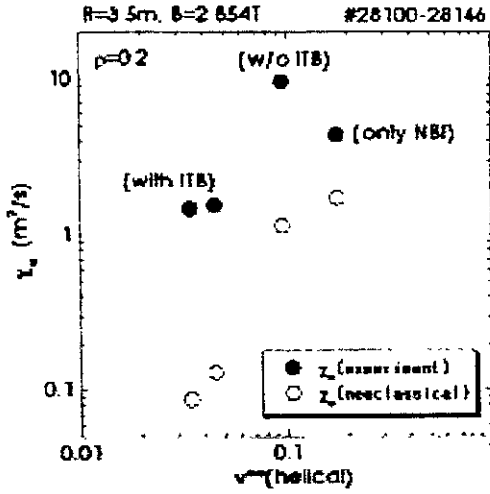
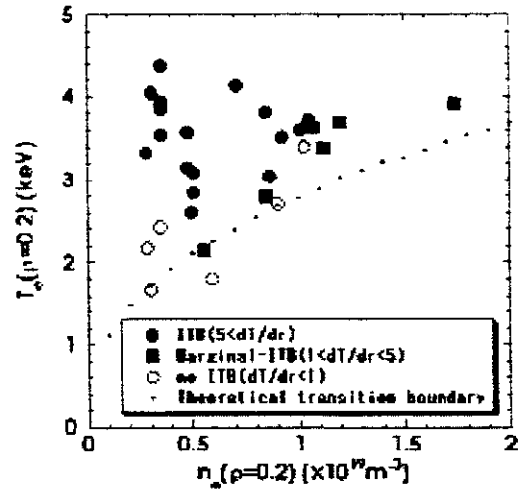Fig. 5 Electron thermal diffusivity as a function of the collisionality.

Fig. 6 $T_e - n_e$ diagram for both ITB and no-ITB profiles at $\rho=0.2$.

for $1 < dT_e/d\rho < 5$. In the figure, the theoretical transition boundary to the electron root from the ion root is also indicated. As shown in Fig. 6, the temperature threshold for the ITB formation is dependent on $n_e^{0.4}$, which coincides with the theoretical prediction. The electron ITB profile is also observed in relatively high-density plasmas of $>1\times10^{19}\mathrm{m}^{-3}$ with a higher ECRH power and a higher NBI power. Even in the neon plasmas the marginal ITB formation is observed at $n_e=1.8\times10^{19}\mathrm{m}^{-3}$ in the ECRH injection into a plasma heated by 8MW-NBI. Although a clear increase in the ion temperature has not been recognized, a high electron temperature in the ITB formation would enhance the ion heating ratio in high-power NBI heating, leading to increase in the ion temperature. Moreover, the neoclassical electron root in the ITB formation would reduce the ion transport in the collisionless regime, which would realize a higher ion temperature.

5. Summary

To raise the ion temperature with a high-energy negative-NBI heating, neon gas was injected for increasing the plasma absorption power of the neutral beam and enhancing the effective ion heating power with a reduction of the ion number in high-Z_{eff} plasmas. As a result, the ion temperature is raised to 5 keV at an NB-injection power of 8 MW. By injection of centrally focused ECRH microwave into the NBI-heated plasma, the electron ITB profile with a steep gradient inside $\rho=0.4$ was observed. The temperature threshold for the ITB formation depends on $n_e^{0.4}$, which agrees with the theoretically predicted transition to the neoclassical electron root from ion root. The electron ITB was observed also in the neon plasmas. It is important to obtain a high ion temperature by achieving the improvement of the ion transport in the neoclassical electron root, and this is a future work.

References

[1] O. Kaneko, et al., Proc. the 16th IAEA Fusion Energy Conference (Montreal, Canada, 1996) Vol 3, p. 539.
[2] Y. Takeiri, et al., Proc. the 17th IEEE/NPSS Symp. on Fusion Engineering (San Diego, 1997) Vol. 1, p. 409.
[3] S. Kubo, et al, J. Plasma Fusion Res. 78, 99 (2002).
[4] M. Osakabe, et al, Rev. Sci Instrum 72, 590 (2001).
[5] M. Yokoyama, et al, Nucl. Fusion 42, 143 (2002).
[6] K. Itoh, et al., Plasma Phys. Control. Fusion 36, 123 (1994).

Transport Analysis of ECH Overlapped NBI Plasmas in LHD

H.Funaba, T.Shimozuma, S.Kubo, H.Idei, Y.Yoshimura, T.Notake [1], K.Narihara,
K.Ida, Y.Nagayama, S.Inagaki, Y.Takeiri, M.Osakabe, K.Tanaka, B.J.Peterson,
K.Y.Watanabe, S.Murakami, M.Yokoyama, K.Kawahata, N.Ohyabu
and the LHD Experimental Group

National Institute for Fusion Science, Toki, Gifu 509-5292, Japan
[1]*Nagoya Univ., Grad. School of Energy Engineering and Science, Nagoya 464-8601, Japan*

1. Introduction

The electron temperature, T_e, profile with a high central T_e and a steep gradient, ∇T_e, was observed on the Large Helical Device (LHD) [1] in both ECH plasmas and low density NBI plasmas with overlapping of the strongly focused ECH [2]. Local transport analysis is carried out in order to clarify whether any transport improvement, such as the electron thermal transport barrier which is observed in the Compact Helical System (CHS) [3], appeared or not in LHD associated with the high central T_e.

The electron thermal conductivities in NBI with ECH plasmas of various densities are evaluated and they are compared with the results of the neoclassical calculation with the radial electric field, E_r. Moreover, some transport simulations of the temporal development of T_e are carried out to evaluate the electron thermal transport at the central region.

2. Transport analysis of ECH overlapped NBI plasmas

In the plasmas heated by NBI and ECH, the high $T_e(0)$ and the steep ∇T_e appeared when the absorbed power of ECH, P_{ECH}, exceeded a certain threshold power or the electron density, n_e, was lower than a threshold density. Figure 1 (a) shows four profiles of T_e, which were measured by the YAG Thomson scattering system [4]. Three of them are in the cases of NBI with ECH heated plasmas with different n_e ($\bullet$: $\bar{n}_e = 0.15 \times 10^{19}\,\mathrm{m}^{-3}$, $\triangle$: $0.24 \times 10^{19}\,\mathrm{m}^{-3}$ and $\diamond$: $1.7 \times 10^{19}\,\mathrm{m}^{-3}$) and the other symbol $(+)$ represents T_e in a NBI-only plasma. Here, $\rho = (\Phi/\Phi_a)^{1/2}$ (Φ : the toroidal magnetic flux) is the normalized average minor radius and $\rho < 0$ denotes the inside of the magnetic axis position, R_{ax}. These plasmas are produced under the conditions of $R_{ax} = 3.75\,\mathrm{m}$ (the standard magnetic configuration) and the magnetic field strength $B = 1.52\,\mathrm{T}$. The spatial profile of E_r can be measured in the $R_{ax} = 3.75\,\mathrm{m}$ case by the charge exchange spectroscopy (CXS) [5, 6] of NeX with the neon gas puffing. $B = 1.52\,\mathrm{T}$ is adjusted to the central heating condition of the 2nd harmonic ECH. In the lowest n_e case ($\bullet$), the T_e profile has $T_e(0) \geq 8\,\mathrm{keV}$. The steep ∇T_e appears in the low density cases ($\bullet$, $\triangle$) at the $\rho < 0.2$ region. However, such ∇T_e can't be seen in the high density case ($\diamond$).

The experimental thermal diffusivities, χ_e for electrons and χ_i for ions, are evaluated by the local transport analysis using an one-dimensional transport code, PROCTR [7].

This code reads the magnetic flux surface data and the spatial profiles of T_e, n_e, the ion temperature, T_i, the absorbed power of ECH, P_{ECH}, the deposition power of NBI to electrons and ions, P^e_{NBI} and P^i_{NBI}, the radiation power, P_{rad}, and so on. $P^e_{NBI}(\rho)$ and $P^i_{NBI}(\rho)$ are given by the calculation results from a three-dimensional Monte Carlo simulation code [8]. $P_{ECH}(\rho)$ is calculated by the ray-tracing method. Its profile depends on the focal point and the R_{ax} shift by β.

χ^{exp}_e in the NBI-only case is about $12\,\mathrm{m^2/s}$ at the center and it gradually decreases towards the edge as shown in Fig.1(b). The magnitude of χ^{exp}_e in the high density NBI with ECH plasma becomes large at the central region because of the increase in the deposition power to electrons. On the other hand, the central χ^{exp}_e was reduced in the case of the low density NBI with ECH plasma. It becomes under $1\,\mathrm{m^2/s}$ at $\rho < 0.1$ with the steep ∇T_e.

Figure 1(c) shows the power balance of electrons and ions in a NBI with ECH plasma ($\triangle$ in Fig.1(a)). The notations of p_{ECH}, p^e_{NBI}, p_{ei}, p_{rad}, p_{conv} and p_{cond} in the figure of the T_e equation represent the ECH absorbed power, the NBI heating power to electrons, electron-ion rethermalization, radiation loss, convection loss and radial transport, respectively. In the figure of the T_i equation, p^i_{NBI}, p_{ion} and p_{cx} are the NBI heating power to ions, the energy loss due to neutral ionization and the charge exchange loss, respectively. p_{ECH} is localized at the resonance position of the normalized minor radius $\rho \simeq 0.1$ and its peak value exceeds $1\,\mathrm{MW/m^3}$. On the other hand, p^e_{NBI} has a broad profile and it is usually less than $100\,\mathrm{kW/m^3}$. Especially, it is less than about $40\,\mathrm{kW/m^3}$ in this figure because of the low n_e. p^i_{NBI} is also about $40 \sim 50\,\mathrm{kW/m^3}$ near the center in this case.

Figure 2(a) shows the neoclassical E^{neo}_r which are calculated by the condition of $\Gamma^{asym}_e = \sum Z_j \Gamma^{asym}_i{}_j$ [9], where Γ^{asym}_e and Γ^{asym}_i are the asymmetric part of the neoclassical electron and ion flux, re-

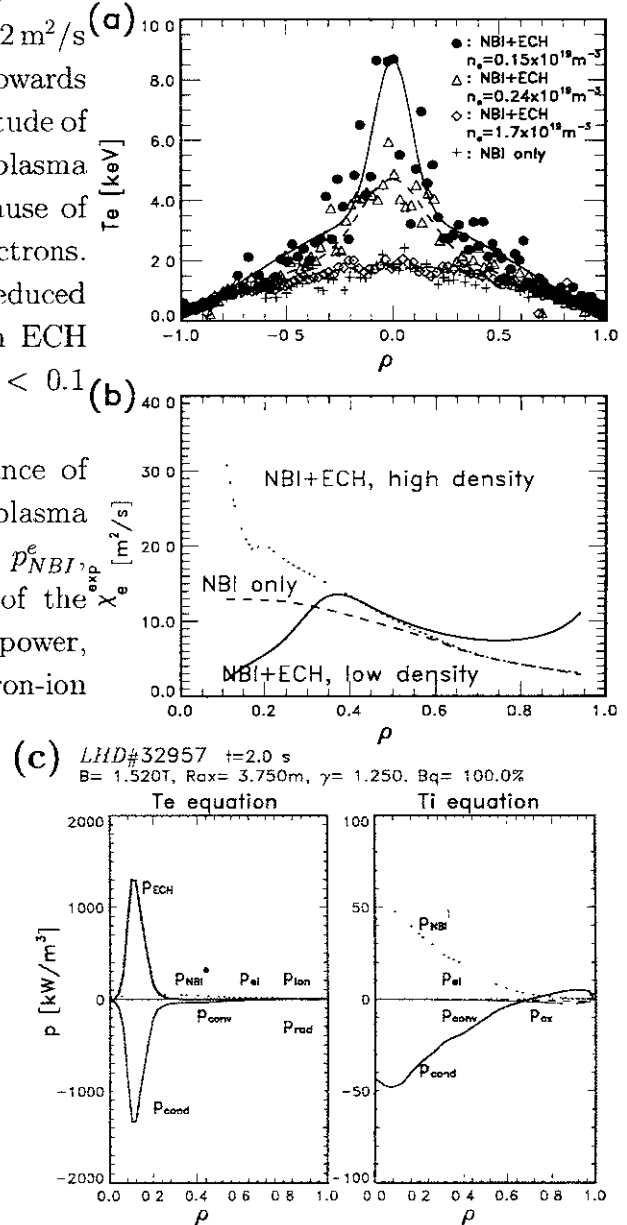**Figure 1.** (a) T_e profiles of three NBI with ECH plasmas and a NBI-only plasma, (b) χ_e of high and low density NBI with ECH plasmas and a NBI-only plasma, (c) the power balance of electrons and ions in a low density NBI with ECH plasma.

spectively. E_r^{neo} in the low density NBI with ECH plasma is positive in the whole plasma and it shows a peak at the central region. This spatial profile is similar with the experimentally observed E_r by CXS with neon gas puffing in the plasmas of $n_e > 0.5 \times 10^{19}\,\mathrm{m}^{-3}$, but the magnitude of E_r^{neo} is larger than the E_r^{CXS} by about factor of 2. On the other hand, E_r^{neo} in the NBI-only or the high density plasmas shows negative or small positive values and multiple roots of E_r appear in the NBI-only case. It may be considered that the neoclassical E_r^{neo} affects on the improvement of χ_e in the ECH overlapped plasmas. However, the neoclassical χ_e^{neo} with E_r^{neo} is smaller than χ_e^{exp} by about one order, as seen in Fig.2(b).

3. Simulations of the temporal development of the electron temperatures

The transport coefficients which are derived by the steady state analysis are still ambiguous at the central region of $\rho < 0.1$ as the power absorption profile of ECH by ray-tracing method shows small value at the vicinity of $\rho = 0$. In order to evaluate χ_e near the center, the temporal development of T_e measured by ECE [10], T_e^{ECE}, are studied. Figure 3(a) shows T_e^{ECE} and the results of transport simulation at $\rho = 0.03, 0.085$ and 0.434. This calculated T_e are derived by assuming a certain χ_e after the ECH off time.
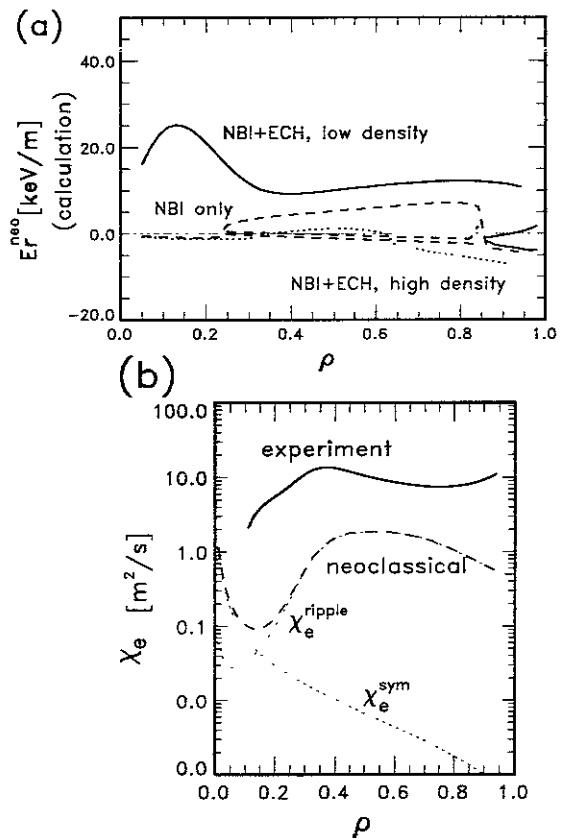

Figure 2. (a) Neoclassical E_r^{neo} in high and low density NBI with ECH plasmas and a NBI-only plasma, (b) $\chi_e^{exp} and \chi_e^{neo}$ in a low density NBI with ECH plasma.
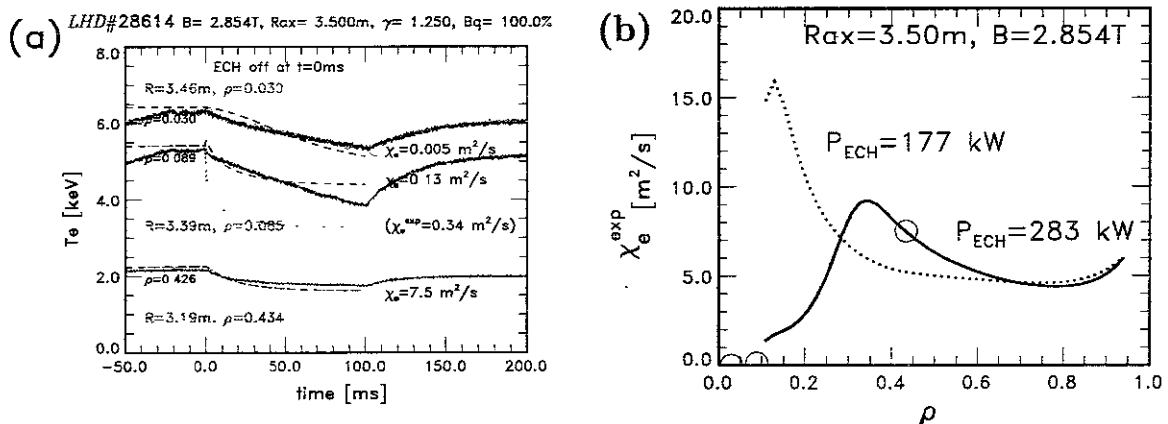

Figure 3. (a) the ECE signals and the simulated temporal development of T_e, (b) χ_e^{exp} in the NBI with ECH plasmas at $R_{ax} = 3.50\,\mathrm{m}$ and $B = 2.895\,\mathrm{T}$. The symbol, $\bigcirc$, denotes the values which are used in this simulation.

These ECH modulation experiments were operated under the conditions of $R_{ax} = 3.50$ m and $B = 2.895$ T with the ECH power of 283 kW and 177 kW. In the higher P_{ECH} case, the T_e profile has a steep gradient and the decay times, τ_d, of T_e^{ECE} are more than 100 ms at the central region, while no steep gradient was observed and $\tau_d \simeq 20$ ms in the lower P_{ECH} case.

The simulation of T_e are carried out from an initial profile measured by the Thomson scattering and therefore, the magnitude of T_e^{ECE} are calibrated by the temperatures of Thomson scattering. The dotted curve in Fig.3(a) shows a example of the results of the calculation by using χ_e^{exp}, which is shown in Fig.3(b) (solid curve). The decay time of this case is smaller than that of the ECE results. The dashed curves in Fig.3(a) are the calculation results by using some assumed χ_e which are selected in order to reproduce the time development of T_e^{ECE}. Although these simulation results are not completely agree with the experimental data, the longer decay times of $50 \sim 100$ ms can be reproduced.

The values of χ_e assumed in Fig.3(a) are plotted in Fig.3(b) ($\bigcirc$). The assumed χ_e is 0.005 m^2/s at $\rho \sim 0.03$ and 0.13 m^2/s at $\rho \sim 0.08$. It may be considered that these small χ_e values indicate some improvement of electron thermal transport at the center.

4. Summary

The local electron thermal transport was investigated for the low density NBI with ECH plasmas on LHD. The derived χ_e^{exp} was reduced with the steep gradient of T_e near the center, but the values of χ_e^{exp} are still larger than the neoclassical χ_e^{neo}. The radial electric field predicted by the neoclassical theory, E_r^{neo}, is also calculated. Although the magnitude of E_r^{neo} is larger than the experimentally measured E_r^{CXS}, their radial profiles are similar. Some ambiguity remains in the steady state analysis of χ_e at the center. However, the electron thermal transport at the central region seems to be improved from the view point of the temporal development of T_e by comparing the ECE signals with the results of transport simulation.

References

[1] A.Iiyoshi, A.Komori, et.al., Nucl.Fusion**39**(1999)1245.

[2] S.Kubo,T.Shimozuma,et.al.,Journal of Plasma and Fusion Research **78**(2002)99.

[3] A.Fujisawa, H.Iguchi, T.Minami et.al., Phys.Rev.Lett.**29**(1999)2669.

[4] K.Narihara,et.al.,Rev.Sci.Instrum.**72**(2001)1122.

[5] K.Ida, S.Kado et.al., Rev.Sci.Instrum.**71**(2000)2360.

[6] K.Ida, Plasma Phys.Control.Fusion**40**(1998)1429.

[7] H.C.Howe, ORNL/TM-11521(1990).

[8] S.Murakami, N.Nakajima and M.Okamoto, Trans.Fusion Technol.**27**(1995)256.

[9] M.Yokoyama, K.Ida et.al.,Nucl.Fusion**42**(2002)143.

[10] Y.Nagayama,et.al.,Rev.Sci.Instrum.**70**(1999)1021.

EXPERIMENTAL ANALYSIS AND PREDICTIVE SIMULATION OF TRANSPORT BARRIER IN LHD AND CHS PLASMAS

Kozo Yamazaki, Shin Kubo, Kazuto Narihara, Kenji Tanaka, Takashi Minami,

CHS Group and LHD Experimental Group

National Institute for Fusion Science, 322-6 Oroshi-cho, Toki, 509-5292, Japan

Abstract

In the central Electron Cyclotron Heating (ECH) experiments, the internal transport barrier (ITB) has been found in the Compact Helical System (CHS), and recently in the Large Helical Device (LHD). The strong positive radial electric field has been experimentally observed, which reduces neoclassical ripple transport and anomalous losses. The calculated neoclassical transport coefficients without effects of radial electric field roughly agrees with experimentally obtained transport values, but are ten times smaller than the experimental values when the strong neoclassical ambipolar radial electric field is included. The common ITB physics pictures are expected in LHD and CHS high electron temperature plasmas.

1. Introduction

In the helical confinement systems, the strong electric field is supposed to be utilized for improving the plasma confinement. High central electron temperature plasmas with positive electric potential have been obtained in the centrally focused Electron Cyclotron Heating (ECH) experiment of the Compact Helical System (CHS) [1]. The formation of this internal transport barrier (ITB) is correlated with the reduction of density fluctuation and the shear of electric field, and is related to neoclassical positive electric field in the low-density regime [1, 2]. Recently in the Large Helical Device (LHD) we have obtained ten-keV electron temperature plasmas using centrally focused Gaussian beam at the fundamental and second harmonic resonances [3]. Here, transport analysis has been done in both LHD and CHS for their comparisons.

2. Method of Transport Analysis using TOTAL Code

For predictive simulation and experimental analysis of toroidal plasmas, a simulation code TOTAL (Toroidal Transport Analysis Linkage) has been developed [4,5]. This consists of a 3-dimensional equilibrium with ohmic and bootstrap currents and a 1-dimensional transport

with neoclassical loss determined by ambipolar radial electric field as well as anomalous transport (empirical or drift turbulence models). In both core and edge plasma analyses, the plasma equilibrium is iteratively and consistently calculated using experimental data on the virtual expanded edge flux coordinates, and the calculated transport properties are compared with several theoretical models.

3. Transport Barrier formation and Experimental Analysis in CHS

The box-type temperature profile often can be seen in reversed-shear tokamaks and parabola-type ITB is obtained in the normal shear tokamak operations. In helical system bell-type electron temperature profiles are obtained. Figure 1 shows the electron temperature and density profiles with ITB (ECH 200kW) and without ITB (ECH 150kW). The experimental thermal diffusivities roughly agree with zero radial-electric-field case (Er=0), but are ten times higher than the neoclassical values with self- consistent electric field.
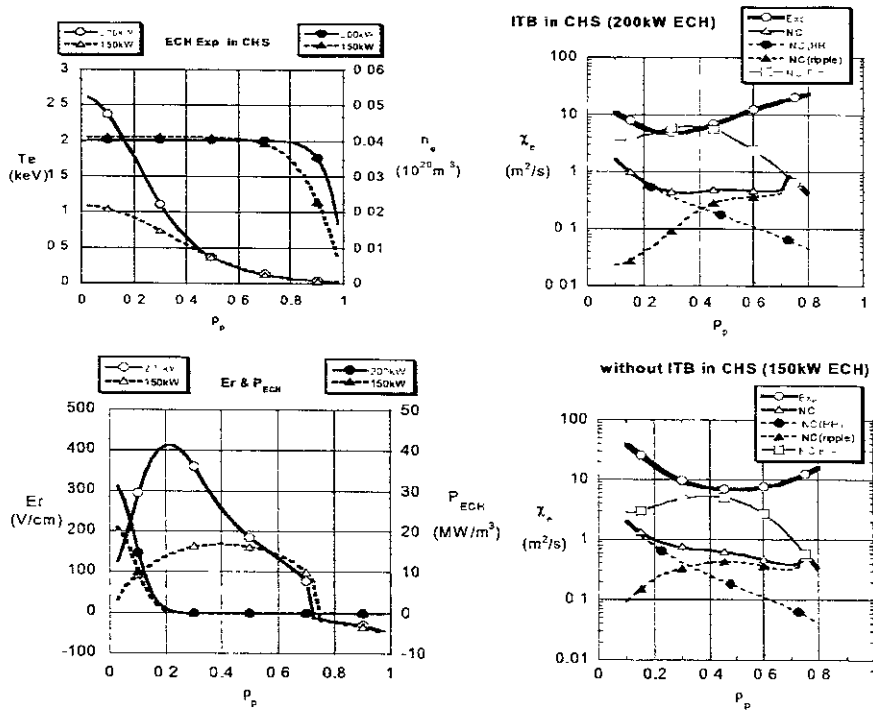
Fig. 1   ITB profiles and transport coefficients of CHS

4. Transport Barrier formation and Experimental Analysis in LHD

Hot electron temperature operations have been obtained also in LHD using ~ 1 MW ECH heating power [2]. Figure 2 shows the electron temperature and density profiles measured by 200-channel YAG Thomson scattering system and 11-channel FIR interferometer. The 3-dimentional plasma equilibrium is calculated self-consistently using TOTAL code [5]. Here, we calculated the plasma performance with the assumption of

neoclassical transport with helical field harmonics and self-consistent radial electric field in addition to semi-empirical anomalous transport loss [4]. The calculated electric field in the LHD plasma depends critically on the plasma density and heating power deposition (position and power density).

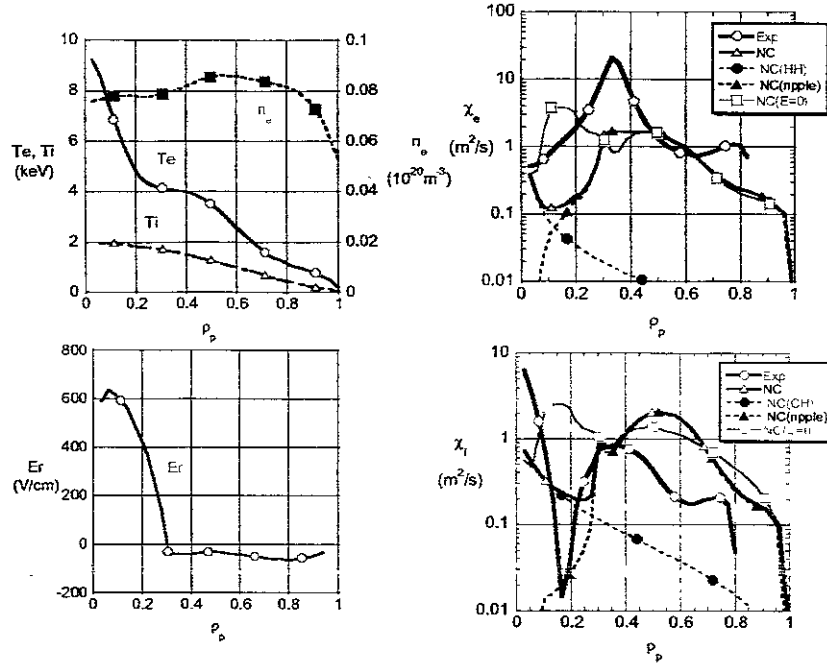In order to evaluate transport coefficients, the parabolic ion temperature profile with experimental central value is assumed. We can determine experimental transport coefficients as shown in Fig. 2. The experimental electron transport coefficients near the ITB region are ten times higher than the neoclassical values (HH plus ripple transport for electron, CH plus ripple transport for ion). The strong positive radial electric field has been expected.

Fig. 2   ITB profiles and transport coefficients of LHD (#26943, 0.5ms)

5. Predictive Transport Simulation in LHD

Related to the ITB shot, the following four predictive simulations have been carried out in addition to the previous section; (1) full simulation, (2) only experimental density profile is used, (2) experimental density and electron temperature profiles are used, and (4) drift wave model simulation.

(1) Full simulation

Without using experimental plasma profiles, we can simulate high T_e plasmas using empirical transport model and neoclassical ripple transport model with self-consistent ambipolar electric field [4]. The experimental line-averaged electron density is used in the simulation. The simulated density profile does not agree with experiments, therefore central temperature is rather low. To simulate slightly hollow electron density profile, anomalous outward particle flow is required in addition to the neoclassical diffusion.

(2) Simulation using experimental density profiles

The anomalous transport coefficients described in Ref.[4] are assumed here. The central electron density and thermal coefficient are both low enough to get higher Te(0) than 10 keV. The anomalous transport model with fixed profile is not realistic and it should be modified to fit the experimental values.

(3) Simulation with experimental n_e and T_e profiles

The ion temperature has been calculated using experimental n_e and T_e profiles. Several bumps in radial electric field E_r as a function of minor radius have been obtained. The E_r profile critically depends on T_i profile, therefore T_e profile strongly depends on ion temperature.

(4) Drift Wave Model Simulation

Multi-mode transport analysis in addition to neoclassical transport has been carried out for LHD using 5 times smaller drift-wave turbulent transport coefficients of Ref. [4] to fit standard LHD operation. The simulated ion temperature is lower than the experiment. The present model will be modified to include electric shear effect for the confinement improvement in the future.

6. Summary & Discussion

The transport analysis has been carried out for high-Te ECH discharges in both LHD and CHS focusing on the comparisons between the experimental values and neoclassical values. Experimental transport coefficients near ITB roughly agree with neoclassical values in the case of Er=0, but are about ten times higher than the neoclassical vales including the effect of Er in both LHD and CHS plasmas. The anomalous transport might be dominant near ITB and be reduced by the strong electric field shear. The common physics pictures are expected in LHD and CHS high electron temperature plasmas.

References

[1] A. Fujisawa et al., Phy. Rev. Lett. **82** (1999) 2669-2672.

[2] T. Minami, A. Fujisawa et al., Plasma Phys. Control. Fusion **44** (2002) A197.

[3] S. Kubo, T.Shimozuma et al, J.Plasma Fusion Res., **78** (2002) 99.

[4] K.Yamazaki, T.Amano, Nucl. Fusion **32** (1992) 633.

[5] K.Yamazaki et al., 26th EPS Conference on Controlled Fusion and Plasma Physics, 14-18 June 1999, Maastricht (1999) P3.107.

Energetic ion driven MHD instabilities in high β LHD plasmas

S. Yamamoto[i], K. Toi, S. Ohdachi, N. Nakajima, S. Sakakibara, K.Y. Watanabe,
T. Masuzaki, H.Yamada, Y. Narushima, Y. Takeiri, M. Osakabe, K. Narihara, I. Yamada,
K. Tanaka, T. Tokuzawa, S. Morita, M. Goto, K. Kawahata, Y. Nakamura, N. Ohyabu,
and LHD experimental group G1, G2

National Institute for Fusion Science, Toki-shi 509-5292, JAPAN
1) Dep. of Energy Eng. and Science, Nagoya Uni., Nagoya-shi 464-8601, JAPAN

Introduction

MHD instabilities destabilized by the energetic ions are being studied in many magnetic confinement devices because there are two important and of interest issues for plasma confinement. One is to clarify the characteristics of these energetic ion driven MHD modes. The other is to clarify the effects of the MHD instabilities on energetic ion transport and bulk plasma confinement. In particular, these researches are extensively being studied in many tokamaks with regard to alpha particle physics on ITER.

These MHD instabilities are also being studied in helical systems, which are thought to be promising alternative concepts for the tokamaks. Toroidicity induced Alfvén eigenmodes (TAEs) and energetic particle modes (EPMs), which are destabilized by the energetic ions, were observed in the Compact Helical System (CHS)[1,2], Wendelstein-7AS (W-7AS) [3] and the Large Helical Device (LHD) [2,4]. However, knowledge about these modes in helical systems is still unclear due to a complex magnetic configuration. Alfvén eigenmodes (AEs) are predicted to be more unstable in a high beta plasma of LHD from the previous studies. In this paper, we report two topics about energetic ion driven MHD instabilities in high beta LHD plasmas.

TAEs in high beta LHD plasmas and loss of energetic ion caused by TAEs

In NBI heated LHD plasmas at low magnetic field ($B_t < 1$ T), the bursting TAEs are often observed, of which amplitude is one order of magnitude larger than non-bursting ones. A typical high beta discharge that TAEs are observed is shown in Fig.1, where the absorbed NBI power is 2.7 MW and hydrogen beams with $E_{NBI} = 150$ keV are tangentially injected into a hydrogen plasma in the inward-shifted configuration at the magnetic field $B_t = 0.5$ T. In this high beta LHD plasma, $m\sim 2\text{-}3$ / $n=2$ TAE is observed, of which gap is formed by the poloidal mode coupling of $m=2$ and 3 modes, and $m\sim 2\text{-}3$ / $n=1$ TAE is also observed. The TAE with $m\sim 2\text{-}3$ / $n=1$ disappears at $t = 0.8$ sec because the TAE gap is disappeared due to considerably modification of the rotational transform profile caused by the finite beta effect and the net plasma current.
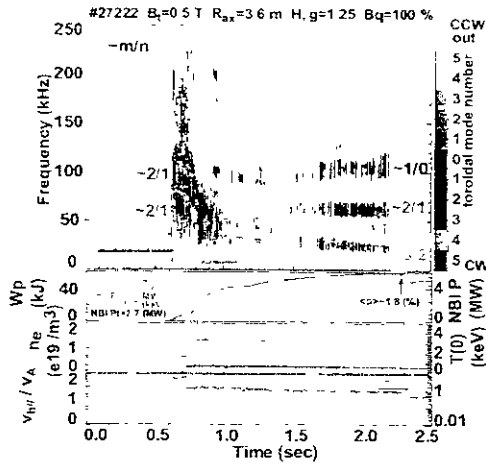
Fig.1, Time evolution of magnetic fluctuations in a high beta NBI-heated LHD plasma. The bursting TAEs are
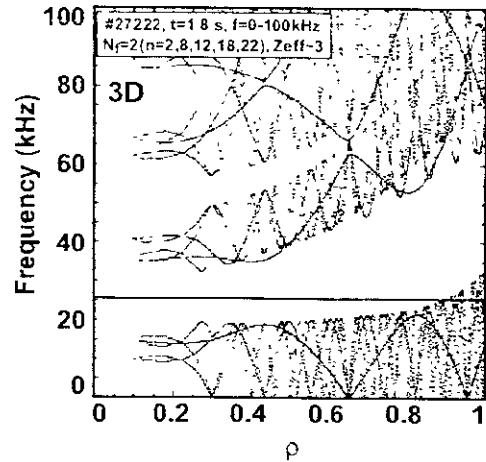

Fig.2, The shear Alfvén spectra with N_f = 2 at t = 1.8 s of the plasma shown in Fig. 1. The spectra are calculated for the 3D magnetic configuration.

We compare the observed frequencies at t = 1.8 s is the plasma shown in Fig. 1 with the shear Alfvén spectrum that is calculated for 3D magnetic configuration. Here the toroidal mode coupling is taken into account. A heliotron configuration has a 3D magnetic configuration having the toroidal field period number N_p. A family of modes with toroidal mode number n' satisfying the relation $n'+n$ or $n'-n = kN_p$ (k = ...-2,-1,0,1,2....) can couple with the mode having the toroidal mode number n [5]. In LHD case, the N_f = 2 mode is composed by Fourier modes with n' = ...-12, -8, -2, 2, 8, 12, ...etc. The toroidal mode coupling among n = 2,8,12,18,22 and 28 Fourier modes is taken into account for the calculation of the spectrum shown in Fig. 2. The gap structures are produced through poloidal mode coupling for all Fourier modes with different toroidal mode number in the
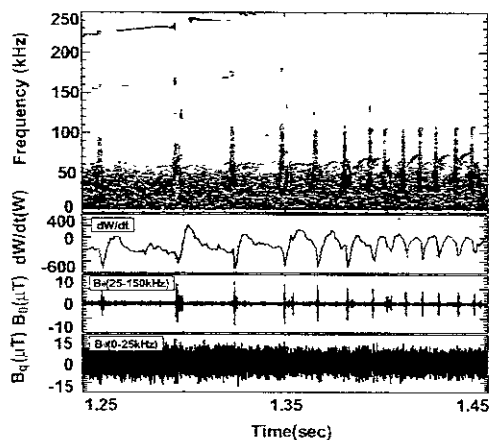

Fig. 3, Time evolution of magnetic fluctuations and time derivative of the stored plasma energy dW/dt.

same mode family. This leads to the formation of the envelope of all these TAE gaps. Good alignment of the TAE gap from the plasma core towards the edge can be realized by the large Shafranov shift and the decrease of the magnetic shear in such high beta case. The good alignment of the gap structure and high bema beta $<\beta_b>$ are thought to be responsible for the excitation of TAE with large amplitude.

The TAEs appreciably affect the energetic ion transport and/or bulk plasma confinement because some plasma parameters are simultaneously modulated with bursting TAEs, as

shown in Fig. 3. The transient decrease in the stored energy ($dW/dt<0$) is explained by the transient loss of energetic ions in the course of the slowing down. The transient decrease in W corresponds to about 15% loss of the absorbed beam power by each burst. The loss rate of absorbed beam power is increased with the increase in fluctuation amplitude of TAEs. In the highest beta plasma, where $<\beta_{bulk}> \sim 2.5$ % at low magnetic fields ($B_t < 0.7$ T), TAEs aren't observed because the resonance condition might not be satisfied.

The observation of helicity induced Alfvén eigenmodes (HAEs)

The MHD instabilities, of which frequency is eight times higher than that of TAE gap, are newly observed in NBI heated plasmas of LHD at the low magnetic fields ($B_t < 0.7$ T). The typical discharge where these modes were observed is shown in Fig. 4, where hydrogen beams are injected into H plasma in the configuration of $R_{ax} = 3.6$ m at $B_t = 0.5$ T. The coherent modes in the range of 180 ~ 220 kHz are observed after $t = 1$ s. The magnetic fluctuation amplitude reaches $b_\theta/B_t \sim 10^{-6}$ at the probe position. The observed modes are identified to be $n = 2$ and propagate in the diamagnetic drift direction of energetic ion. These modes are thought to be Alfvén eigenmode (AE), because the frequencies of these modes are scaled the Alfvén velocity (v_A).

The toroidal mode coupling related to 3D magnetic configuration leads to a generation of new spectral gap, which is related to the helical fields components. In this new gap, the helicity induced AEs (HAEs) [5,6] can be excited. The frequencies of these modes are by 40 % lower than the predicted HAE gap frequency. However, the full width of the HAE gap is considerably wide (~200 kHz in this case). The observed modes are thought to be related to the HAEs.
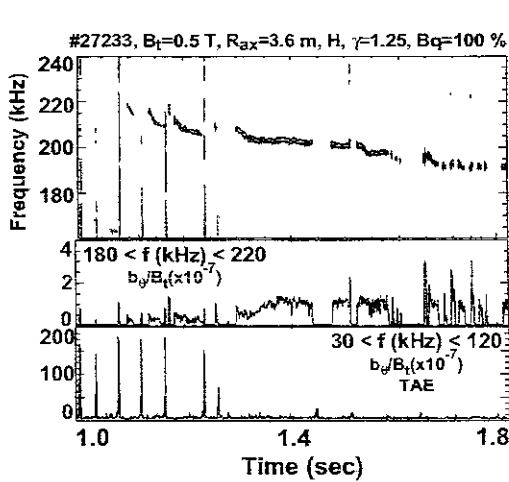

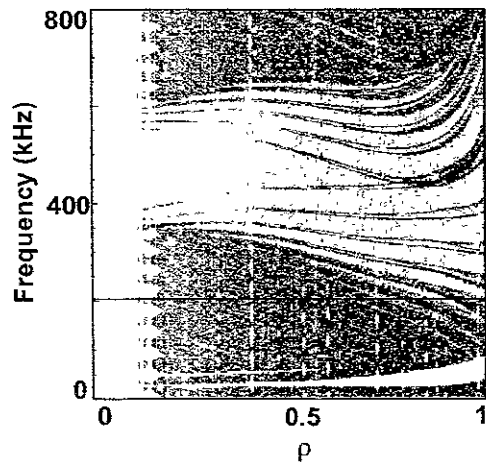Fig. 4, The high frequency modes with $n = 2$ are observed in a NBI-heated plasma.

Fig.5, The shear Alfvén spectra with $N_f = 2$ at $t = 1.4$ s of the plasma shown in Fig. 4. The HAE gap is generated around $f\sim400$ kHz by the toroidal mode coupling.

We compare these observed frequencies at $t = 0.8$ s of the plasma shown in Fig. 4 with the shear Alfvén spectrum for $N_f = 2$(Fig.5.), where the toroidal mode coupling among $n = 2$, 8, 12, ...48, 52, (including 13 kinds of n and 919 modes), is taken into account. The HAE gap has a good alignment from the plasma core toward the edge. The continua with high-n mode exist in HAE gap and new continua inside HAE gap might be produced by the absence of helical symmetry of helical field components [7]. The former continua may not affect the low-n modes because the toroidal mode coupling is weak and the latter continua may affect the low-n modes. The solid line in Fig. 5 indicates the measured frequency of magnetic fluctuation. The frequency lies in the HAE gap at the plasma edge ($\rho \sim 0.8$) and intersects newly generated continua inside the HAE gap location. We predict that the modes would be strongly suffered from continua damping but mode are excited. The profile of energetic ion pressure is predicted to be flat because the larmor radius of passing energetic ion reaches up to 10 % of plasma radius. Therefore, the gradient of energetic ion pressure has a peak near the plasma edge and the growth rate of the mode may be significantly large enough to overcome the damping. It is concluded from these analyses that the HAEs are observed for the first time in helical systems.

Summary

We investigated energetic ion driven MHD instabilities in NBI heated high beta LHD plasmas. The $m\sim 2$-$3/n=2$ bursting TAEs with large amplitude are observed and appreciably affect the energetic ion transport. About 15% of the absorbed beam power is lost by each burst. The high frequency MHD instabilities are newly observed in NBI heated plasmas of LHD. As a result of a comparison with the shear Alfvén spectrum that in full 3 dimensional magnetic configurations, the frequency of observed modes lies in the HAE gap near the plasma edge. The observed modes are thought to be HAEs.

References

[1] M. Takechi, et. al., Phys. Rev. Lett. **83**, 312 (2001).

[2] K. Toi, et. al., Nucl. Fusion **40**, 1349 (2000).

[3] A. Weller, et. al., Phys. Plasmas **8**, 931 (2001)

[4] S. Yamamoto, et. al., J. Plasma Fusion Res. SERIES **3**, 117 (2000)

[5] N. Nakajima, C. Z. Cheng, and M. Okamoto, Phys. Fluids B **4**, 1121 (1992)

[6] Ya. I. Kolesnichenko, et. al., Phys. Plasmas **8**, 491 (2001)

[7] N. Nakjima (private communication).

Study of ideal external mode in LHD

Y. Narushima, K. Y. Watanabe, S. Sakakibara, N. Nakajima, K. Nishimura,

H. Yamada, K. Yamazaki and LHD experimental group

National Institute for Fusion Science, 322-6 Oroshi-cho, Toki, Gifu 509-5292, Japan

W.A. Cooper[1]

1) *Centre de Recherches en Physique des Plasmas,*

Association Euratom / Confederartion Suisse, EPFL, 1015 Lausanne, Switzerland

1. Introduction

Serious MHD instabilities leading to the degradation of the energy confinement time and the termination of the discharge have not been observed in experiment on the Large Helical Device (LHD) [1]. It is worthwhile to investigate the characteristics of the MHD activities in the LHD plasma theoretically and experimentally. In this paper, we focus on the external mode (particularly $m/n=1/1$ mode). The low-n ideal MHD analysis is performed for $n=1$ mode family on the LHD plasma using the three-dimensional stability code **TERPSICHORE** [2].

2. Characteristics of ideal MHD stabilities of LHD plasma at peripheral region

The analyzed plasma has the magnetic axis at $R_{ax}=3.6$m and no plasma current $I_p=0$. The plasma pressure p is expressed as $p=p_0(1-\rho^2)^k$. Here, p_0, ρ, and k are the central plasma pressure, normalized minor radius in flux coordinate, and the parameter of the profile with the range of 0.2 to 1.0, respectively. The equilibrium is solved by VMEC code [3] under the condition of the free boundary. Figure 1 shows low-n ideal MHD mode unstable region in $\langle\beta\rangle$ - $d\beta/d\rho$ diagram for $n=1$ mode family. The all symbols mean the destabilized points with respect to the low-n interchange mode calculated by **TERPSICHORE** under the free boundary condition. The solid, dashed and dotted
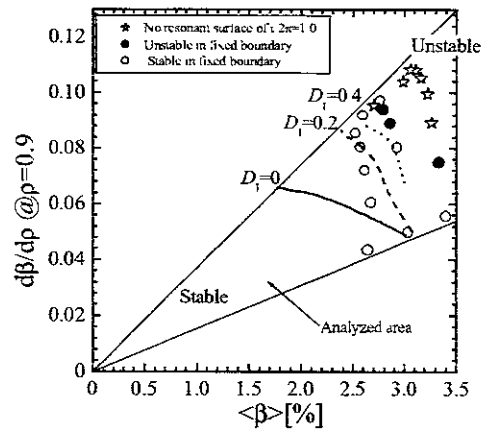

Fig. 1 Relation between the beta and the pressure gradient at $\rho=0.9$.

lines mean the contours of Mercier parameter [4] with D_I=0, 0.2, and 0.4, for $\iota/2\pi$=1.0 resonant mode

respectively. In the case of the fixed boundary condition, the points of the closed circle remain unstable,

and the amplitude of the radial component of the displacement vector (ξ_s) at plasma boundary is zero

($\xi_{s(1)}$=0). This structure is defined as "internal mode" henceforth. In this case, the qualitative correlation

between the D_I and low-n mode is found. On the other hand, under the free boundary condition, the

domain of low-n unstable region expands wider in comparison with the fixed boundary condition. In

typical LHD plasma with low-β, the $\iota/2\pi$=1.0 and 0.5 resonance surfaces are inside plasma. However,

$\iota/2\pi$=1.0 surface disappears under high-β. The equilibrium shown by stars do not have the resonant surface

of $\iota/2\pi$=1.0. In this situation, the displacement vector at ρ=1.0 has the meaningful value and this mode

structure is defined as "external mode" henceforth. The ξ_s profile of an external mode has a structure with a

dominant m/n=1/1 contribution, as described in section 3.

3. Detail of mode structure and wall effect against the external mode

Figure2 shows an example of the mode structure of the external mode whose dominant mode is

m/n=1/1. The pressure profile is assumed as $p=p_0(1-\rho^2)^{0.5}(1-\rho^8)$ and β=2.73%. This profile does not have

the surface current originate from the pressure gradient at ρ=1.0. The rotational transform at plasma

boundary ($\iota_{(1)}/2\pi$) is below 1.0 (Fig.2 (d)). As shown in Fig.2 (a), the components of m/n=2/1 and 1/1

mode appear together. The amplitude of ξ_s of the m/n=1/1 mode is maximum at ρ=1.0, where it locally

indicates the tendency toward stability (D_I<0, dW>0, Fig.2(b)(c)).

On the other hand, m/n=2/1 mode shows the off-resonant mode and

its peak position is ρ=0.7. The potential energy at that position is

positive that means the stability by m/n=2/1 mode.

The external mode is stabilized under the fixed boundary

condition. TERPSICHORE is able to calculate the stability with

various wall shapes. To examine the wall effect against the mode,

the analysis of stability is carried out with the various walls whose

shapes are similar figures of the plasma boundary. Figure 3 shows

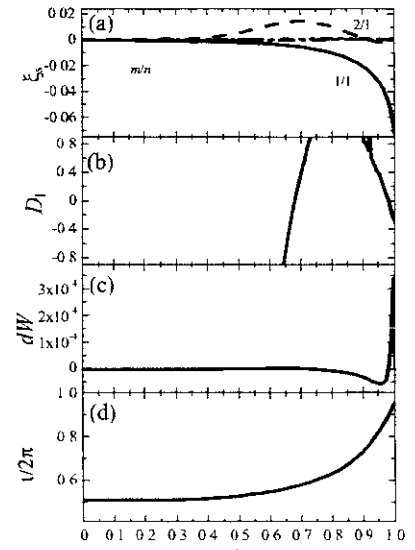the wall effect on the external mode as the dependence of the

Fig. 2 The profile of (a)ξ_s, (b)D_I (c)dW, and (d)$\iota/2\pi$.

eigenvalue on a_{wall} (the ratio of the averaged radius of the wall and the plasma boundary) with the range from 1.0 (fixed boundary) to 5.0. The growth rate is almost constant at $a_{wall}>2.0$, that is, the results are almost same as a free boundary condition. The eigenvalue decreases
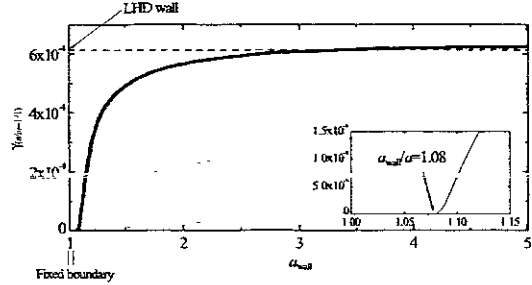

Fig. 3 Wall effect on external mode.

steeply with a_{wall} below $a_{wall}<1.5$, and finally, the external mode can be stabilized with $a_{wall}<1.08$. We also adopt a wall shape that is similar to the real LHD vacuum vessel shape. In this case, the eigenvalue is equal to the case of $a_{wall}=3.0$, which means the real LHD wall is equivalent to the case of $a_{wall}=3.0$ with regard to the $m/n=1/1$ mode so that the real LHD wall represents a nearly free boundary condition for ideal MHD stabilities.

4. The domain where external mode appears

We focus on the effect of the profile of the rotational transform, especially the value at edge $\iota_{(1)}/2\pi$. Here, we also assume $p=p_0(1-\rho^2)^{0.5}(1-\rho^8)$. To obtain the equilibrium in various $\iota_{(1)}/2\pi$, the position of the plasma boundary is changed in the calculation with VMEC. One way to produce such plasma configuration experimentally is usage of a limiter [5]. The low-n unstable region under the free boundary condition is shown in Fig.4. The points of open and closed symbol mean low-n stable and unstable, respectively. In the unstable symbols, the closed circles mean the largest amplitude of ξ_s for $m/n=2/1$ modes and closed stars for 1/1 mode. The solid and dashed lines indicates the contours of Mercier parameter with $D_I=0$, 0.2, for $\iota/2\pi=0.5$ resonant mode, respectively, and dotted line indicates the contour of $D_I=0$ for $\iota/2\pi=1.0$ resonant

mode. The contour of $D_I=0.2$ for $\iota/2\pi=1.0$ does not exist in this equilibrium region. The half-filled symbols mean low-n unstable even in the fixed boundary condition and the modes are destabilized in the Mercier unstable region with $D_I(@\iota/2\pi=0.5)>0.2$ regardless of the value of $\iota_{(1)}/2\pi$. These mode structure shows the internal mode and the main component is $m/n=2/1$ mode (Fig4.(a)). Under the fixed boundary condition, there does not exist the mode
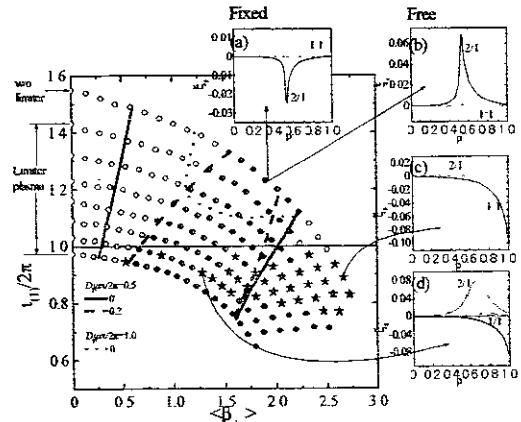

Fig.4 The unstable domain with respect to low-n mode.($n=1$ mode family).

structure in which the $m/n=1/1$ appears independently. Under the free boundary conditions, the low-n unstable area is expanded to Mercier stable and $\iota_{(1)}/2\pi > 1.0$ region more widely than the case under the fixed boundary condition. In case of $\iota_{(1)}/2\pi > 1.0$, the low-n unstable area stays in Mercier unstable region and the mode structure is similar to an internal mode (Fig.4 (b)). In case of $\iota_{(1)}/2\pi < 1.0$, on the other hand, the unstable region exists even in Mercier stable region and the mode structure clearly shows the characteristics of an external mode (Fig.4 (c)). In this case, the amplitude of $m/n = 1/1$ becomes larger than that of $m/n=2/1$. At the region with Mercier unstable and $\iota_{(1)}/2\pi < 1.0$, the mode structure has the comparable amplitude of ξ_s of $m/n = 2/1$ and $1/1$ (Fig.4 (d)). These show that the structure of an external mode, which has the meaningful $m/n = 1/1$ mode, appears in the region of $\iota_{(1)}/2\pi < 1.0$ regardless of the value of D_1 under the free boundary condition.

4.Conclusion

The low-n analysis for $n=1$ mode family is performed on the LHD plasma. The analysis with **TERPSICHORE** predicted that the external mode with $m/n=1/1$ would be unstable in the high beta region. The external mode structure, which has the $m/n=1/1$ mode, appears under the free boundary and $\iota_{(1)}/2\pi < 1.0$. The perfectly conducting wall of $a_{wall} < 1.08$ stabilizes the external mode. The real LHD wall is equivalent to the $a_{wall}=3.0$, which is almost free boundary condition. The region where external mode appears lies under the condition of the free boundary and $\iota_{(1)}/2\pi < 1.0$, even in Mercier stable and/or low-β region. If the condition with no rational surface of $\iota/2\pi=1.0$ inside the plasma can be produced, the external mode could be studied experimentally.

References

[1] S. Sakakibara, H. Yamada, K.Y. Watanabe, Y. Narushima et al., *Plasma Phys. Control. Fusion* **44** No 5A (2002) A217

[2] W. A. Cooper, *Plasma Phys. Control. Fusion* **34**, (1992) 1011

[3] S. P. Hirshman, W. I. Van Rij, and P. Merkel, *Comput. Rhys. Commun.* **43**, (1986) 143

[4] J. L. Johnson, J. M. Greene, *Plasma Phys.*, **9**, (1996) 611

[5] K. Nishimura, K. Ida, K. Kawahata, and K. Kozo et al., *Journal of Plasma and Fusion Research SERIES*, **4**, (2001) 106

Redistribution of Energetic Particles by MHD bursts
on Large Helical Device

M. Osakabe, S.Yamamoto, Y.Takeiri, J.F.Lyon[1], D.Greenwood[1], S.S.Medlay[2],

A.L.Roquemore[2], K.Ikeda, O.Kaneko, S.Sakakibara, K.Toi, K.Tsumori, K.Narihara,

K.Tanaka, Y.Oka, K.Kawahata, N.Ohyabu, and the LHD-Experimental Group

National Institute for Fusion Science, Japan
[1]Oak Ridge National Laboratory, USA
[2]Princeton Plasma Physics Laboratory, USA

1. INTRODUCTION

The confinement of fast ions is one of the most important issues on helical devices since the large helical ripple plays an important role on the topology of the fast ion orbit. Concerning on the fast ion studies on LHD, (a) the confinement of Neutral Beam Injected particles during their slowing-down processes, (b) interactions between fast ions and instabilities and/or ICRF-induced-waves, and (c) the confinement property of fast ions in the presence of electric fields are the important issues to be studied.

During the high-beta experiment with the configuration of $R_{ax}=3.6$ [m] and $Bt=0.5\sim0.75$ [T], the fast change of energetic neutral fluxes were observed on the E//B-NPA being associated with MHD burst signals which were measured by mirnov coils. These phenomena were observed during the 4th- and 5th- experimental campaign of LHD. In this paper, we will focus on the behavior of fast-ions during these phenomena.

2. Experimental Set-Up

On LHD, two of high energetic neutral beam (NB) injector was in operation during the 4th-experimental campaign. They are based on negative-ion sources, thus they have only single energy components. Each injector has two ion-sources. The injection energy of the beam was designed to be 180keV. The beam power was about 1.3MW per single ion-source. The Beam is injected into co- and counter- direction, respectively. From the 5th-campaign, additional 3rd-NB injector was installed to the counter-direction and started its operation.

The Princeton-type E//B-NPA was installed on the tangential-port of LHD to examine the confinement property of fast ions produced by NBI. The energy range of the NPA covers from 0.5[keV] to 180[keV] for Hydrogen, which is sufficient for NB-particle measurement on LHD.

3. MHD induced neutral flux increase

During the high beta campaign
of LHD, the sudden increases of
neutral flux being associated with the
MHD burst were observed at
E//B-NPA as shown in Fig.1. The
magnetic filed strength was 0.5-T and
the direction of the field is reversed
compared to the standard
configurations, thus the NPA was
observing the co.-rotating particles.
The high energy component (132-keV)
of the neutral flux was increased at the
time bin when the MHD-bursts were
observed. The flux increase of lower
energy components occurred
simultaneously and/or after the
increase of high energy components of
the signals. Since the fast neutral
particle measurement is the result of
the product between the ion
density($n_i(E)$) of interested energy and
the density of low energy neutrals
which is coming from the plasma
periphery, we must be care full about
on which components MHD-bursts had
their influences. If MHD-bursts had

Fig.1   Typical wave forms of dischrarges where
neutral flux increases associated MHD bursts were
observed. a)Stored energy (black lines with closed
circles), Deposition power of co.-Neutral Beam (blue
lines with open circles), that of counter.-NB (purple
lines with closed squares) and radiation power (green
lines with open squares) are shown. b) Line averaged
electron density (blue lines with open circles) and
H-alpha signals are shown. c)Magetic fluctuation
signals (B_θ) measured by a Mirnov-coil is shown.
d)-f)Neutral Flux signals measured by E//B-NPA for
86-keV, 113-keV, 132-keV and 151-keV are shown by
lines with open circles, closed circles, open squares, and
closed squares, respectively.

influences on the peripheral neutral density, the effect should also appear on the H-alpha
signals and the influences on NPA-signals should not have the time delay depending on the
fast neutral energy.   Therefore, the flux increase of the fast neutral was considered to be the
result of the change of the fast ion populations in plasmas.

The dominant component of the MHD bursts was TAE whose toroidal mode number(n) was 2 and poloidal mode number(m) was 3 or 4. The frequency of the mode was changing quickly during the bursts as shown in Fig.2(b). This mode was typically observed when the fast neutral flux increase was observed with a MHD-burst. The small deviation in plasma stored energy was also observed. This phenomena is more clearly seen in the time derivative of the plasma stored energy as shown in Fig.2(a) and might indicate that the degradation of the NB heating efficiency by the TAE[1].

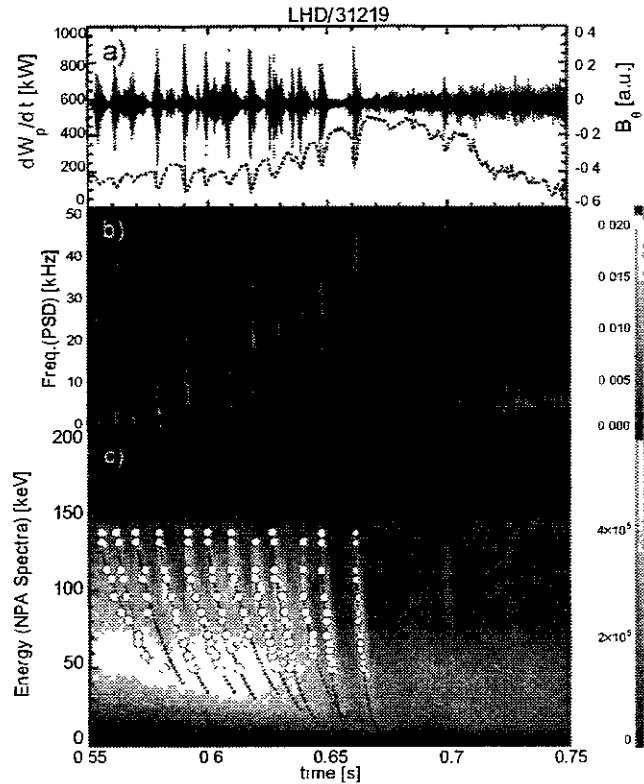In Fig.2(c), the spectra of the E//B-NPA are shown by a

Fig.2 a) dW/dt and mirnov signals are shown in dashed and solid lines, respectively. b) Power Spectrum Density of Mirnov signals are shown. c) E//B-NPA spectra are shown by pixel intensities. The circles indicate peak positions of the flux increase at each energy channels. Dashed-lines show the result of exponential fitting of peak positions for each flux increase.

2-dimensional image. The energy decay of the increased flux was more clearly seen in this figure. The energy decay time of each increased flux was evaluated by the exponential fitting of peak positions at energy channels of the NPA and was compared to the line averaged electron densities. As shown in Fig.3(a), the energy decay time is inverse proportional to line averaged electron densities. This result suggests that the energy decay itself was the result of classical slowing-down process, since the electron temperature stayed almost const during this period of the discharge. To evaluate the slowing-down time of the particle which was detected by the NPA, a series of orbit following calculation was performed by taking the launching points of the calculations on the NPA line of sight and by using the electron temperature and density profile of the discharge. In Fig.3(b), the result of the calculation were shown for the particle which are traveling at ρ_{avg} between 0.51 and 0.64, where the ρ_{avg} express the particle's location in plasma minor radius being averaged along the orbit. In this figure, the time with which the particle of 86-keV spend to lose its

energy down to 54-keV are shown as slowing-down time. The slowing-down time of the particle rotating around $\rho_{avg} = 0.55$ seems to well express the experimental observations. By comparing the slowing-down time distribution to the energy decay time of the increased flux, the location where the fast ion population increased was evaluated and is shown in Fig.3(c). There seems to be the phenomena had a preference to occur at $\rho_{avg} = 0.55$.

4. SUMMARY

Fast Neutral Flux increases being associated with MHD bursts were observed by the tangential NPA on low field LHD-plasmas. The flux increase was caused by the increase of fast ion population on the NPA line of sight. It is turned out the increase at the high energy of around 130keV was induced by MHD-burst and the increase at the lower energy is the

Fig3. a) Comparison of energy decay time of the flux increase to line averaged electron density. b)The slowing-down time of co.-passing particles rotating at $\rho_{avg.}$=0.513, 0.526, 0.553, 0.594, and 0.646 are shown by short dashed lines, solid lines, long dashed lines, long center dotted lines, and short center dotted lines, respectively. Solid lines with open circles show the energy decay time of increased neutral flux. c) The evaluated location where the fast ion increase was occurred is shown

result of the energy slowing-down of the MHD induced increase at high energy. The MHD-induced increase of fast-ion population had a preference of being occurred at ρ_{avg} of arround 0.55.

The further analysis is necessary for the identification of the mode of MHD-bursts which induces the change of fast ion population and for the driving mechanism of the mode. The TAE of n=2 and m=3 or 4 is the most probable candidate.

References

[1] S.Yamamoto, et.al, presented at this conference.

Spatially Resolved Measurements of Energetic Neutral Particle Distributions in the Large Helical Device

J.F. Lyon[1], S. Murakami[2], P.R. Goncharov[3], T. Ozaki[2], D.E. Greenwood[1], S. Sudo[2]

and LHD Groups I/II[2]

1) Oak Ridge National Laboratory, Oak Ridge, TN 37831-8072, USA
2) National Institute for Fusion Science, Toki, Gifu 509-5292, Japan
3) Graduate University for Advanced Studies, Hayama, Kanagawa, 240-0193, Japan

Abstract. A silicon-detector-based neutral particle analyzer (SDNPA) was used to study the fast ion distribution in the Large Helical Device (LHD) for different plasma heating conditions. The GNET code simulations of the SDNPA measurement are needed for more accurate interpretation of the SDNPA data.

I. THE MEASUREMENT

The liquid-nitrogen-cooled SDNPA measures the energetic (> 10 keV) neutral flux with an energy resolution of 1-1.5 keV along six horizontal viewing chords, directed as shown in Fig. 1. The pitch angles corresponding to the six different lines of sight cover the range 38° to 73°, as shown in Fig. 2. Each detector sees a nearly constant pitch angle. A vertically movable collimating aperture provides a full two-dimensional scan of the non-axisymmetric plasma.
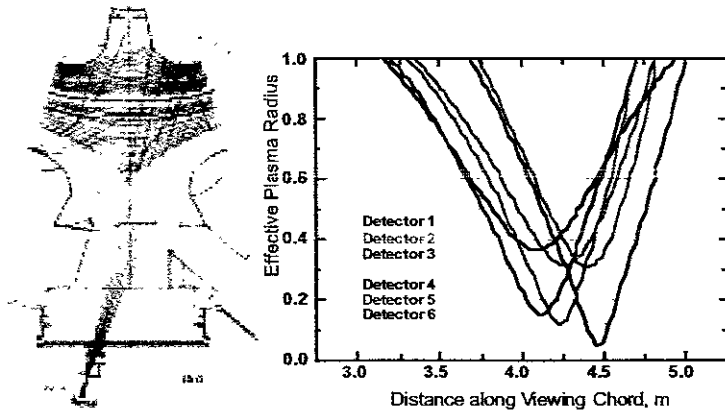
Fig. 1. Viewing geometry for the SDNPA.
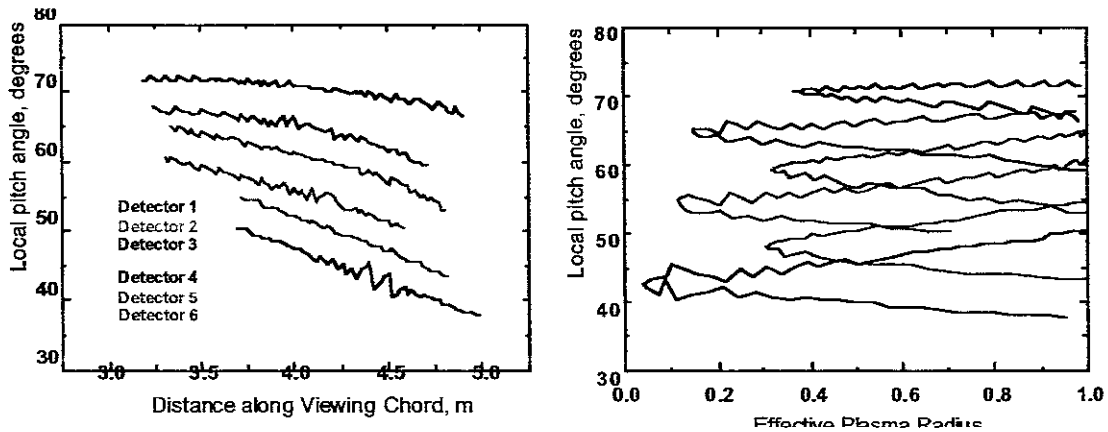
Fig. 2. Pitch angle distributions along viewing chords and plasma radius.

An insertable Be foil also allows the SDNPA to be used as a soft X-ray spectrometer and to separate the X-ray background from the charge-exchange flux. Figure 3 shows the spectra obtained for two ECH shots, with and without a 13-μ Be filter to stop charge-exchange neutrals.
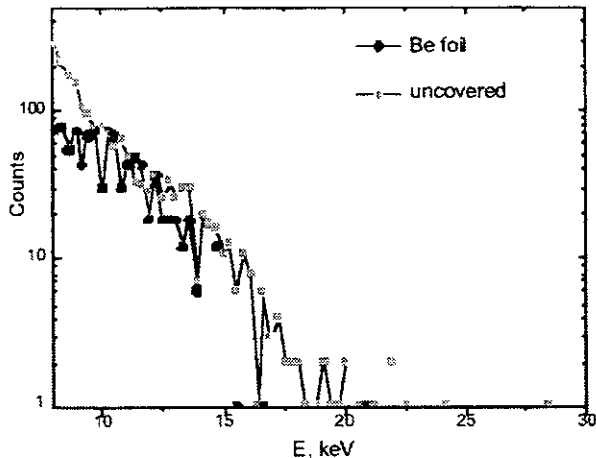

Fig. 3. Soft X-ray spectra measured by the SDNPA.

II. FAST ION MEASUREMENTS

Measurements were made on LHD for a variety of experimental conditions: electron-cyclotron-heated (ECH) plasmas with ECH powers up to 1.7 MW; ion cyclotron heating (ICH) with ICH powers up to 2.7 MW; and neutral beam injection (NBI) heating up to 7 MW. The relationship of the SDNPA viewing lines to the NBI paths is indicated in Fig. 4. Co-injection is in the clockwise direction, so NB 2 is aimed in the co-injection direction and NBs 1 and 3 are aimed in the counter-injection direction. Consequently, fast ions in the plasma from
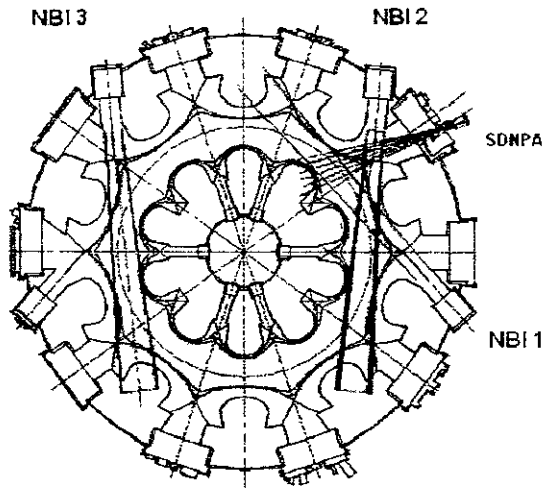
Fig. 4. Relationship of NBs and the SDNPA.

NBs #1 and #3 must back scatter to be detected by the SDNPA while fast ions in the plasma from NB #2 only need to scatter over a smaller angle. Figure 5 illustrates this point; detector 6, which is aimed closer to the NB #2 direction, sees a broader energy distribution
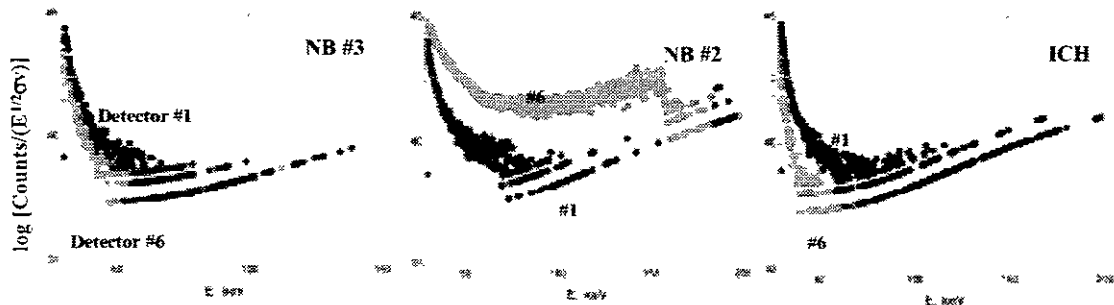

Fig. 5. Fast ion distributions from NBI and ICH.

than detector 1, which is aimed closer to the perpendicular. The opposite is true for the oppositely-directed NB #3 and ICH, which heats closer to the perpendicular direction.

III. EFFECT OF MAGNETIC AXIS SHIFT

Figure 6 illustrates the dependence of heating efficiency on shift of the magnetic axis for plasmas with NB #1, NB #3, and ICH, which favor detector 1 over detector 6. Plasmas shifted inward in major radius have improved ion confinement while plasmas shifted out have poorer confinement but theoretically improved MHD behavior. A cleaner illustration of this effect is given in Fig 7. where the only plasma heating is from NB #2. The fast ion energy distribution is again broader for the plasma that is shifted further inward.
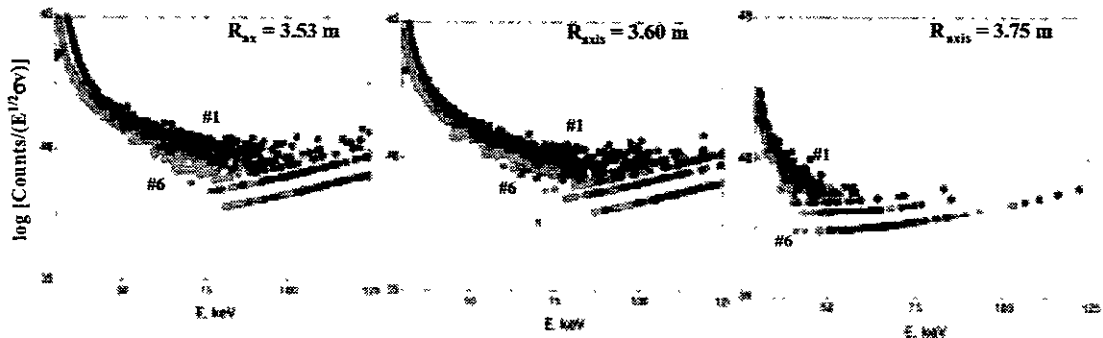
Fig. 6. Fast ion distributions for different shifts of the magnetic axis.
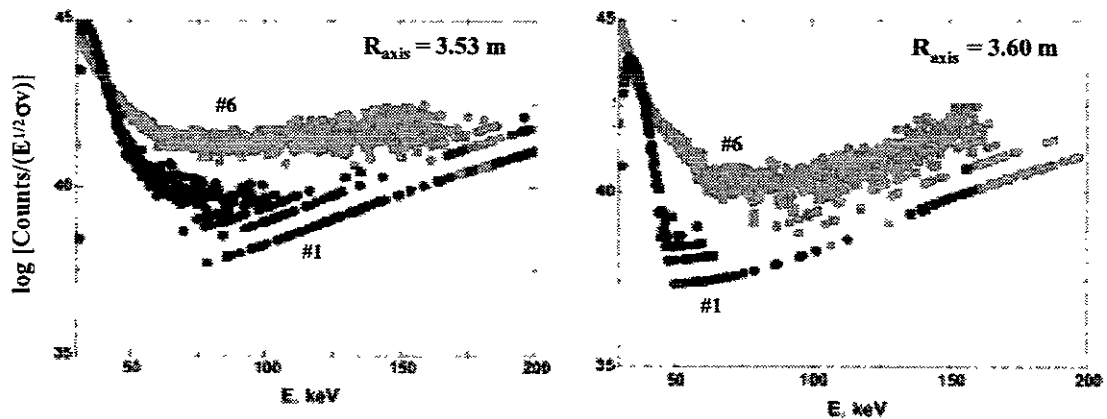
Fig. 7. Fast ion distributions for NB #2 for two shifts of the magnetic axis.

Another effect that enters by the shift of the magnetic axis is the different plasma radii seen by the SDNPA. Figure 8 shows the difference for $R_{axis} = 3.53$ m and $R_{axis} = 3.75$ m for slightly different vertical scan positions. Accurate interpretation of the SDNPA data requires modeling of the charge-exchange flux from the plasma taking the magnetic geometry into account.
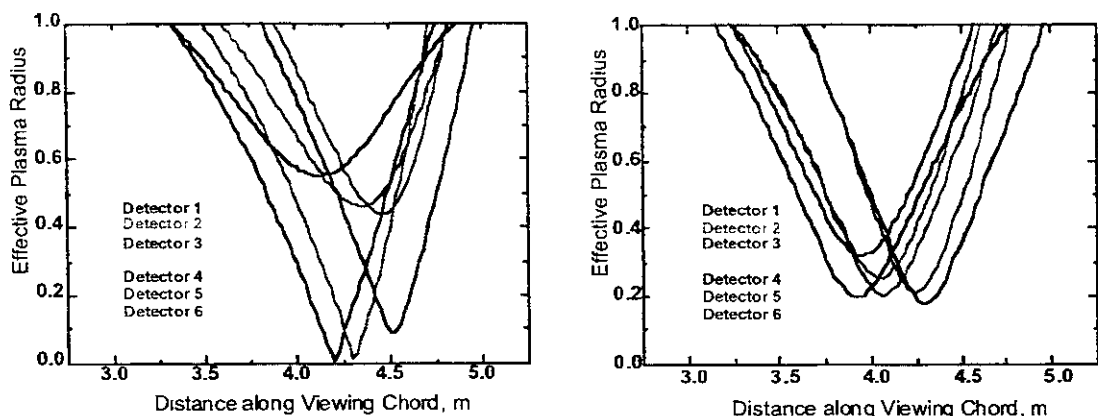
Figure 8. Viewing paths for $R_{axis} = 3.53$ m (left) and $R_{axis} = 3.75$ m (right).

IV. SIMULATION OF SDNPA MEASUREMENTS

The GNET [2] code solves the drift kinetic equation for the energetic particle distribution in 5-D phase space using a Monte-Carlo method and calculates the global distribution of the energetic ions. The fast neutral particle flux to the SDNPA detectors can be simulated from the calculated distribution. Figure 9 shows the GNET code results for a particular shot with $R_{axis} = 3.75$ m and NB #1 heating. The SDNPA data does not allow comparison with this shot because of a large soft X-ray background. However, the capability exists and the next step for the experiment will be to compare the simulated count rate with the SD NPA measurement for the same shot including the neutral density profile and attenuation of charge-exchange flux in the plasma.
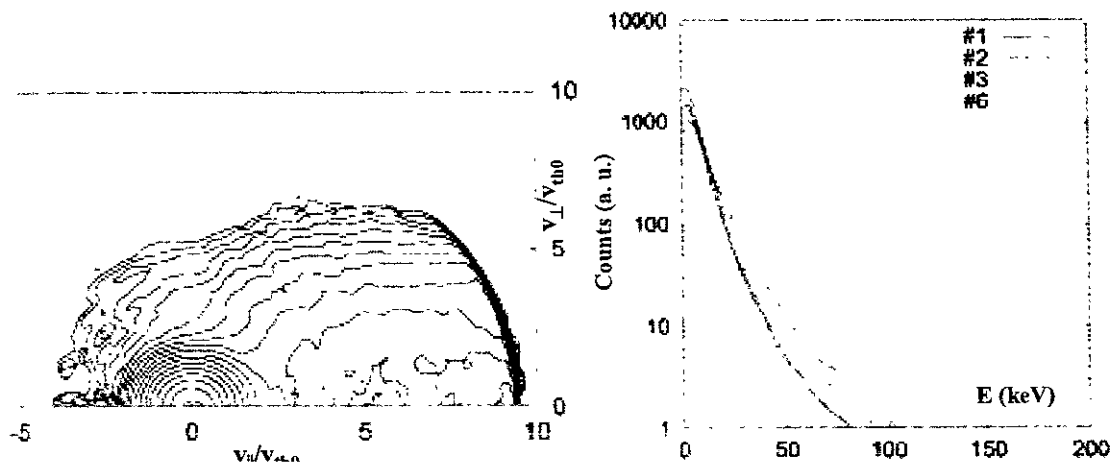

Fig. 9. GNET calculation of the fast ion distribution and simulated counts in the SDNPA.

[1] J.F. Lyon et al., *J. Plasma and Fusion Res. SERIES* 1 (1998), 358.

[2] S. Murakami et al., *Nuclear Fusion* 40 (2000), 693.

Impurity Transport Study by means of
Tracer-Encapsulated Solid Pellet in LHD

N. Tamura[1], K. V. Khlopenkov[1], S. Sudo[1], S. Kato[1], V. Yu. Sergeev[2],

S. Muto[1], K. Sato[1], H. Funaba[1] and LHD experimental groups[1]

[1]*National Institute for Fusion Science, 322-6 Oroshi-cho, Toki, Gifu 509-5292, Japan*
[2]*State Technical University, Polytechnicheskaya 29, St.Petersburg, 195251 Russia*

1. Introduction

In order to realize a practical fusion reactor, impurity particle transport is still one of the important issues. This study has been done intensely by means of an impurity injection. Conventional methods for the impurity injection, however, have essential disadvantages, such as a broad source profile of the injected impurities and an ambiguity of the total amount of those. In order to solve these problems and to promote impurity particle transport studies, a tracer-encapsulated solid pellet (TESPEL) [1] has been developed [2] and in recent Large Helical Device (LHD) experiments, the TESPEL injection has been implemented [3, 4]. TESPEL consists of polystyrene (-CH (C_6H_5) CH_2-) as an outer shell (typically ~ 0.7 mm ϕ) and tracer particles as an inner core (typically ~ 0.2 mm size). It is a unique characteristic of TESPEL to be able to produce a both poloidally and toroidally localized particle source as a tracer of a quantity that is well known. Moreover, the flexible choice of the tracer particle is one of the important characteristics with the object of the investigation of the Z-dependence of impurity transport. In LHD, metallic impurity accumulation has been found only in hydrogen discharges with a line-averaged electron density n_{e_bar} around 2.0×10^{19} m^{-3} [5]. In this paper, the quantitative transport properties of this phenomenon are investigated by means of the TESPEL with a titanium (Ti) tracer.

2. Experimental apparatus

The Large Helical Device (LHD) is the world's largest heliotron device having a superconducting $l/m = 2/10$ helical coils and 3 pairs of superconducting poloidal coils. The experiments subjected to this work were conducted under conditions of major radius $R_{ax} = 3.6$ m, a magnetic field $B_t = 2.75$ T, $n_{e\_bar} = (0.3-3.5) \times 10^{19}$ m^{-3} and the electron temperature $T_e = (1.8-2.9)$ keV. A TESPEL is injected from the outboard side of LHD by means of the pneumatic pipe-gun technique. In order to obtain the deposition feature of TESPEL, the ablation light of the TESPEL injected into LHD plasma is observed by CCD cameras and photo-multiplier tubes with corresponding interference filters for shell and tracer. In case of the Ti tracer, several Ti micro-balls (with 80-100 μm diameter) have been filled inside the TESPEL. The total amount of Ti particle was varied approximately in the $(0.5-3) \times 10^{17}$ range. The behavior of emission lines from the highly ionized Ti tracer impurity, Ti Kα ($E_{He-like}$ ~ 4.7 keV) and Ti XIX ($\lambda =$ 16.959 nm), have been observed by an X-ray pulse height analyzer (PHA) and a vacuum ultra violet (VUV) spectrometer, respectively. Two PHA systems have been used. One system (PHA2O) is

installed on the equatorial plane of LHD Port 2-O to observe the LHD plasma central chord. Another system (PHARD), which has 3 channels, is done at Port 2.5-L to observe the radial profile of X-ray emissions. The energy resolution of the PHA system is approximately 300 ~ 400 eV. Thus, the measured Ti Kα emission by these systems contains Ti Kα line emissions from several charge states.

3. Experimental results and Discussions

Figure 1 shows the dependence of the decay time of Ti Kα emission measured by the PHA2O on the line-averaged electron density for balanced NBI heated plasmas with the TESPEL injection. The decay time of Ti Kα increases gradually as the value of n_{e_bar} increases from 0.3×10^{19} m^{-3} to 1.9×10^{19} m^{-3}. There are points above 3.0×10^{19} m^{-3}, which have a considerably longer decay time. This is consistent qualitatively with the experimental results by the observations of behavior of an intrinsic impurity [5].
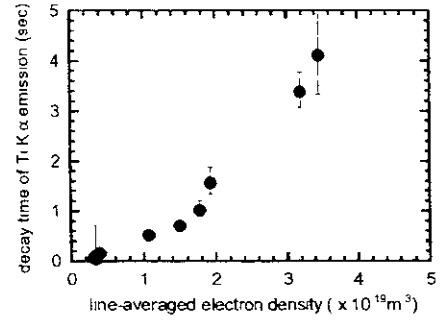
Figure 1. The dependence of the decay time of Ti Kα emission on the line-averaged electron density in the case of balanced NBI heated LHD plasmas.

In order to estimate the transport coefficients, the impurity transport code, MIST [6] has been used. A cylindrical symmetry is assumed. The radial particle flux Γ_i for the i-th charge state ion is modeled by a simple diffusive-convective model:

$$\Gamma_i = -D_i(r)\partial n_i/\partial r + V_i(r)n_i$$

, where n_i is the density of the impurity, $D_i(r)$ is the radial diffusion coefficient and $V_i(r)$ is the convective velocity, respectively. In our study, the diffusion coefficient is assumed to be a constant in time and space and the convective velocity term is represented as $V_i = - C_v(2rD_i/a^2)$, where C_v is the convection parameter, a is the averaged minor radius of plasma (here, $a = 63$ cm), and those are common among all charge states.

As seen in figure 2, the trial and error analysis with the MIST indicates that the observed behavior of the emissions of the highly ionized Ti tracer at the value of $n_{e\_bar} = 1.8 \times 10^{19}$ m^{-3} is well described by the value of $D = 1000$ cm^2/sec and $V = 0$ cm/sec, that is, the no convection. Here, the intensity of Ti Kα emission measured by the PHA2O is normalized by the value at the time when the Ti Kα emission reaches a maximum.

On the other hand, at the value of $n_{e\_bar} = 3.5 \times 10^{19}$ m^{-3}, the temporal evolution of the emissions of Ti Kα and Ti XIX is in fairy good agreement with the case of $D = 600$ cm^2/sec and $V(a) = -76$ cm/sec (see figure 3).
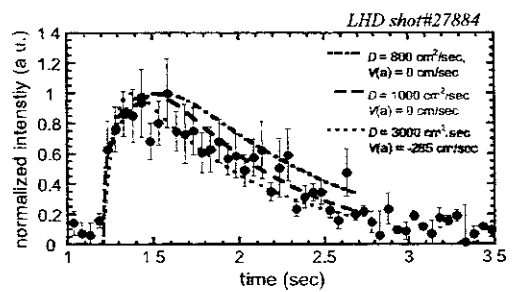
Figure 2 Comparison of normalized temporal evolution of Ti Kα emission (closed circles) measured by the PHA2O with those calculated by MIST with several sets of D and V at the value of $n_{e\_bar} = 1.8 \times 10^{19}$ m^3 (dash-dotted line. D = 800 cm^2/sec, V = 0 cm/sec, dashed one· D = 1000 cm^2/sec, V = 0 cm/sec, dotted one D = 3000 cm^2/sec, convective velocity at the plasma edge V(a) = -285 cm/sec)

From the point of view of global behavior, the Ti impurity transport with $n_{e\_bar} = 3.5 \times 10^{19}$ m^{-3} can be explained with the value of $D = (300 \sim 900)$ cm^2/sec and $V(a) = - (19 \sim 114)$ cm/sec. In this case, the inward convection should be taken into account.

We investigate the parameter space to where the plasma with the inferred convection belongs. The parameter space shown in figure 4 is defined by the electron density and the electron temperature at the peripheral region of LHD plasma ($\rho = 0.7$). The solid line in figure 4 indicates the boundary between the Banana-plateau (BP) regime and the Pfirsch-Schlüter (PS) regime. For the simplicity, this boundary is calculated with the following assumption. Firstly, the collision between the Ti impurity ion and the bulk plasma ion has been only considered. Secondly, a dominant charge state of the Ti impurity ion is helium-like. As seen in figure 4, the data point with the value of $n_{e\_bar} = 3.5 \times 10^{19}$ m^{-3} belongs to the PS regime. On the other hand, the case of $n_{e\_bar} = 1.8 \times 10^{19}$ m^{-3} belongs to the BP regime. In order to examine the experimentally deduced convective velocities, the neoclassical expressions of the radial impurity flux for axisymmetric devices are utilized for the both regimes, although it might be arguable that the one for axisymmetric devices can be utilized for non-axisymmetric devices in case of the BP regime. The radial impurity flux in the BP regime for axisymmetric devices is given by [7]

$$\Gamma_{BP} = - D_{imp} \, (n_{imp}'/n_{imp} + 3T_{imp}'/2T_{imp} -Z_{imp}n_i'/n_i -3Z_{imp}T_i'/2T_i) \, n_{imp} \quad (1)$$

, where the subscript of 'imp' and 'i' denotes the impurity ion and the bulk plasma ion, respectively. The last two terms have an important role in the case of the higher Z impurities. The inward flux could be driven by the negative n_i' and T_i' in this case. In case of the PS regime, the impurity flux is written as [7]

$$\Gamma_{PS} = - D_{imp} \, (n_{imp}'/n_{imp} - T_{imp}'/2T_{imp} -Z_{imp}n_i'/n_i +Z_{imp}T_i'/2T_i) \, n_{imp} \quad (2)$$
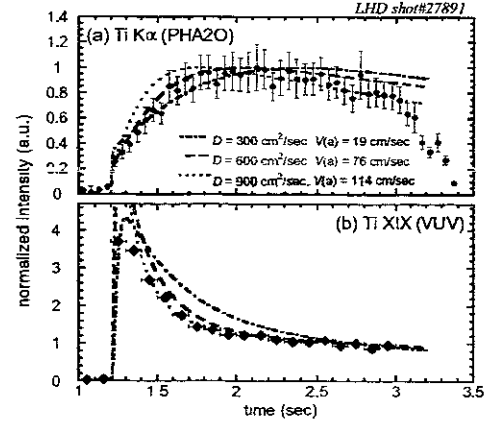

Figure 3. Comparison of normalized temporal evolution of (a) Ti Kα emission (closed circles) measured by the PHA2O and (b) Ti XIX emission (closed diamond) done by the VUV spectrometer with those calculated by MIST with several sets of D and V at the value of $n_{e\_bar} = 3.5 \times 10^{19}$ m^{-3} (dash-dotted line: D = 300 cm^2/sec, V(a) = -19 cm/sec, dashed one: D = 600 cm^2/sec, V(a) = -76 cm/sec, dotted one: D = 900 cm^2/sec, V(a) = -114 cm/sec). The balanced NBI was terminated at t = 3.3 sec.
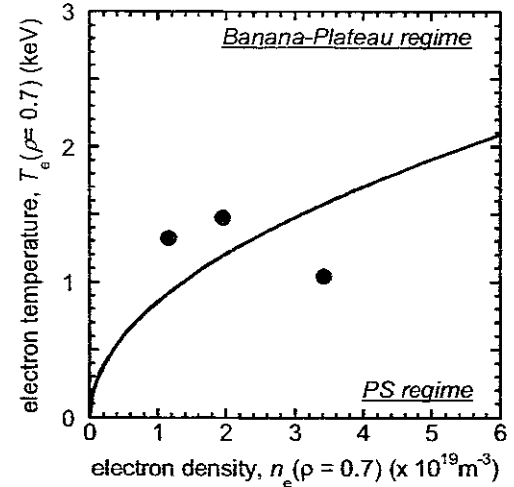

Figure 4. Data points for the transport analysis using MIST in the balanced NBI plasmas on the parameter space defined by n_e and T_e at the normalized averaged minor radius $\rho = 0.7$. The solid line indicates the boundary between the Banana-Plateau (BP) regime and Pfirsch-Schluter (PS) regime on the assumption that the collision between the Ti impurity ion and the bulk plasma ion (proton) have been only considered and the dominant charge state of the Ti impurity ion is taken as helium-like. The data point with the value of $n_{e\_bar} = 3.5 \times 10^{19}$ m^{-3} belongs to the PS regime.

In this regime, the last density term could drive the inward impurity flux. On the other hand, the last temperature term could induce the outward one. In any case, the scale length of n_i and T_i should cause the convective flux toward the center or the edge. Thus, assuming that $n_e \sim n_i$ and $T_e \sim T_i$, the scale lengths of n_e and T_e are estimated. And then the neoclassical convective velocities in the case with n_{e_bar} = 1.8 x 10^{19} m^{-3} and with n_{e_bar} = 3.5 x 10^{19} m^{-3} are calculated with the estimated values of the n_e and T_e scale lengths. In case of n_{e_bar} = 1.8 x 10^{19} m^{-3}, the convective velocity at $\rho = 0.7$, which deduced from the MIST analysis, 0 cm/sec, agree with the neoclassical one at $\rho = 0.7$, (-101.6 ± 128.7) cm/sec, within the range of the error. On the other hand, in case of n_{e_bar} = 3.5 x 10^{19} m^{-3}, the neoclassical value at $\rho = 0.7$, (52.7 ± 46.6) cm/sec has the opposite sign (the outward), compared with the experimentally deduced one at $\rho = 0.7$, -53.3 cm/sec. Therefore, the estimated convective velocity cannot be explained in case of n_{e_bar} = 3.5 x 10^{19} m^{-3} solely by the effects of the pure neoclassical impurity transport and the effect of some kind, which originates the inward flux, should be taken into account.

4. Conclusions

The quantitative transport properties of Ti impurity on LHD plasmas heated by the balanced NBI was investigated by means of the TESPEL injection. The fairly longer decay time of the line emissions from highly ionized Ti tracer was observed above the value of n_{e_bar} = 3.0 x 10^{19} m^{-3}. As a result of the MIST analysis for the higher density case, the inward convection is required to account for the experimental results, even though the absolute inward convective velocity is less than around 100 cm/sec. The comparison between the experimentally deduced convective velocities and the ones calculated by the neoclassical impurity transport has been performed. The inferred rise of the inward convection cannot be explained solely by the pure neoclassical impurity transport.

References

[1] Sudo S 1993 J. Plasma Fusion Res. 69, 1349

[2] Khlopenkov K et al 1998 Rev. Sci. Instrum. 69, 3194

[3] Tamura N et al 2001 J. Plasma Fusion Res. SERIES 4, 442

[4] Sudo S et al 2002 Plasma Phys. Control. Fusion 44, 129

[5] Nakamura Y et al 2001 Proc. 28th EPS Conf. Controlled Fusion Plasma Phys. 25A, 1481 (Funchal, Portugal)

[6] Hulse R A 1983 Nuclear Technology/Fusion 3, 259

[7] Fussmann G et al 1991 Plasma Phys. Control. Fusion 33, 1677

Evaluations of Optimal Pellet Injection Parameters and Expected Detector Signals for the PCX Diagnostics on LHD

V.Yu. Sergeev[1], O.A. Bakhareva[1], B.V. Kuteev[1], N. Tamura[2], P.R. Goncharov[2],

K.Khlopenkov[3], A.V. Krasilnikov[4], M. Isobe[3], T. Ozaki[3], M. Sasao[3] and S. Sudo[3]

[1]State Polytechnical University of St. Petersburg, 195251, Russia, e-mail: sergeev@phtf.stu.neva.ru
[2]Graduate University for Advanced Studies, Hayama, 240-0193, Japan, e-mail: ntamura@nifs.ac.jp
[3]National Institute for Fusion Science, Oroshi-cho 322-6, Toki 509-5292, e-mail: sudo@nifs.ac.jp
[4]TRINITI, Troitsk, Moscow region, 142092, Russia, e-mail: anatoli@triniti.ru

Introduction. Understanding the fast particle behavior in high-temperature magnetically confined stellarator plasmas becomes more and more important while plasma parameters grow up to the reactor-like level. A perspective active method of fast ion analysis is the Pellet Charge eXchange (PCX) diagnostics [1], which is based on ion neutralization in a pellet ablation cloud. This diagnostics has been successfully applied on TFTR for studies of fusion alpha particles and tritons [2-3] and tritium minority ions [4]. An application of the PCX diagnostics for the W7-X stellarator plasmas has been proposed in Ref. [5], considering a Li pellet cloud as a target for CX of fast ICRF-driven protons, and the Neutral Particle Analyzer (NPA) [4] as a spectrometer of escaping neutrals. In this work, simulations of signals for the PCX diagnostics on LHD, which uses lithium and polystyrene $(C_8H_8)_n$ pellets, are carried out. Along with the NPA, the Natural Diamond Detector (NDD) [6] is considered as an energy spectrometer of neutrals. Pellet ablation rates and cloud sizes in different ICRF and NBI -heated LHD regimes were simulated in order to estimate optimal pellet size and velocity as well as the detector count rate.

Pellet ablation simulations. Li and $(C_8H_8)_n$ pellet ablation rate has been simulated using the Neutral Gas and Electrostatic Shielding Model (NGESM) [5], which allows us to take into account the effect of fast particles on ablation. The heat flows of fast ICRF-driven protons and fast NBI ions were evaluated using the distribution functions obtained in the classical slowing-down approach [7,8], but for the ICRF-driven protons the characteristic slowing-down time was restricted by the energy confinement time found from the LHD scaling [10,11]. The following model parameters and assumptions have been used for the ablation simulations: 1) the electron and ion temperature profiles $T_e, T_i = T_{e0}, T_{i0} \times (1 - \rho^2)^2$ versus the effective minor radius ρ, the electron density profile $n_e = n_{e0} \times (1 - \rho^8)^2$; 2) two regimes with the following central values: $n_{e0} = 1.5 \cdot 10^{19}$ m^{-3}, $T_{e0} = 2$ keV, $T_{i0} = 0.8$ keV for Regime 1 and

$n_{e0} = 0.7 \cdot 10^{19}$ m^{-3}, $T_{e0} = 4$ keV, $T_{i0} = 2$ keV for Regime 2; 3) the minority H$^+$ ions content $\alpha = n_H/n_{He} = 0.01$ or 0.05; 4) the total ICRH power absorbed by the H$^+$ minority P_{ICRH} - 1 MW and 3 MW; 5) the deposition profile of the ICRH power - Type A and Type B, which are shown in Fig. 1 by the dotted and the solid lines correspondingly; 6) the neutral beam energy 150 keV, the port-through NBI heating power 4 MW, 20% of which is evaluated to be deposited into ions; 7) the NBI power deposition profile is proportional to n_e. The pellet size r_{p0} was chosen as that providing the electron density perturbation after injection equal to the initial electron content in the plasma. The «optimal» pellet velocity v_p^{opt} was found from the condition of pellet reaching the plasma center.

Fig. 1. The model ICRH power deposition profiles in LHD.

The pellet sizes and velocities in different LHD regimes are given in Tables 1 and 2 for Li and $(C_8H_8)_n$ pellets correspondingly.
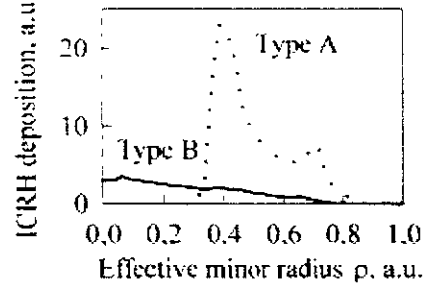
Table 1 v_p^{opt} (km/s) for Li		Regime 1 (r_{p0} = 0.8 mm)		Regime 2 (r_{p0} = 0.62)	
		$\alpha = 0.05$	$\alpha = 0.2$	$\alpha = 0.05$	$\alpha = 0.2$
P_{ICRH} = 1 MW	Type A	0.23	0.22	0.70	0.70
	Type B	0.24	0.22	0.70	0.70
P_{ICRH} = 3 MW	Type A	0.35	0.27	0.90	0.75
	Type B	0.55	0.32	1.10	0.80

Table 2 v_p^{opt} (km/s) for $(C_8H_8)_n$		Regime 1 (r_{p0} = 0.59 mm)		Regime 2 (r_{p0}=0.46 mm)	
		$\alpha = 0.05$	$\alpha = 0.2$	$\alpha = 0.05$	$\alpha = 0.2$
P_{ICRH} = 1 MW	Type A	0.65	0.65	2.10	2.10
	Type B	0.66	0.65	2.10	2.10
P_{ICRH} = 3 MW	Type A	0.90	0.70	2.50	2.20
	Type B	1.25	0.80	2.70	2.20

From Tables 1,2 it follows that 1) the v_p^{opt} values are 2-3 times larger in the Regime 2 compared to the Regime 1; 2) the v_p^{opt} values for Type A are 1.0-1.6 times greater than for Type B, 3) ablation is stronger and v_p^{opt} is 1-2.3 times higher for regimes with greater values of P_{ICRH} and a smaller minority fraction α. An additional experimental investigation of pellet ablation in ICRF-heated LHD regimes is desirable.

Both the fast CX neutrals flux emitted from the pellet cloud and the PCX detector signal depend on the transverse cloud size. Following to Ref. [9], two estimations of the transverse cloud size have been made. The radius of the cloud plateau r_{pl} was estimated from the energy balance between the electron heat flux flowing onto the cloud from the bulk plasma and the energy required to evaporate, dissociate (if necessary), heat accelerate and ionize the evapo-

rated material. The "exponential wings" scale was also estimated as the ionization length of the ablated neutrals to the first charge state (r_{ion}). Thus, for Li pellets we obtained $r_{pl}^{Li} \sim 0.5$-1.5 mm, $r_{ion}^{Li} \sim$ 1-3 cm, while for $(C_8H_8)_n$ pellets $r_{pl}^{C.H} \sim$ 1-2 mm, $r_{ion}^{C.H} \sim$ 0.5-5 cm. For both cases, the size of the cloud plateau is small compared to the transverse decay length. This means that the slowly decaying "exponential wings" length should give a contribution to the fast particles CX. For simplicity, the cloud plateau size values were used for the PCX signals simulation. Such simplification might yield underestimated PCX signals.

Estimation of the PCX signals

The count rate of both the NPA and NDD detector depends on 1) the proton energy distribution function, 2) neutralization properties of the cloud, 3) detector parameters.
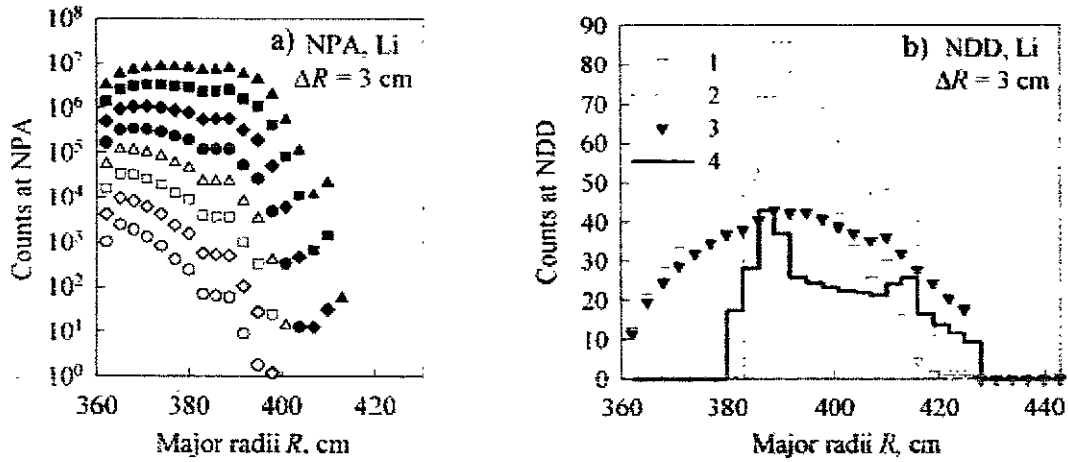

Fig. 2. The simulated counts profiles along the pellet trajectory: a) at the NPA for the Regime 1, ICRH Type B, P_{ICRH} =3 MW, α= 0.05. The symbols from upper to lower curve correspond to the neutrals energies E (and energy resolutions $\Delta E/E$) 266 keV (0.113), 322 keV (0.094), 404 keV (0.085), 498 keV (0.074), 608 keV (0.067), 727 keV (0.061), 857 keV (0.058), 1 MeV (0.056). b) at the NDD for the regimes 1) Regime 1, Type B, P_{ICRH} = 3 MW, α = 0.05, S_c= 8.5·10⁻⁸ cm², 2) Regime 1, Type A, P_{ICRH} = 3 MW, α = 0.05, S_c =7.9·10⁻⁸ cm², 3) Regime 2, Type B, P_{ICRH} = 1 MW, α = 0.2, S_c = 1.6·10⁻⁶ cm², 4) Regime 2, Type A, P_{ICRH} = 1 MW, α = 0.2, S_c = 9.4·10⁻⁷ cm². The magnetic axis is at R=360 cm, separatrix is at R=446 cm.

In the current simulations, eq. (4) from Ref. [5] was used for the count rate calculation. The H⁺ distribution function was taken from Ref. [7]. The fraction of neutralized protons was calculated using the CX cross-sections of H⁺ and H⁰ in a 100% Li⁻ and in a (25% C¹⁺, 25% C²⁺, 50% H⁰) clouds. For details and for the detector parameters see Ref. [5, 6]. For Li clouds, the count rate profiles over the time intervals $\Delta t = \Delta R/v_p^{opt}$ (here the spatial resolution ΔR = 3cm and v_p^{opt} is given in Table 1) are shown in Figs. 2a and 2b for the NPA and NDD detectors correspondingly. The signal in Fig. 2a might be well detectable by the NPA. In the case of $(C_8H_8)_n$ cloud, the NPA signal is an order of magnitude greater. The profiles in Fig. 2b were obtained with the restriction on the area of the NDD collimating aperture S_c, which

should provide the count rate below the maximum acceptable value at a 3 cm desired spatial resolution. The values in Fig. 2b are essentially less than the count rate necessary for the energy spectrum with good statistics (1000-2000 counts). Therefore, achievement of a good statistics over the whole energy range together with acceptable spatial resolution seems to be a technical problem for the NDD operating with analog spectroscopy electronics at count rate up to 10^6 cps.

Summary. The ablation behavior of lithium and polystyrene pellets has been simulated in various LHD He plasma regimes with ICRF driven H^- minority. The simulations showed that for pellet penetration to the plasma core it is preferable to inject pellets in regimes with higher plasma density and lower plasma temperature, with lower ICRH power, with a larger minority fraction, and when the ICRH power is deposited closer to plasma periphery. Li pellets of 1.2-1.6 mm in size and with 0.2-1.1 km/s velocities can provide a core pellet penetration in the regimes simulated. For polystyrene pellets of 0.9-1.2 mm size (with the same electron content), higher 0.65-2.7 km/s velocities are required for the core penetration. Estimations of the PCX neutrals energy spectra for LHD made for two types of detectors NDD and NPA show that for both Li and $(C_8H_8)_n$ pellets, the estimated number of the incident fast CX neutrals can be well detected by the $E\|B$ NPA with spatial resolution of about 3 cm in those regimes, where a visible effect of the ICRF driven protons on pellet ablation is expected. For the NDD at count rate up to 10^6 cps, a lack of statistics over the whole energy range is expected at an acceptable (3 cm) spatial resolution.

References

[1] R.K. Fisher, *et al.* Fusion Technol. **13** (1988) 536.

[2] S.S. Medley, *et al.* Rev. Sci. Instrum. **67** (1996) 3122.

[3] J.M. McChesney, *et al.* Rev. Sci. Instrum. **66** (1995) 348.

[4] M.P. Petrov, *et al.* Phys. of Plasm. **6** (1999) 2430.

[5] V.Yu. Sergeev *et al.* IPP Report 10/20, January 2002.

[6] A.V. Krasilnikov *et.al.* Nucl.Fusion, **39** (1999) 1111. See also P.R. Goncharov *et al.* in this conference.

[7] T.H. Stix, Nuclear Fusion **15** (1975) 737.

[8] D.E. Post, *et al.* Journal of Fusion Energy, Vol. 1,No. 2, 1981.

[9] B.V. Kuteev, *et al.* Journal of Technical Phys., Vol. 72, No. 8, 2002.

[10] M. Fujiwara, *et al.* Plasma Physics and Controlled Fusion **41** (1999) B157-B166.

[11] H. Yamada, *et al.* Plasma Physics and Controlled Fusion **43** (2001) A55-A71.

Formation of Dissipative Vortex and Anomalous Viscosity in a Rotating Plasma

M.Y. Tanaka, K. Nagaoka[1], A. Okamoto[1], K. Hara[1], S. Yoshimura, and M. Kono[2]

National Institute for Fusion Science, Oroshi, Toki 509-5292, Japan
[1]Graduate School of Science, Nagoya University, Nagoya 464-8602, Japan
[2]Faculty of Policy Studies, Chuo University, Hachioji, Tokyo 192-0393, Japan

Abstract

A vortex with a deep density-cavity in its center, "plasma hole," has been observed in a rotating magnetized plasma. The flow velocity field and vorticity distribution of the plasma hole are experimentally determined. It is found that the plasma hole is identified as a Burgers vortex and the plasma exhibits anomalous viscosity. This is the first experimental observation of a dissipative vortex in a plasma.

1. Introduction

Plasmas of interest in the research of vortex dynamics are conservative or nearly conservative systems so far, and are close to or equivalent to two-dimensional Eulerian fluids. In real plasmas, however, effects of instability and dissipation might play an important role on the formation of vortices. We have shown that a spiral drift-vortex is generated in a rotating magnetized plasma, and the origin of spiral nature is attributable to the existence of instability. [1,2] On the other hand, the effect of dissipation on vortex formation has not been fully understood. Since macroscopic flow structures excited in a plasma with dissipation (due to viscosity) are subjected to continuous energy damping due to internal friction, vortices survived under the circumstance should be a dissipative structure. Such a vortex, however, has not been experimentally observed in plasmas yet. We present in this paper the experimental results on the formation of dissipative vortex in a plasma , which is identified as a Burgers vortex.

2. Experiments

The experiments have been performed with the High Density Plasma Experiment (Hyper-I) device at National Institute for Fusion Science. Hyper-I is a linear plasma device (30 cm in diameter and 200 cm in length) with ten magnetic coils. The plasmas are produced by electron cyclotron resonance heating, using a microwave of frequency 2.45 GHz and of maximum power 15 kW. The magnetic field configuration is a so-called magnetic beach structure (1.25 kG at z=30 cm, 875 G at z=100 cm). [3] The typical electron temperature and density are 20 eV and 1×10^{12} cm^{-3}, respectively. We have observed a cylindrical density cavity (referred to as plasma hole) in a helium plasma. The perspective image of plasma hole taken by a CCD camera is shown in Fig.1. The central dark region in Fig.1 indicates a deep density hole, the sizes of which are 6cm in diameter and more than 100cm in axial length. The plasma density in the hole region is one tenth of that in the ambient plasma, and the width of transition layer between the hole and ambient plasma is about 1.2 cm, which corresponds to several ion Larmor radii. This steep density gradient is a remarkable characteristic of the plasma hole. The space potential measured with an emissive probe is 110 V at the hole center and 30V in the ambient

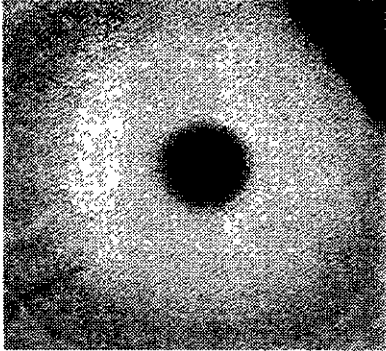plasma. There also presents a steep potential gradient in the density transition layer, and the electric

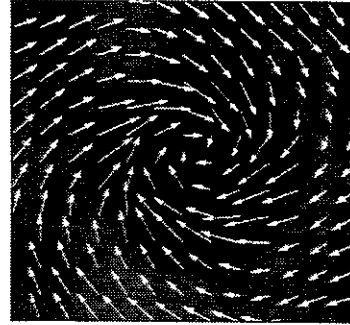Fig.1 CCD Iimage of Plasma Hole

Fig.2 Vector Field Plot of Ion Flow.

field in this region is about 40 V/cm, which induces azimuthal rotation of the plasma. Flow vector field associated with the plasma hole has been measured with a directional Langmuir probe (DLP). [4] The vector field plot of ion flow is shown in Fig.2. The flow pattern exhibits a monopole vortical structure with a sink in its center, and the velocity at the hole boundary $(r \sim 3 \, \text{cm})$ exceeds the ion sound speed. When the direction of magnetic field is inverted, the azimuthal velocity also changes its sign, indicating that the azimuthal rotation is due to $E \times B$ drift. In fact, the maximum azimuthal velocity $(\sim 3 \times 10^6 \, \text{cm/sec})$ is well explained by the $E \times B$ drift with the observed electric field (40 V/cm). On the other hand, the radial flow velocity remains unchanged when the polarity of the magnetic field is inverted. This suggests that the driving force of radial flow changes its sign with the magnetic field inversion. The most probable mechanism of occurrence of radial flow is viscous drag force originated from the shear of azimuthal velocity V_θ. This force reverses the direction with the inversion of the magnetic field, and thus the resultant $F \times B$ drift remains unchanged.

We calculate the z-component of vorticity at each point by performing the line integration defined by the following equation:

$$\omega = (rot \, v) \cdot e_z = \oint v \cdot dl / \Delta S,$$ (1)

where the integration path is taken along the minimum square passing through the neighbouring four velocity vectors, and ΔS the area bounded by the integration path. Figure 3 shows the vorticity distribution as a function of radius, where the error bars correspond to the dispersion of the data, and the closed circles indicate the average values. It should noted that the vorticity is localized in the central hole region, and negligible in the ambient plasma, showing a Gaussian profile represented by the solid curve.

3. Discussions

In order to understand the mechanism of vorticity concentration observed in the experiment, we consider vorticity dynamics for ion fluid. Taking a curl of the momentum equation for ion fluid in a uniform magnetic field, we obtain the following vorticity equation:

$$\frac{\partial \omega}{\partial t} + v \cdot \nabla \omega = \omega \cdot \nabla v - \omega \nabla \cdot v + v \Delta \omega,$$ (2)

where v is the kinetic viscosity. This equation is identical to that of normal fluids except a constant

vector, which comes from the ion cyclotron frequency vector $(\omega \rightarrow \omega + \Omega_{ci})$. Thus, we can discuss vorticity dynamics of ion fluid with the same physical picture as ordinary fluids.

When there presents an inward convection $(V_r = -\alpha r, \alpha > 0)$, vorticity localization may occur through the balance between diffusive process due to viscosity and concentration due to convection, generating a stationary structure. This is known as Burgers vortex. [5, 6] The vorticity profile of Burgers vortex is given by a Gaussian distribution, which is characterized by the total circulation Γ at the initial time and the scale length of the vortex l,

$$\omega(r) = \frac{\Gamma}{\pi l^2} \exp[-\frac{r^2}{l^2}],$$ (3)

where the quantity l is determined by the square root of the ratio of viscosity to magnitude of inward convection,

$$l = \sqrt{\frac{2\nu}{\alpha}},$$ (4)

The solid curve in Fig.3 indicates the best fit Gaussian profile, for which the parameters are taken to be $\Gamma = 7.7 \times 10^7 \text{ cm}^2 / \text{sec}$ and $l = 3.0 \text{ cm}$. Then, the azimuthal velocity is uniquely determined by integrating eq.(3) and is given by

$$\upsilon_\theta(r) = \frac{\Gamma}{2\pi r}\left(1 - \exp\left[-\frac{r^2}{l^2}\right]\right),$$ (5)

which behaves as $V_\theta \propto r$ (rigid rotation) for $r \ll l$ and $V_\theta \propto 1/r$ (vorticity free rotation) for $r \gg l$.
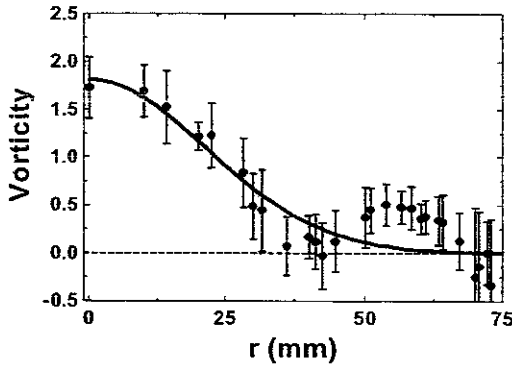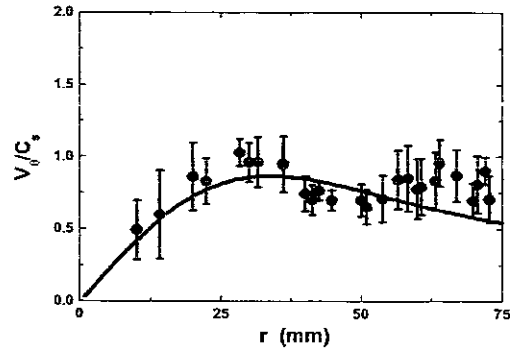

Fig.3   Vorticity Profile

Fig.4 Azimuthal Velocity Profile

Figure 4 shows the azimuthal velocity V_θ as a function of radius. The experimental results are also plotted in the figure by closed circles, showing a good agreement with the theoretical values.
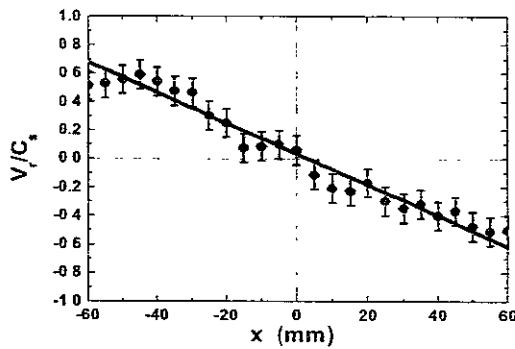

Fig.5 Radial Velocity Profile

Presence of inward convection is of essential importance on the formation of Burgers vortex, and is assumed so far. The radial velocity component as a function of radius is depicted in Fig.5, showing that there exists in fact an inward flow proportional to the radius. According to these results, the localization of vorticity observed in the present experiment is identified as a Burgers vortex. [7] Finite viscosity of fluids induces

irreversible thermalization of fluid motions due to internal friction. We have experimentally determined the radial profile of dissipation rate by using the rate-of-strain tensor $e_{\alpha\beta}$. It is found that $e_{r\theta}$ term dominates the rest of all, and 61 % of the total dissipation is produced by this term. It is emphasized that this term corresponds to the dissipation of azimuthal rotaion by internal friction. It is found that the dissipation layer is located in the periphery of the plasma hole, and the energy of vortical motion transported by viscous diffusion is finally consumed into heat in this layer. It should be pointed out that the energy dissipation undertakes stationary nature of the plasma hole, which is organized in a plasma with continuous input of energy. The plasma hole is a dissipative structure in a rotating magnetized plasma.

The viscosity coefficient v_{eff} can be estimated from the scale of vortex l and the coefficient α of inward flow using the relation eq.(4). Substituting $\alpha = 4.4 \times 10^5$ sec^{-1} from the experimental data and $l = 3.0$ cm into the above relation, we have $v_{eff} = 2 \times 10^6$ cm^2 / sec, which is four orders of magnitude higher than the classical value $v_c = 1 \times 10^2$ cm^2 / sec [8], and still one order of magnitude higher than the anomalous viscosities observed in magnetically confined plasmas.

One of possible cause of viscosity anomaly might be attributable to the breaking of quasi-neutrality in the hole plasma. Using the Poisson equation and potential data, the normalized density difference $\delta n / n$ ($\delta n = n_i - n_e$) is of the order of $(\lambda_D / R)^2$ (λ_D : Debye length, R : plasma radius), and is 10^{-3} in the hole region in contrast to that in the ambient plasma 10^{-6}. Therefore the Debye shielding is insufficient in the hole region, and the potential leaks to outside far beyond the scale of Debye length. This long range interaction might make it possible to transport momentum in azimuthal direction faster to the radial direction. Another possibility of the origin of viscosity anomaly might be attributable to turbulence induced by instability of electrostatic waves such as drift wave turbulence or lower hybrid turbulence etc., since there exists strong inhomogeneity in density profile. Unfortunately, we have not experimentally identified the origin of viscosity anomaly yet, and the detailed analysis remains for future study.

4. Conclusions

We have observed the plasma hole in a rotating magnetized plasma, and identified it as a Burgers vortex in a compressible fluid. The remarkable characteristic of the Burgers vortex in a plasma is a deep density hole with a shock-like transition layer at the boundary. The vorticity distribution well agrees with a Gaussian profile. The effective viscosity far exceeds the classical value. Although the viscosity anomaly is not fully understood yet, the implication of the present result is that plasma is much more "*sticky*" than expected. Therefore Burgers vortex as a dissipative structure will play a crucial role in structure formation in plasmas.

References

1. M. Y. Tanaka and M. Kono, J Plasma Fusion Res. SERIES Vol.4 (2001) 131
2. M. Kono and M. Y. Tanaka, Phys. Rev. Lett. **84**, (2000)4369.
3. M. Tanaka *et al.*, J. Phys. Soc. Jpn. **60**(1991)1600.
4. K. Nagaoka, A. Okamoto, S. Yoshimura, and M. Y. Tanaka, J. Phys. Soc. Jpn. **70** (2001)131.
5. L. M. Burgers, Adv. Appl. Mech. **1** (1948)171.
6. T. Kambe, J. Phys. Soc. Jpn. **53** (1983)13.
7. K. Nagaoka, A. Okamoto, S. Yoshimura, M. Kono, M.Y. Tanaka, Phys. Rev. Lett. *in press*.
8. S. I. Braginskii, in *Review of Plasma Physics Vol.1* (Consultants Bereau, New York, 1965).

Potential Structure and Quasi-neutrality Breaking of Plasma Hole

S. Yoshimura, K. Nagaoka*, A. Okamoto*, K. Hara*, M. Kono**, and M. Y. Tanaka

National Institute for Fusion Science, Oroshi, Toki 509-5292, Japan
*Graduate School of Science, Nagoya University, Chikusa, Nagoya 464-8602, Japan
**Chuo University, Hachioji, Tokyo 192-0393, Japan

1. Introduction

Electric field in magnetized plasmas drives a rotating motion by $E \times B$ drift, giving rise to macroscopic structures. Recently spontaneous formation of a cylindrical density-cavity structure, which is referred to as *plasma hole*, has been observed in a laboratory ECR plasma. [1, 2] From the viewpoint of flow structure, the plasma hole is a monopole vortex with a sink and is identified as a dissipative vortex (Burgers vortex). Since the azimuthal rotation is driven by $E \times B$ drift, the fact that the maximum rotation velocity exceeds the ion sound speed implies the existence of strong electric field, and the problem of interest is how such a strong electric field is self-generated in the plasma. In this paper, we present the results of potential profile measurement of the plasma hole. On the basis of Poisson's equation, we also present an estimation of the degree of quasi-neutrality breaking occurred in the plasma hole.

2. Experimental

The experiments have been performed with the High Density Plasma Experiment (HYPER-I) device at National Institute for Fusion Science. [3] HYPER-I is a cylindrical plasma device (30 cm in diameter and 200 cm in length) with ten magnetic coils. The plasma is produced by electron cyclotron resonance heating in a *magnetic beach*, where the microwave power is 5 kW and the frequency is 2.45 GHz. A helium gas has been used with the operation pressure of 0.6 mmTorr. Typical plasma parameters are as follows: the electron temperature is 20 eV, the plasma density $10^{10} \mathrm{cm}^{-3}$ (hole plasma) $- 10^{11} \mathrm{cm}^{-3}$ (ambient

plasma).

Floating emissive probe method [4] has been adopted to measure the plasma potential profile. The emissive probe has been constructed as follows: the emissive filament is made of a small loop of tuntalum wire (0.2 mm in diameter) welded to tungsten rods (0.8 mm in diameter), which are mounted in a two-hole ceramic insulator. The measurement circuit is grounded through a high impedance load resister. As the electron emission from the heated filament becomes sufficiently high, the probe potential comes to indicate the plasma potential directly, which has been experimentally confirmed by the I-V characteristics of the emissive probe.

3. Results and Discussions

The radial density profile measured with a Langmuir probe is shown in Fig. 1 (a). A deep density hole exists at the center of the cylindrical plasma, and this is why we call this structure *plasma hole*. The density in the hole plasma is indeed one tenth of that in the ambient plasma. A typical potential profile of the plasma hole, together with the potential profile without the plasma hole, is shown in Fig. 1 (b), in which two distinctive features can clearly be seen: (i) The potential has a *bell-shaped* structure and sharply increases toward the center, the maximum value exceeding more than 100 V, which is five times higher than the electron temperature. The drastic increase in plasma potential begins from the density transition layer (x ~ 30-50 mm), in which the density profile has the steepest gradient. (ii) There is a spatial oscillation in potential profile around x ~ 50 mm, indicating the alternation of the electric field direction. We have also measured the two-dimensional potential profile to confirm the axisymmetric profile. On the other hand, the potential profile of a plasma without any characteristic structure exhibits no spatial irregularity, and the maximum value is, as is expected, approximately equal to the electron temperature.

Since the plasma hole has the intense electric field (40 V/cm) compared to that without

plasma hole (~1 V/cm), the breakdown of charge neutrality may takes place in the hole plasma. The quasi-neutrality breaking can be evaluated from the Poisson's equation $-\nabla^2\phi = 4\pi e \delta n$, where $\delta n = n_i - n_e$. Assuming the magnitude of the potential $|\phi| \simeq T_e / e$, and the characteristic scale-length is equal to plasma radius L, we have the normalized density difference as $\delta n / n \sim (\lambda_D / L)^2$, where λ_D is the Debye length. A typical value of $\delta n / n$ for a plasma without plasma hole is estimated to be of the order of 10^{-6} under our experimental conditions ($T_e \sim 20\,\text{eV}, L = 15\,\text{cm}$ and $n \sim 10^{11}\,\text{cm}^{-3}$). It should be noted that $\delta n / n$ represents the degree of quasi-neutrality breaking, or non-neutrality, of the plasma. By taking the second derivative of measured potential profile, the value of $\delta n / n$ can be calculated directly. As shown in Fig. 2, $\delta n / n$ of the plasma without plasma hole is of the order of 10^{-6}, which coincides with the expected value from the Poisson's equation. The degree of quasi-neutrality breaking of the plasma hole is, however, considerably greater than the expected value for a plasma without plasma hole. The quantity $\delta n / n$ attains its maximum value (8×10^{-4}) within the hole plasma region (ion-rich); it is about 10^3 times higher than that of quasi-neutral plasma. In addition, the electron-rich layer can be seen in the interface layer ($x \sim 35\text{-}50\,\text{mm}$) between the hole and the ambient plasma.

4. Conclusion

The characteristic potential profile of the plasma hole has been measured with an emissive probe. The potential has a bell-shaped structure and its maximum value is five times higher than the electron temperature. The quantity $\delta n / n$ of the plasma hole has been calculated from the Poisson's equation and the potential data; it is about three orders of magnitude higher than that of the ambient plasma. It is found that the quasi-neutrality breaking occurs in the plasma hole, producing the very high potential ($\phi \sim 5T_e$) and the resultant supersonic ion flow in azimuthal motion. It is also found that the double layer structure does exist in the

transition layer between the hole and ambient plasma. The elucidation of the mechanisms of occurrence and sustainment of this quasi-neutrality breaking is left for future study.

References

[1] K. Nagaoka, A. Okamoto, S. Yoshimura, M. Kono, and M. Y. Tanaka, *to be published in* Phys. Rev. Lett. (2002).

[2] K. Nagaoka, T. Ishihara, A. Okamoto, S. Yoshimura, and M. Y. Tanaka, J. Plasma Fusion Res. SERIES 4, 359 (2001).

[3] M. Y. Tanaka, M. Bacal, M. Sasao, and T. Kuroda, Rev. Sci. Instrum. 69, 980 (1998).

[4] R. F. Kemp and J. M. Sellen, Jr., Rev. Sci. Instrum. 4, 455 (1966).
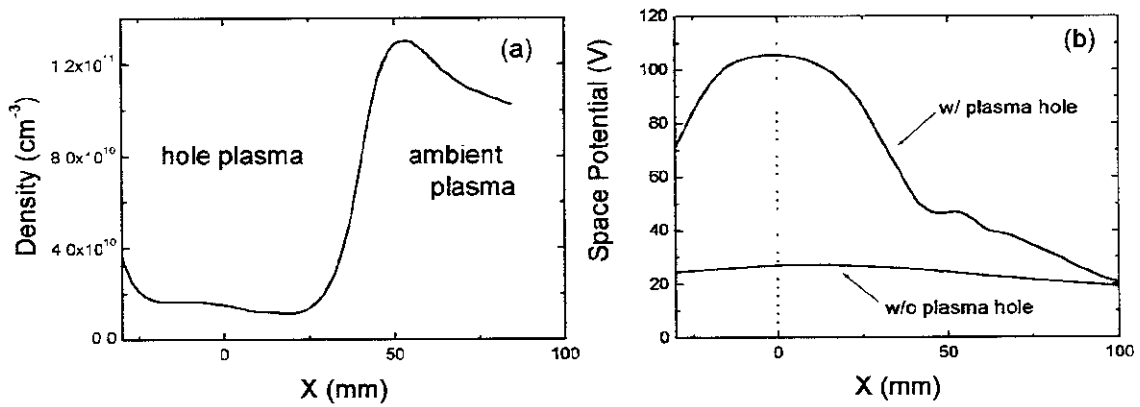
Figure 1 *(a) Density profile of the plasma hole. (b) Potential profile of the plasma hole. Potential profile without plasma hole is also plotted.*
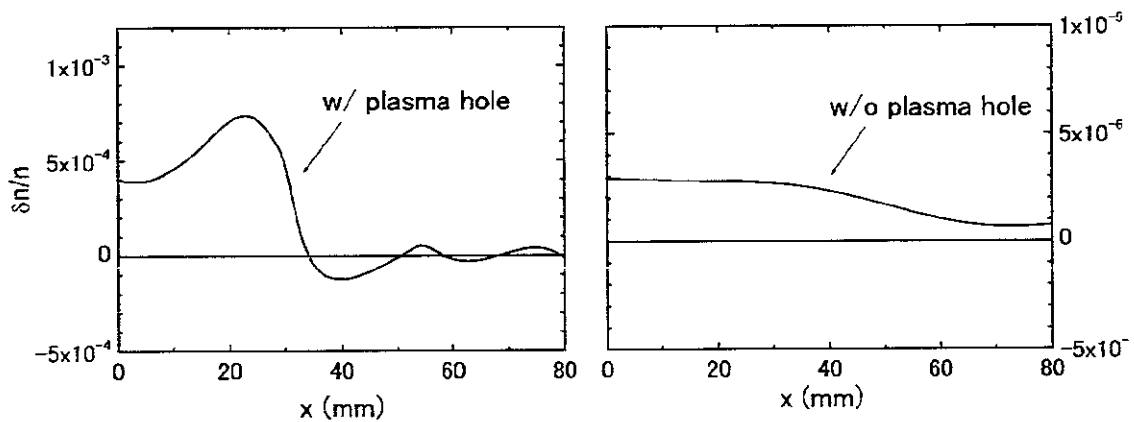
Figure 2 $\delta n / n$ *profile of the plasma hole and of ordinary plasma without plasma hole.*

P-4.06

29th EPS Conf. On Plasma Phys. & Contr. Fusion

17-21 June 2002, Montreux, Switerland

Transport Studies of Dimensionally-Similar Low-Energy-Density Plasmas in CHS Heliotron/Torsatron

K. Toi, S. Kawada[1], G. Matsunaga[1], C. Suzuki, T. Shoji[1], Y. Sakawa[1],

K. Ohkuni[2], K. Matsuoka, and CHS Group

National Institute for Fusion Science, Toki 509-5292, Japan
1) *Dep. Energy Eng. Sci., Nagoya Univ., Nagoya 464-8603,Japan*
2) *High Temp. Plasma Res. Center, Univ. of Tokyo, Tokyo 113-8656, Japan*

1. Introduction

Understanding of turbulent transport in a toroidal plasma is a very important and challenging task in magnetic confinement fusion research. Correlation measurements among plasma fluctuations are crucial to clarify underlying physics mechanisms in turbulent particle and heat transport of a toroidal plasma. In the case that electrostatic fluctuations are dominant the turbulent particle and electron heat

fluxes are respectively expressed as $\Gamma_{turb} = \langle \tilde{n}_e \tilde{E}_\theta \rangle / B_t$ and $Q_e = \frac{3}{2} (T_e \langle \tilde{n}_e \tilde{E}_\theta \rangle + n_e \langle \tilde{T}_e \tilde{E}_\theta \rangle) / B_t$, where

$\tilde{n}_e, \tilde{T}_e$ and $\tilde{E}_\theta$ are fluctuations of electron density, electron temperature and poloidal electric field, and B_t is the toroidal magnetic field strength. However, the correlation measurement is extremely difficult in high temperature plasmas, except for the measurements with Langmuir probes in the plasma edge region. If the transport behaviours in a high temperature plasma is simulated by those in a cold and low density plasma, detailed studies of turbulent transport are possible in such low energy density plasma with aid of Langmuir probes and may provide a knob to clarify unknown transport mechanisms. When the relevant dimensionless plasma parameters such as ν_* (effective collision frequency), β_t (toroidal beta) and relative scale length of density and temperature profiles except for ρ^* (normalized gyroradius) are the same in two kinds of plasmas, these two plasmas are "dimensionally similar" each other and their plasma transport is expected to be similar[1,2]. Based on this hypothesis, we have started a new simulation experiment on high temperature plasma transport using low energy density plasma obtained at low toroidal field (B_t <0.1 T) in CHS heliotron/torsatron. Main objectives of this new experimental campaign are as follows, (1) to compare fluctuation characteristics of both plasmas, (2) to obtain improved confinement regimes observed in hot plasmas and clarify physics mechanisms of turbulence suppression, and (3) to establish realistic transport model in a toroidal plasma through detailed comparison between experimental data and numerical simulations. In CHS, we intend to produce low energy density plasmas at low toroidal field (B_t ~0.09T) with 2.45GHz microwaves (up to 20 kW) and/or 9 MHz helicon waves(up to 100kW). The electron density from 10^{16} m^{-3} to 10^{19} m^{-3} and the electron temperature from 5 eV to 100 eV are expected in low energy density plasma, where the expected effective collision frequency ν_* (=0.01-1) and toroidal beta

β_t (= 0.01 – 1 %) are comparable to those in high temperature plasmas at $B_t \geq 0.9$T

2. Plasma parameters in an initial experiment

An initial experiment presented here was performed in so-called outward-shifted plasmas produced with up to 1 kW ECH.   In these plasmas the toroidal beta value is still very low

(β_t =0.002%), but $v*$ and p^* are comparable to those in CHS plasmas at $B_t \geq 0.9$T.   This plasma is

not dimensionally similar to that at high magnetic field.   Nevertheless, it is interesting and important for this new experimental project to investigate characteristics of electrostatic fluctuations in the plasma. Plasma parameters and their fluctuations were measured with a triple probe [3].   Radial profiles of electron density n_e, electron temperature T_e and plasma potential V_s in a plasma produced by 0.4 kW ECH are shown in Fig.1(a).   The density profile is slightly hollow and electron temperature has a very flat profile, where ECR layer is located at the magnetic axis.   This hollow ne-profile is very similar to the ECH plasma obtained at high magnetic field ($B_t \geq 0.9$T).   In Fig.1(b), the radial profiles of the radial electric field Er and its shear Er' are also shown.
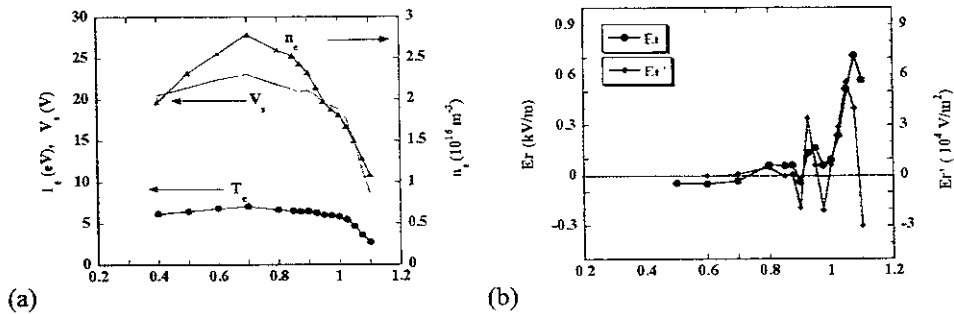
Fig.1 (a) Radial profiles of electron temperature, density and plasma potential in a plasma produced by 0.4 kW ECH at Bt=0.0875T. (b) Er and Er' profiles derived from Vs.

3. Characteristics of electrostatic fluctuations

In Fig.2, we compare power spectra of ion saturation current and floating potential in the plasma edge (p~1) of a low energy density plasma produced by 2.45 GHz ECH at B_t~0.09 T and NBI heated plasma at B_t~0.9T, where ECH and NBI powers are respectively to be 0.4 kW and 500 kW.   Although
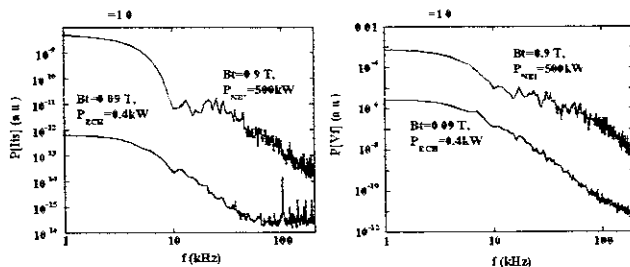
Fig.2 Comparison of frequency spectra of edge fluctuations measured at p ~1 for 0.4 kW ECH plasma and 500 kW NBI plasma, where P[Iis] of the ECH plasma is in the noise level in the range of f>70 kHz.

the magnitude of the spectral power of the NBI plasma is by three or four orders magnitude larger than that of ECH plasma, both spectra have a very similar turbulent character without clear coherent modes.

In this low energy density plasma, fluctuations can be measured even in the plasma core region with LP, as shown in Fig.3. All fluctuations of n_e, T_e and V_s are increased rapidly from $\rho \sim 0.7$ toward the edge. That is, the relative amplitudes of n_e, T_e and V_s fluctuations are respectively ~5%, ~5% and ~1% at $\rho \sim 0.6$, and ~13%, ~7% and ~23% at $\rho \sim 0.9$. That is, the n_e-fluctuation level is two time larger than that of T_e. These features are very similar to that of edge turbulence in tokamak and helical plasmas[3-5]. Note that a reduction in these fluctuations is seen just inside the last closed flux surface. In this edge region, the radial electric field shear is fairly small ($Er' \sim 2\text{-}3.5 \times 10^4 V/m^2$) as shown in Fig.1(b), but the poloidal velocity shear is fairly large ~2.3-4x10^5 1/s) because of low magnetic field(B~0.09T). This reduction is also similar to that in the edge region of the TEXT ohmic plasma [6].
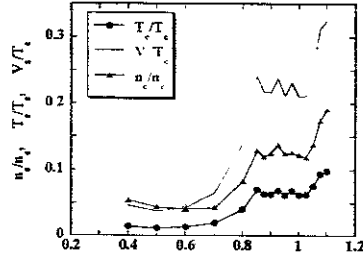
Fig.3 Radial profiles of the relative amplitude of Te, ne and Vs fluctuations.

Frequency spectra of these fluctuations in the scrape-off layer($\rho \sim 1.1$), edge ($\rho \sim 0.9$) and core ($\rho \sim 0.6$) are shown in Fig.4. Spectral power of n_e-fluctuations is concentrated less than ~50 kHz in the edge region and less than 30 kHz in the core region. On the other hand, the spectra of T_e and V_s fluctuations extend to relatively high frequency range more than 100 kHz in the core region as well as the edge. The turbulent particle flux Γ_{turb} is obtained from the correlation between n_e-fluctuations and poloidal electric field (E_θ) fluctuations which are derived from the difference of the floating potential signals at two points separated poloidaly by 6 mm. That is, the effect of T_e-fluctuations was neglected in the present analysis. The frequency spectrum of Γ_{turb} is concentrated in the low
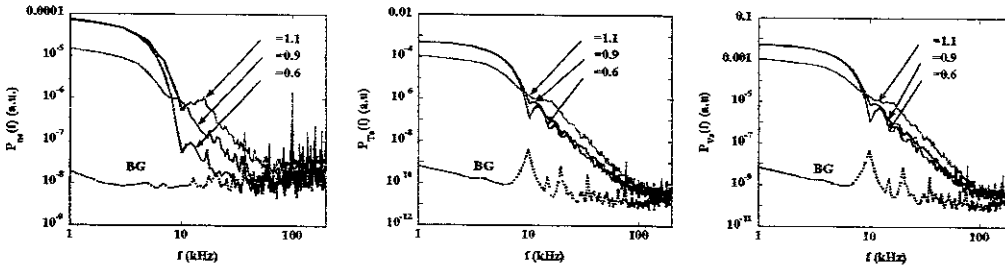

Fig.4 Frequency spectra of ne-, Te- and Vs-fluctuations for different radial locations at ρ=0.6(red), ρ=0.9(blue) and ρ=1.1(green). The black dotted curve denotes the noise level(BG).

frequency range less than ~20kHz.   Note that the phase difference between ne- and E_θ - fluctuations is nearly 0 degree over the range of 100 kHz in the region of 0.4≤ρ≤.1.1.   The radial profile of the particle flux integrated in the frequency region Γ_{turb} is shown in Fig.5.   The turbulent particle flux is localized in the edge region from ρ~0.8 to ρ~1.1.
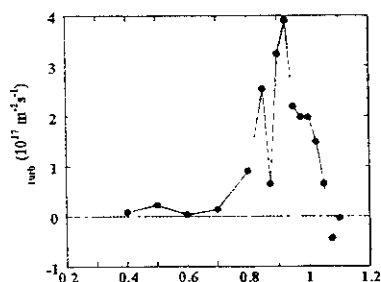

Fig.5 Radial profile of turbulent particle flux.

4. Summary

Characteristics of plasma profiles and fluctuations in a low density and low temperature plasma produced with ≤1 kW ECH at B_t~0.09T were investigated in CHS.   Although the beta value of this plasma is very low as β_t ~0.002%, the other two parameters ρ^* (~0.07)   and v^* (~0.9) are similar to those in a high temperature plasma obtained at high magnetic field (B_t≥0.9T).   Radial profiles of relative amplitude of n_e-, T_e-, and V_s fluctuations, power spectra of the ion saturation current and floating potential also exhibit similarity to those in high temperature plasmas.   Even this preliminary experiment suggests a potentiality that transport characteristics might be simulated with those in a low energy density plasma obtained at low magnetic field condition (B_t≤ 0.1T).   Experiments with 2.45GHz ECH of ~20 kW and/or helicon wave heating of ~100kW are required in order to adjust similar values of relevant dimensionless plasma parameters such as v^*, β_t, ρ^* and the relative scale length of density and temperature profiles, and to proceed detailed comparison of transport characteristics with those of high temperature plasmas.

References

[1] B.B. Kadomtsev, Sov. J. Plasma Phys.1, 295(1975).

[2] R.E. Waltz et al., Phys. Rev. Lett. 65, 2390(1990).

[3] K. Ohkuni, K. Toi et al., Phys. Plasmas 8, 4035 (2001).

[4] Ch.P. Ritz et al., Phys. Rev. Lett. 62, 1844(1989).

[5] B.A. Carreras, IEEE Trans. Plasma Sci. 25, 1281 (1997).

[6] Ch.P. Ritz et al., in Proc.13th IAEA Conf. On Plasma Phys. Contr. Fusion Res. (Washington D.C., 1990), Vol.2, IAEA, Vienna 589.

SPATIAL DISTRIBUTION OF HIGH-ENERGY PARTICLE NBI AND ECH PLASMAS OF LARGE HELICAL DEVICE

T.Ozaki, P.Goncharov[i], S.Murakami, T.Watanabe, S.Sudo and G1/G2 Group

National Institute for Fusion Science, Toki, Gifu 509-5292, Japan
[i] *Graduate Univ. for Advanced Studies, Hayama, Kanagawa, 240-0193, Japan*

1. Introduction

In the helical devices, the particle orbit of the NBI co-injection beam against the direction of the torus magnetic field is different from that of the counter injection. According to the calculation, the guiding center of the particle orbit is close to the magnetic axis and shifted to the high magnetic field side in the co- and counter-injection, respectively. The tendency is remarkable in the low magnetic field. On the simulation in the Large Helical Device (LHD), the spatial distribution of the particle of co-injection on the mid-plane is expanded to the entire plasma[1]. On the contrary, that of the counter-injection is localized near the high magnetic field side. Therefore the part of the particles is lost by the collision with the inner wall. The disadvantage can be overcome by the increase of the magnetic field. The difference of each orbit strongly reflects the charge exchange neutral particle flux.

In the 4th experimental campaign, NBI#1 as the counter-injection and NBI#2 as the co-injection are prepared. In 5th cycle, NBI#3 is added as the counter injection beam. NBI#1 and #3 change to the co-injection and #2 changes to the counter-injection by the inversion of the magnetic field direction in some shots on the 5th cycle.

2. Experimental Setup and Diagnostics

The time-of-flight type NPA (maximum /minimum observable energy 0.5/370keV, typical energy resolution 7%) has the capability of a high S/N ratio against the radiation
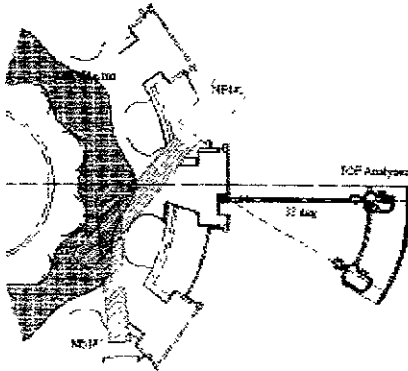

Figure 1. The experimental configuration of LHD, NBI and the neutral particle energy spectrum in LHD.

including soft/hard X-rays from plasmas[2]. The analyzer and the movable stage are installed at the mid-plane of LHD on the 10-O port. There are two NBIs (NBI#1 and #2) at neighboring ports to 10-O (Fig.1). NBI#3 is installed in the parallel direction with NBI#2 from the 5th campaign. In particular, the beam path of NBI#1 crosses the sight line of the analyzer. Therefore a large amount of particles from the plasma center can be expected, which is suitable for the high-energy distribution measurement. The

scanning is performed with the pivot in front of the 10-O port by using a motor, which is remotely controlled from -2 degrees to +31 degrees (0 degrees indicates the direction perpendicular to the 10-O port flange surface). The angles are equal to the pitch angle (the angle between the magnetic axis and the sight line) of 100 degrees and 40 degrees, respectively.

The position (=angle) can be measured from the length of the stainless wire between the stage and a fixed point. The position data are sent to the Windows computer. At the same time, the timing data can be provided to the computer from the timer, which is triggered by the LHD discharge initiation.

3.Experimental Results

Two different experiments are performed to compare the behavior of the co-injection with the counter injection. The plasma initiated by ECH heating is sustained by NBI#1 (counter). Modulated NBI#2 (co) is added to the plasma. The TOF analyzer is set perpendicular against the plasma magnetic axis in order to investigate the comparison.

Figure 2. Intensity ratio of the particle flux between the co- and counter injection NBI.

Figure 2 shows the intensity ratio between the flux during NBI#1 (counter) and that during NBI#1+NBI#2 (modulated, co-injection). The neutral particle flux in the counter injection is less than that in co-injection even if the difference of number of the beam particle is considered. Background neutrals, which produce the high-energy neutral particles by the charge exchange reaction, are distributed near the plasma edge. The neutral particle flux in the counter injection is not much because the particle orbit in the counter injection is not located near the plasma edge. The particle confinement in the counter injection may be worse than that in co-injection. However the possibility cannot be verified only by this experiment. The pitch angle distribution of the high-energy neutral particle cannot be observed in the modulation experiment. The trapped particle instead of the transit particle can be mainly observed in the modulation

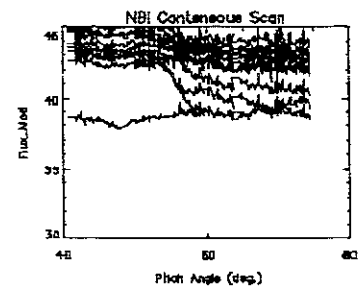Figure 3(a). The spatial-resolved neutral particle energy spectrum in NBI long discharge (co-injection).

Figure 3(b). The contour plot of Fig. 3(a).

experiment because the analyzer is set perpendicular to the magnetic axis.

To overtake the disadvantage, the pitch angle scan experiment during long discharge is performed. The accurate experimental result can be expected in the scanning on the long discharge rather than the scan shot-by-shot. The accurate comparison between the co- and counter injection can be expected so the horizontal scan of the an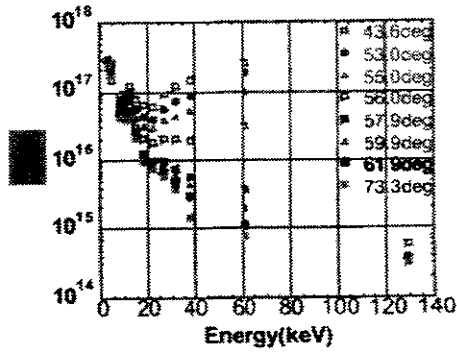alyzer during long discharge is also done in the inverse magnetic field. The spatial resolved energy spectra can be observed during a long discharge of NBI plasma by continuously scanning the neutral particle analyzer[3,4]. Figure 3(a) shows the time evaluated (=angular distributed) three-dimensional spectrum obtained by overlapping of three NBI plasma discharges. The pitch angle means the angle between the sight line and the central magnetic axis. In these discharges, the plasmas are initiated by the ECH heating, after that NBI#2
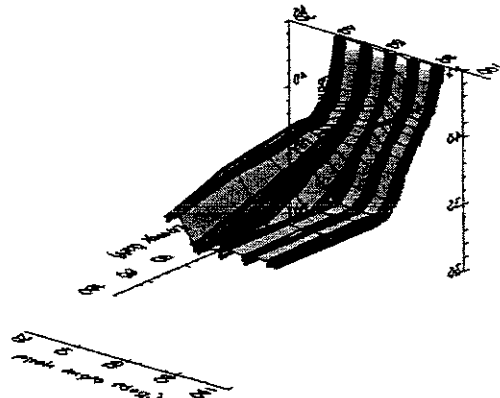

Figure 3(c). Energy spectrum of each pitch angle obtained by Fig. 3(a).

(co-injection) sustains the plasma during 40 – 60 seconds. The scanned pitch angle is from 44 degrees to 74 degrees. The electron density measured by the interferometer is kept to be almost 2×10^{19} cm^{-3} during discharge except the plasma initiation phase. At the initiation phase by ECH plasma, the high-energy particle flux is enhanced as the density is too low and the background neutral density is high. The injected hydrogen neutral beam energy of NBI#2 is only 130 keV because the original ion source polarity is negative. To make clear the pitch angle dependence, the contour plot of Fig.3 (a) is

Figure 4(a). The spatial-resolved neutral particle energy spectrum in NBI long discharge (counter-injection).

Figure 4(b). The contour plot of Fig. 4(a).

shown in Fig. 3(b). Figure 3(c) shows the spectra at some typical pitch angles. The shape of spectra is almost similar from 44 degrees to 53 degrees. However the spectra from 55 degrees are strongly varied. It reflects the injection pitch angle of the beam according to the simulation (53 degrees at Rax=3.75 m in simulation). The beam keeps the pitch angle at incidence until the beam energy becomes to the energy, which the pitch angle scattering is occurred by the

energy loss due to the electron collision. The low flux region can be observed around 10-15 keV, which is 15 times the electron temperature. The energy region may be equal to the energy at which the pitch angle scattering is occurred.

The pitch angle distribution and the contour plot are shown in Fig. 4(a) and Fig. 4(b), respectively when the magnetic field is inversely applied. The large variation at 48 degree can be observed. The pitch angle of the particle is almost conserved in high-energy region because the pitch angle scattering occurs near the energy of the 15 times of the electron temperature. It is not believed that only the particles with large pitch angle are localized near the plasma center where the back ground neutrals is not rich. Therefore it is reasonable that the particle with the pitch angle between 48 to 53 degree is lost. The neutral particle flux in the counter injection is less than that in the co-injection same as the modulation experiment. The main reason is that the guiding center of the particle orbit in the counter injection is shifted to the high field side. Another candidate of the flux decrease comes from the particle loss with large pitch angle. However the loss of the counter injected particle does not strongly affect to the heating efficiency and the stored energy because the contribution of the particle with large pitch angle is not so much.

4.Conclusion

The experiments for the comparison between the co- and counter neutral beam injection are performed. The pitch angle distribution of the neutral particle spectrum in the both injections can be precisely obtained by the scanning of the analyzer in long discharge by changing the magnetic field direction. In the counter injection the neutral particle flux is not so much because the particle orbit passes through the low background neutral region. It can be found that the particle with large pitch angle is lost in the counter injection from the spectrum of the pitch angle distribution of the neutral particle.

References

1. T. Watanabe, http://www.lhd.nifs.ac.jp/lhdorb.html
2. T. Ozaki, V. Zanza, G. Bracco, A. Moleti, B. Tilia, A. Sibio, S. Sudo, H. Nakanishi, M. Kojima, M. Shoji and G1/G2 experimental group, High Energy Neutral Particle Measurement System in Large Helical Device, *Rev. of Sci. Instrum.*, **71**(7), 2698-2703 (2000).
3. T. Ozaki, S. Sudo, et al., Preliminary Results of the Neutral Particle Measurements in Large Helical, *Plasma Phys. and* Fusion Research, SERIES, Vol.3, 444-448 (2000).
4. K. Saito, R. Kumazawa, T. Mutoh, T. Seki, T. Watari, T. Yamamoto, Y. Torii, N. Takeuchi, Y. Zhoa, A. Fukuyama, F. Shimpo, G. Nomura, M. Yokota, K. Kato, M.Sasao. M. Isobe, T. Ozaki, et al., A Study of high-energy ions produced by ICRF heating in LHD, *Plasma Physics and Controlled Fusion* **44** (2002) 103-119.

Equilibrium and Boundary Structure of Quasi-axisymmetric Stellarator CHS-qa

S. Okamura, A. Shimizu, C. Suzuki, M. Isobe, S. Nishimura, K. Matsuoka,
T. Hayashi, M. Yokoyama, N. Nakajima

National Institute for Fusion Science
Oroshi 322-6, Toki, 509-5292 Japan

1. Introduction

Physics design of an advanced stellarator CHS-qa has been in progress in the National Institute for Fusion Science (NIFS) as a candidate of a new generation of satellite experiment [1]. The design work is executed by the joint team of the experimental group of CHS (helio-tron/torsatron type device experiment) and the theory group in NIFS. Basic configuration was decided to be a compact stellarator with the quasi-axisymmetric (QAS) magnetic field structure [2]. The toroidal period number is two and the averaged aspect ratio is 3.2. The rotational transform is between 0.35 and 0.39 for the vacuum configuration avoiding the low order rational resonances. The basic engineering design is completed for the device parameters: major radius $R = 1.5$ m and the magnetic field strength $B_t = 1.5$ T.

The configuration optimization was made based on the fixed boundary solution of the three dimensional equilibrium solver, VMEC code [3]. Because this code calculates equilibrium with assumed existence of good magnetic surfaces, it is uncertain whether the magnetic surfaces are clearly formed without dangerous islands. Even the position of the last closed magnetic surface (LCMS) is not given from the code calculation. It is necessary to examine the magnetic surfaces with the field-line tracing for the vacuum field and the finite beta equilibrium calculated without the assumption of magnetic surfaces. The first step for such a study is designing of magnetic coils which can produce, in a good accuracy, the optimized fixed bound-ary equilibrium solution. With NESCOIL code [4], 20 modular coils were designed for full torus (four groups of five different shapes). For the vacuum field produced by these coils, the plasma equilibria were calculated with HINT code [5] which does not require the existence of magnetic surfaces.

2. Free boundary calculation without vertical field

The equilibrium calculation with HINT code is basically the free-boundary calculation since no restricting condition for the boundary is applied. We would like to compare HINT code results with free-boundary VMEC calculation. Figure 1 shows two equlibria for zero beta (left) and 1.5 % average beta (right) calculated with HINT code for 2b32 quasi-axisymmetric configuration of CHS-qa. It shows puncture plots of magnetic field-line tracing on the obtained equilibrium field. Since no vertical field is applied, the total plasma position is shifted outward for higher beta. In this calculation, the plasma current is assumed vanishing in the average for each magnetic surface. The position of the LCMS is a part of code calculation results. Because a considerable part of boundary region is lost for 1.5 % beta equilib-
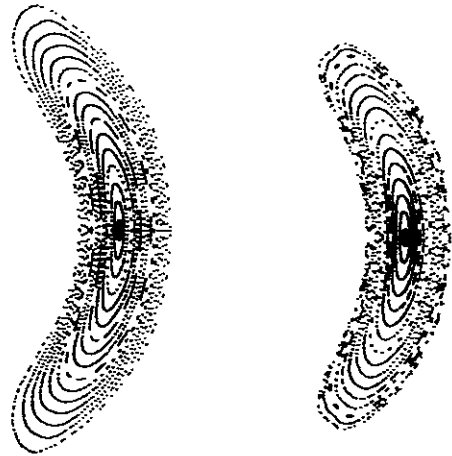
Fig. 1 Equilibria with HINT code

Fig. 2 Vacuum field-line tracing with MAGN code

rium, we would like to examine whether it is due to magnetic surface destruction for higher beta equilibrium.

In order to understand how the position of LCMS is determined in QAS configuration, vacuum magnetic surfaces are calculated for different surface position with the control of vertical field. It is known for the conventional stellarators (e.g., CHS and LHD), that there are two fixed points in the boundary region (inboard side and outboard side of LCMS) so that the magnetic surfaces can be formed only in the region between them. Figure 2 shows two vacuum field-line tracing results for 2b32 configuration: no vertical field (left) and 0.015 T vertical field for 1 T toroidal field (right). It is found
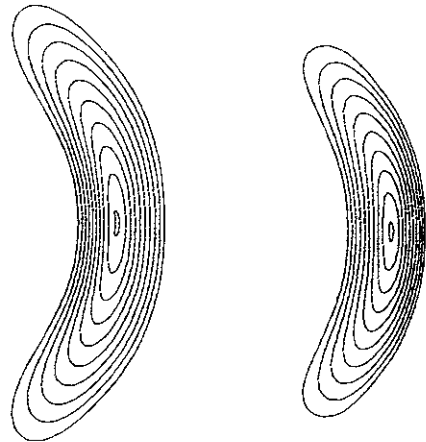
Fig. 3 Free-boundary VMEC calcu-lation

that the right edge of LCMS for two cases lie on the same position. This position is similar to the outboard fixed point for conventional stellarators described above. The vertical shift 0.015 T for the right plot is selected to make its boundary shape similar to the right plot in Fig. 1. Although the relative magnetic axis positions are slightly different for these two, the boundary shapes are very close. The loss of outer magnetic surfaces for 1.5 % equilibrium in Fig. 1 is simply due to the position shift effect which is observed in the vacuum configuration as well.

It is necessary to give the plasma volume for the free-boundary VMEC calculation. Figure 3 shows two results of VMEC run with the same volume as the original fixed boundary solution (left) and by keeping the width of the waist of LCMS the same as the right plot in Fig. 2. The resulting shapes of boundary are very close to the HINT results in Fig. 1. The iota
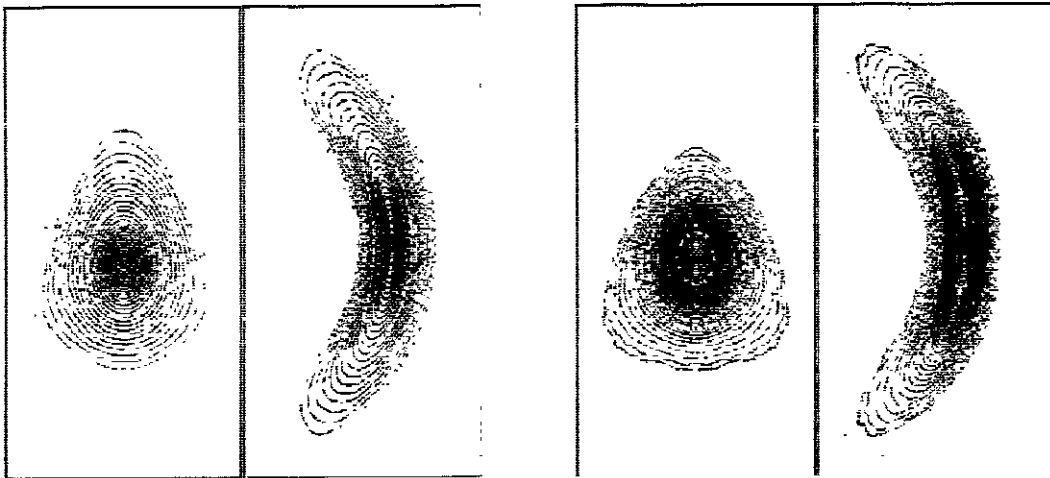
*Fig. 4. Puncture plots of magnetic surfaces for vacuum (left) and 3.3%
average beta (right) equilibria of CHS-qa calculated by HINT code.*

profiles obtained from HINT and VMEC are also very similar. For this level of beta, we confirmed the equilibria given by two codes are in a good agreement. However we found that the iota value in VMEC calculation for 2.4% beta is significantly lower than HINT result. A further study is necessary for the comparison of HINT and VMEC equilibrium calculation with free boundary condition.

3. High beta equilibrium calculated by HINT code

Because the loss of outer magnetic surfaces in Fig. 1 is caused by the outward shift of the surface position, an automatic control of vertical field is introduced in the HINT code calculation to push the position back recovering the lost magnetic surfaces. Figure 4 shows the equilibrium calculation with HINT code for vacuum and 3.3 % average beta. The left parts of two cases are for the horizontally elongated cross section with 90 degree rotation. The pressure profile is very sensitive to the robustness of the magnetic surfaces in the boundary region. In this calculation, the profile $p(\psi) \propto (1-\psi^2)$ is assumed. This profile is one of typical profiles observed in the existing helical experiments. More peaked pressure profiles give larger perturbation of the magnetic field for high beta equilibrium causing loss of boundary magnetic surfaces.

Plasma current was assumed zero in average on each magnetic surface. It is expected that comparable order of bootstrap current as tokamaks will be created in high beta plasma in QAS stellarators. The estimated value reached to 100 kA for high beta discharges in CHS-qa. HINT code calculations including the plasma current with self-consistent profile to the pressure profile has not yet been made.

4. Divertor field-line tracing for vacuum configuration

The divertor magnetic field structure design is one of most important key issues of magnetic confinement research for fusion. Since the optimization of QAS stellarator is mostly
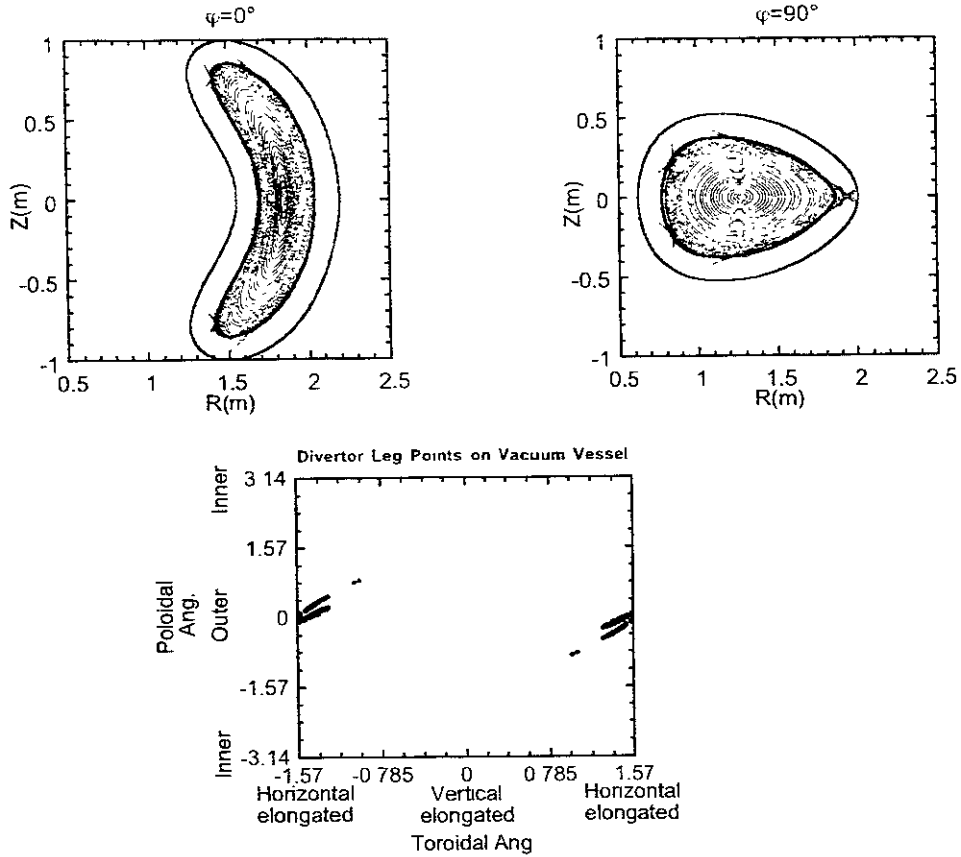
Fig. 5   Divertor field line tracing for 2b32 configuration. Intersecting points on the wall are plotted on toroidal and poloidal angles

done for the magnetic surface quantities, this important problem is left over in the QAS configuration discussion. Although lots of people recognize this issue important, it is not yet included into the list of figure of merits in the optimization loop.

Several modular coil design can be made for the same optimized configuration depending on the design conditions of the coils. We found that two sets of modular coil design give very different divertor trace structures. Since they are both designed to satisfy the given magnetic surface quantities for QAS configuration, the magnetic surfaces inside LCMS are very similar for both cases. However one set of modular coils gives clearer island divertor structure shown in Fig. 5 while another does not. It suggests that if the quality of the divertor field structure could be evaluated as a figure of merit, much better coil design would be possible satisfying both good magnetic surface quantities and good divertor structure.

REFERENCES

[1] K. Matsuoka et al., Plasma Phys. Rep. 23, 542 (1997).

[2] S. Okamura et al., Nucl. Fusion 41, 1865 (2001).

[3] S. P. Hirshman et al., Comput. Phys. Commun. 43, 143 (1986).

[4] P. Merkel, Nucl. Fusion 27, 867 (1987).

[5] T. Hayashi et al., Theory of Fusion Plasmas, p.11 (Varenna, 1988).

Theoretical Study of Structure and Dynamics
of Radial Electric Field in Helical Plasmas

S. Toda and K. Itoh

National Institute for Fusion Science, Toki-shi, Gifu, 509-5292, Japan

1. Introduction

The internal transport barrier has been found in the ECRH plasma in the compact helical system (CHS) and the steep gradient in the profile of the radial electric field is obtained in the inner region [1]. A pulsating behavior of electrostatic potential is also found in CHS heliotron/torsatron [2]. We have examined the one-dimensional transport equations which describe the temporal evolutions of the density, the electron and ion temperatures, and the radial electric field in a cylindrical heliotron configuration [3]. The anomalous transport model for anomalous diffusivities to describe the plasma like L-mode has been used. The stationary structure of the radial electric field with hysteresis characteristic (hard transition) was examined in helical plasmas. The strong reduction of the anomalous transport can be obtained near the transition point. However, in the parameter region examined in a previous study, the anomalous transport is dominant compared with the neoclassical transport because the reduction of the anomalous transport can not be obtained at the radial points which are not near the transition point. Therefore, the reduction of the neoclassical transport due to the large positive E_r is not seen and there is not a clear suppression in the total transport.

To show the clear transport barrier in an analytic result, the dependence of the stationary profile of plasma quantities on the input power profile is mainly studied. The hard transition which is characterized by the rapid change spatially is examined. The clear transport barrier can be obtained theoretically because of the large positive value of E_r. When the different external control parameter from the previous analysis is adapted, the neoclassical transport is found to be dominant compared with the anomalous transport in the wide inner region since the gradient of the radial electric field is enough strong to reduce the anomalous transport. Furthermore, we study the dynamics of the radial electric field.

2. One-dimensional model transport equations

In this section, model equations used in this study are explained. The cylindrical coordinate is used and r-axis is taken in the radial cylindrical plasma. The total particle flux Γ^t is set as $\Gamma^t=\Gamma^{na}-D_a\partial n/\partial r$ in this article, where D_a is the anomalous particle diffusivity and Γ^{na} is the radial neoclassical flux associated with helical-rippled trapped particle. The expression for the neoclassical flux here is the connection formula and is applicable from the ν_{thj} regime defined by $D_j \propto \nu_{thj}$ to the $1/\nu_{thj}$ regime $(D_j \propto 1/\nu_{thj})$, where D_j is the particle diffusion coefficient and ν_{thj} is the collision frequency estimated by the thermal velocity for species j [4]. The total heat flux Q_j^t of the species j is expressed as $Q_j^t=Q_j^{na}-n\chi_a\partial T_j/\partial r$, where χ_a is the anomalous heat diffusivity and Q_j^{na} is the energy flux by the neoclassical ripple transport, respectively. The theoretical model for the anomalous heat conductivity will be explained later. The formula for Q_j^{na} are also given in ref. [4]. The anomalous diffusion coefficient for E_r is denoted by D_{Ea} and is given in ref. [5]. The temporal equation for the density is

$$\frac{\partial n}{\partial t}=-\frac{1}{r}\frac{\partial}{\partial r}(r\Gamma^t)+S_n. \tag{1}$$

The term S_n represents the particle source. The equation for the electron temperature is given as

$$\frac{3}{2}\frac{\partial}{\partial t}(nT_e)=-\frac{1}{r}\frac{\partial}{\partial r}(rQ_e^t)-\frac{m_e}{m_i}\frac{n}{\tau_e}(T_e-T_i)+P_{he}, \tag{2}$$

where the τ_e denotes the electron collision time and the second term on the right-hand side represents the heat exchange between electrons and ions. The term P_{he} represents the absorbed power due to the ECRH heating and its profile is assumed to be proportional to

$\exp(-(r/(0.1a))^2)$ for simplicity. This profile has more central peaking than the previous analysis [3]. The equation for the ion temperature is

$$\frac{3}{2}\frac{\partial}{\partial t}(nT_i)=-\frac{1}{r}\frac{\partial}{\partial r}(rQ_i)+\frac{m_e}{m_i}\frac{n}{\tau_e}(T_e-T_i).$$ (3)

The term P_{hi} represents the absorbed power of ions and its profile is also assumed to be proportional to $\exp(-(r/(0.1a))^2)$. The temporal equation for the radial electric field in a helical is expressed by [5]

$$\frac{\partial E_r}{\partial t}=-\frac{e}{\varepsilon_\perp}\sum_j Z_j\Gamma_j^{na}+\frac{1}{r}\frac{\partial}{\partial r}(\sum_j Z_j e(D_{Ej}+D_{Ea})r\frac{\partial E_r}{\partial r}),$$ (4)

where $\varepsilon_\perp$ is the perpendicular dielectric coefficient calculated as $\varepsilon_\perp=\varepsilon_0((c^2/v_A^2)+1)(1+2q^2)$. The factor $(1+2q^2)$ is introduced due to the toroidal effect.

3. Boundary conditions and model for anomalous transport coefficients

The density, temperature and electric field equations (1)-(4) are solved under the appropriate boundary conditions. We fix the boundary condition at the center of the plasma (r=0) such that $n'=T_e'=T_i'=E_r=0$, where the prime denotes the radial derivative. For equation (4), the boundary condition at the edge (r=a) is the ambipolar condition. This simplification is employed because the electric field bifurcation in the core plasma is the main subject of this study. The boundary conditions at the edge (r=a) for the density and the temperatures are those in CHS device: $-n/n'=0.05m$, $-T_e/T_e'=-T_i/T_i'=0.02m$. The machine parameters are similar to those of CHS device, such as R=1m, a=0.2m, the toroidal magnetic field B=1T, toroidal mode number m=8 and the poloidal mode number l=2. We set the safety factor and the helical ripple coefficient as $q=3.3-3.8(r/a)^2+1.5(r/a)^4$ and $\varepsilon_h=0.231(r/a)^2+0.00231(r/a)^4$, respectively [1]. The particle source S_n is set to be $S_n=S_0\exp((r-a)/L_0)$, where L_0 is set to be 0.01m and the value of S_0 controls the average density by the particle confinement time. This profile corresponds to the peaking at the plasma edge of the particle source due to the ionization effect. The values for the anomalous diffusivity of the particle and the anomalous coefficient for E_r are chosen $D_a=1m^2s^{-1}$ and $D_{Ea}=1m^2s^{-1}$. These values are set to be constant spatially and temporally. In this study, we adopt the model for the anomalous heat conductivity based on the theory of the self-sustained turbulence due to the interchange mode, driven by the current difffusivity [6]. This model is chosen because the experiment in CHS device is done in the configuration of the magnetic hill. The anomalous transport coefficient for the temperatures is given as $\chi_a=\chi_0/(1+G\omega_{Ei}^2)$, where χ_0 and G are the functions of the magnetic shear, the safety factor, the pressure gradient and so on. The details of the forms χ_0 and G are shown in ref. [6]. The parameter ω_{Ei} represents the effect of the suppression due to the electric field gradient. In order to set the averaged temperature of electrons T_e to be around $\overline{T_e}=610eV$ and the density to be around $\bar{n}=2\times10^{19}m^{-3}$, the absorbed power of electrons is 100kW and the coefficient of the source term S_0 is $1.5\times10^{24}m^{-3}s^{-1}$ for the choice of above values of anomalous transport coefficients. The averaged ion temperature is chosen to be about $\overline{T_i}=430eV$, where the absorbed power of ions is fixed at 50kW.

4. Stationary solution with multiple ambipolar electric fields

Using these parameters and boundary conditions given, we analysis the equations (1)-(4). The stationary solutions of the radial electric field are shown in figure 1(a). The profiles of the density and the temperature are shown in figures 1(b) and (c), respectively. In figure 1(c), the dotted line represents T_i and the solid line shows T_e. In figure 1(a), the transition of the radial electric field is found at the point $\rho=\rho_T$ (0.49), where ρ represents the normalized minor radius r/a. The circles in figure 1(a) show the values of the electric field which satisfy the local ambipolar condition for the calculated profiles of the density and the temperatures of figure

1(b) and (c). Multiple solutions are found to exist for the local ambipolar condition in the parameter region examined here. In the case of figure 1(a), the electron root ($\rho<\rho_T$) for E_r is sharply connected to the ion root ($\rho>\rho_T$) with a thin layer between them. The transition point should be determined by the Maxwell construction [7]. We confirm that the Maxwell construction is satisfied. The derivative of the radial electric field is observed in figure 1(d). The peak at the transition point $\rho=\rho_T$ is found in figure 1(d). Furthermore, due to the central heating, the gradient of the radial electric field is obtained to some extent in the region $\rho<\rho_T$.

The transport barrier can be shown in both T_e and T_i profiles in figure 1(c). The value of the anomalous diffusivity shown in figure 2(a) is that of χ_a. At the transition point $\rho=\rho_T$, the suppression is obtained due to the strong gradient of the electric field. The neoclassical diffusivities of electrons χ_e^{NEO} and ions χ_i^{NEO} are also shown with the solid line and the dashed line, respectively. Because of the large positive value of E_r, the reduction of the neoclassical transport is obtained in the region $\rho<\rho_1$. In the wide inner region $\rho<\rho_1$, the anomalous transport is moderately reduced due to the E_r gradient. In figure 2(a), the anomalous transport is suppressed up to about one third in the region $\rho<\rho_T$ compared with the case of no E_r
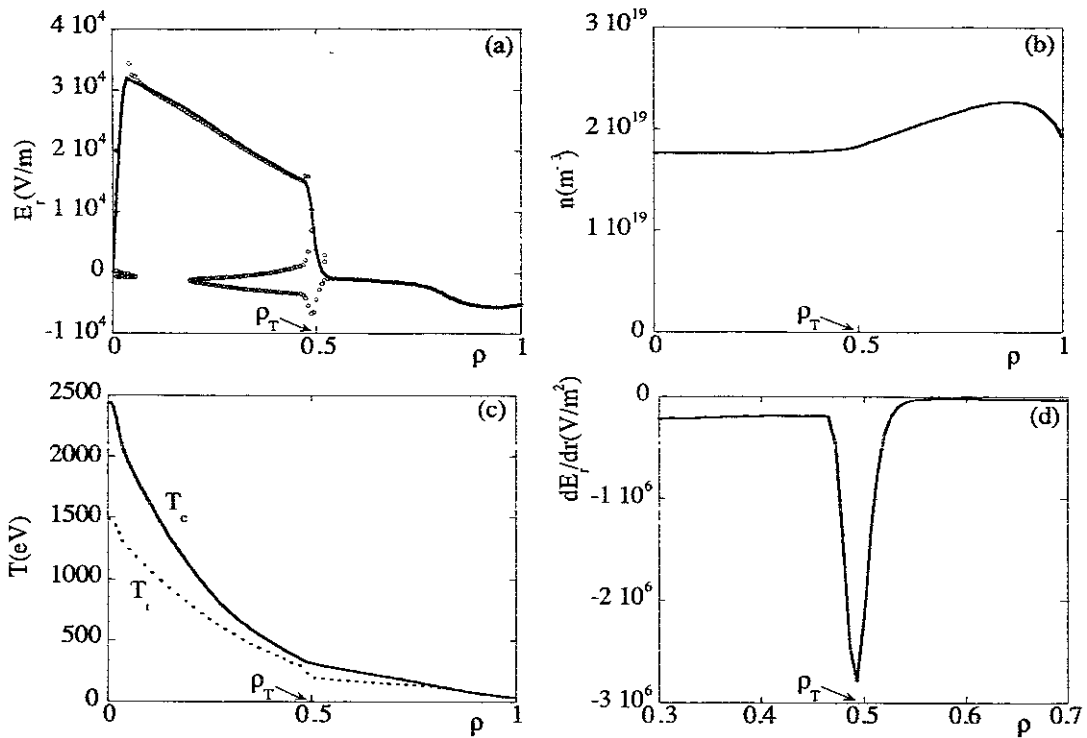
Figure 1 Radial profiles of (a) the electric field, (b) the density, (c) the electron temperature (solid line) and the ion temperature (dotted line) and (d) the derivative of the electric field.
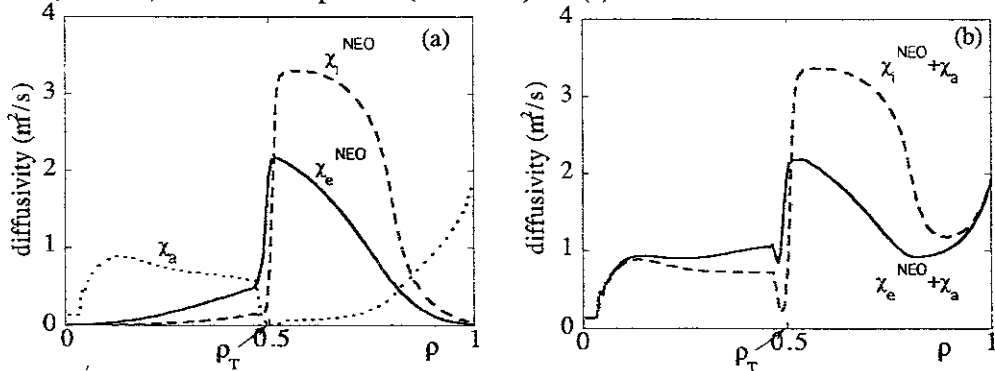
Figure 2 Radial dependence of the diffusivities. In the core region, the improvement is found because of the large positive E_r.

gradient. In the region $\rho > \rho_T$, the neoclassical transport is found to be dominant compared with the anomalous transport in the parameter region examined here. In figure 2(b), the sum of the anomalous and neoclassical diffusivities in the case of electrons and ions is obtained with the solid line and the dashed line, respectively. In the electron channel, the total heat conductivity in the region $\rho < \rho_T$ is about one half of that in the $\rho > \rho_T$ region. In the ion channel, the total heat conductivity in the region $\rho < \rho_T$ is around one third of that in the region $\rho > \rho_T$. Therefore, the clear transport barrier is obtained in both profiles of ion and electron temperatures.

5. Dynamics of radial electric field

In this section, the dynamics of the electric field is examined in the analysis shown in the previous section. In figure 3, the profiles of the electric field are shown at three times. The profile of E_r (solid line) at t=0.2s corresponds to the stationary one, which is identical to that in figure 1(a). Before the state reaches the stationary one, the dotted line and the dashed line show the profiles of E_r at 0.005s and 0.02s, respectively. When the state approaches to the stationary one, the transition point ρ_T goes inside and the gradient of E_r gets steeper in the case of the initial condition chosen here. The time during which the state reaches the stationary one is about a few times as long as the typical energy confinement time $\tau_E \sim 0.01s$. In this study in which a theoretical model due to the current diffusivity is used, the oscillating solution in time is not obtained in the parameter region examined in this paper.
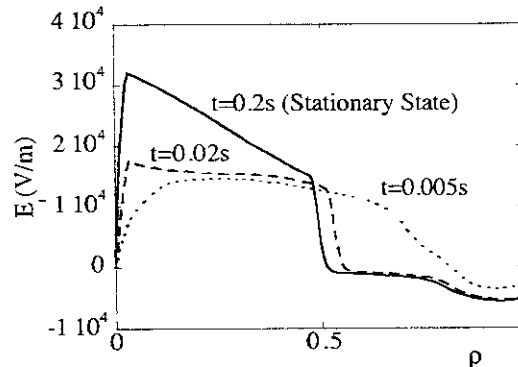
Figure. 3 The temporal evolution of E_r profile is shown. The dotted line represents the E_r profile at t=0.005s, the dashed line represents the one at t=0.02s and the solid line shows the E_r profile at t=0.2s, respectively.

6. Summary and discussion

In this paper, the structure of the radial electric field in helical plasmas is theoretically studied in the case of the more central heating profile than the previous analysis. The parameter region in which the neoclassical transport is dominant compared with the anomalous transport is found by use of a theoretical model for the anomalous transport diffusivities. The clear transport barrier is seen in the profiles of the temperatures. Therefore, it is shown that the heating profile is important when the bifurcation characteristic exists even if the values of the heating power are same. In this study, only a theoretical model for anomalous coefficients due to the interchange mode is used. Analyses by use of other theoretical models (e.g., Ion temperature gradient mode) for anomalous coefficients are needed. The continuous study of the dynamics of the electric field should be done to study the electric pulsation observed in CHS device. These are future studies.

References

[1] A. Fujisawa et al., Phys. Plasmas 7 4152 (2000).
[2] A. Fujisawa et al., Phys. Rev. Lett. 81 2256 (1998).
[3] S. Toda and K. Itoh, Plasma Phys. Control. Fusion 44 325 (2002).
[4] K. C. Shaing, Phys. Fluids 27 1567 (1984).
[5] D. E. Hastings, Phys. Fluids 28 334 (1985).
[6] K. Itoh et al., Plasma Phys. Control. Fusion 36 123 (1994).
[7] K. Itoh, S. -I. Itoh and A. Fukuyama, Transport and Structural Formation in Plasmas (London, UK: Institute of Physics Publishing) ch 12.

PROSPECT OF STRONGLY INWARD SHIFTED CONFIGURATION IN CHS

K. Matsuoka, S. Okamura, A. Shimizu, C. Suzuki, S. Nishimura, M. Isobe, A. Fujisawa,
T. Minami, Y. Yoshimura, I. Nomura, C. Takahashi, K. Ida, Y. Liang, H. Iguchi, K. Toi
and
M. Yoshinuma

National Institute for Fusion Science, Toki 509-5292, Japan

Abstract

Inward shifts of the vacuum magnetic axis position R_{ax} in CHS have shown compatibility between good particle orbit and MHD stability, and the configuration with R_{ax} of 92 cm has been adopted as the standard configuration. The internal transport barrier (ITB) on the electron energy was realized in the standard configuration. Recently both of ion energy transport and particle diffusion of impurity ion were found to be improved under the ITB formation. The MHD stability has been studied in strongly inward shifted R_{ax} configurations including the $\sigma=1$ configuration where R_{ax} is about 88cm, because the neoclassical transport is expected to be more improved. It is found that NBI plasmas with $<\beta>$ of about 1 % have not shown any confinement degradation irrespective of expected ideal interchange instabilities because of the stronger magnetic hill. Strongly inward shifted R_{ax} configurations have good prospect from the viewpoint of MHD stability and confinement improvement.

1. Introduction

Helical magnetic traps must satisfy the following requirements: 1) clean and robust magnetic surfaces with an external rotational transform, 2) good α-particle orbit and good neoclassical transport, 3) high equilibrium- and stability-β values, 4) good energy confinement, 5) adequate capability of heat and particle control. After confirming the vacuum magnetic surface of CHS having the aspect ratio of 5 ($R / a_p = 1m / 0.2m$), the prospect of CHS heliotron/torsatron configuration was discussed on the above requirements [1] : 2) successful plasma discharge without radiation collapse only with ICRF heating, 3) high β stability up to 2%, and 4) global τ_E scaling. The most important point was that the inward shifted configurations with R_{ax} of 92cm showed the compatibility between good particle orbit and MHD stability [2, 3].

Since that time the confinement improvement has been the most important subject in CHS experiments. Improved modes of tokamaks are usually accompanied with a negative radial electric field E_r, where there is a positive feedback relation between the negative E_r and the ion pressure gradient. In CHS, trials for confinement improvement following tokamaks have been made. The H-mode was obtained by controlling the edge rotational transform (adjusted to be nearly 1 just inside LCFS) through inducing the OH current in an NB heated plasma [4]. Here, the simultaneous increase in the line averaged electron density n_e and the decrease in the $H\alpha$ signal were observed in spite of a constant gas puffing, which is usually seen in H-modes of tokamaks. However, the jump in the poloidal rotation velocity was not observed in CHS

and the improvement factor is up to 15%. High ion temperature (T_i) mode in an NB plasma was realized by making the electron density peaked [5]. Here, the density was fuelled primarily with NB without gas puffing under intensive titanium gettering. The ion thermal diffusivity χ_i in high T_i mode is lowered by factor of two than that in the L-mode, reflecting the steeper T_i profile. Again, the improvement factor is not large, although the maximum T_i of 1 keV was attained in the high T_i mode of CHS.

Another concern has been MHD stability in strongly inward shifted configurations (R_{ax} < 90cm) where the neoclassical transport is improved. Although the σ=1 configuration, where R_{ax} is 88cm, was studied from the viewpoint of the neoclassical transport in the low-collisionality ECH plasma with low β [6], MHD stability study of finite-β plasma in the σ=1 configuration has not been done. As R_{ax} is shifted inward the magnetic hill gets stronger, that is because the outermost flux surface is almost fixed being determined by the helical coils whereas R_{ax} can be changed freely by controlling poloidal coil currents.

2. Internal Transport Barrier in CHS

The confinement improvement is closely related to E_r and its shear. The E_r in CHS is determined by the ambipolar condition between electron and ion fluxes caused by non-ambipolar diffusion, bulk viscosity, orbit loss, charge exchange loss and so on. In CHS the non-ambipolar diffusion is the dominant process. The neoclassical internal transport barrier (NITB) for the electron energy was realized, for the first time in helical machines, by applying the 2nd harmonic heating of ECH with the frequency of 53.2 GHz and the threshold power of about 200 kW when R_{ax} and B_t were 92.1 cm and 0.88 T, respectively [7, 8]. It was induced by the large positive E_r shear that is due to the bifurcated electric potential inside the barrier. In a conventional helical machine like CHS, where large rotation shear can not be expected because of a large helical ripple, the E_r shear should rely on the non-ambipolar radial diffusion of ions and electrons. It has been shown that χ_e gets close to the neoclassical value in the barrier region [9]. The bifurcation occurs more easily as the electron density decreases under the heating power kept constant or as the power increases under the constant electron density. The electron density n_e of the ECH plasma with NITB is below about 3×10^{12} cm^{-3}, and the central electron temperature T_e (0) is in the range of a few keV. To increase n_e where NITB is realized two methods were tried. Higher frequency of 106 GHz at the 2nd harmonic ECH results in NITB with higher n_e of about 5×10^{12} cm^{-3}. The hysteresis phenomena have been clarified between the central potential and n_e when those parameters are plotted along the temporal evolution of the discharge. Once NITB is established it can be kept at higher n_e. This hysteresis could also be used as a promising scenario to obtain the high confinement at higher electron density.

Since the discovery of NITB for the electron energy in ECH plasma the next concern has been on the improvement in the ion thermal diffusivity and in the particle diffusion. The 53 GHz 2nd harmonic ECH with the power of 130kW is applied to low-n_e NB plasmas with the central density n_e (0) of 3-4×10^{12}cm^{-3}, because the heating source for ions is needed within the barrier. The plasma makes transition to the electron root and T_e (0) increases to about 2 keV, and it

lowers to a few 100 eV after the ECH pulse. The NITB is formed in the NB plasma with ECH; the electron pressure increases by about factor of 4 in spite of the reduced n_e because of ECH. The ion temperature T_i also increases by about 50 %, however the ion pressure decreases due to the reduced electron density. The substantial part of the increase in T_i is attributed to the increased T_e. On the other hand, when the ECH power is injected to slightly-higher-n_e NB plasma with $n_e(0)$ of $4\text{-}5 \times 10^{12} \text{cm}^{-3}$, $T_e(0)$ increases by factor of 4-5 to 900eV, however there is almost no increase in T_i. The transport analyses on the lower-n_e case show that the electron thermal diffusivity is much reduced and is almost on the same level of the neoclassical value, and the ion thermal diffusivity is reduced inside of NITB.

The particle transport of titanium impurity ion is studied with soft X-ray CCD camera. The photon counting mode provides us with the 2 dimensional spatial profiles of the peak energy of Ti $K\alpha$ line that is determined by T_e and the diffusivity [10]. It has been found by using the MIST code that the diffusivity is of the order of 0.02 m^2/s inside of NITB being much smaller than the value of 0.1- 0.2 m^2/s without NITB.

3. MHD Stability in the Strongly Inward Shifted Configuration

Two NBs were switched from balanced-injection to co- (or ctr-) injection and IBW with 9MHz has been operational to produce the target plasma irrespective of the magnetic field strength B_t. Two co-injected NBs resulted in $T_e(0)$ of 7-800eV at n_e of $4\text{-}5 \times 10^{13} \text{cm}^{-3}$, in the configuration with R_{ax} of 92.1cm and B_t of 1.76T, of which plasma parameters had not been obtained in the balanced injection. By using two NBs the MHD study on strongly inward shifted configurations has been done. The average value $<\beta>$ of 1.2 - 1.3 % has been obtained without an elaborate wall conditioning at B_t of 0.75 T with R_{ax} of 89.9cm. The plasma passes through the range of $<\beta>$ where the interchange mode is well unstable from the Mercier criterion. However, MHD instabilities that degrade the confinement have not been observed. In the previous experiment MHD instabilities which reduced the stored energy were excited for R_{ax} of 89.9cm at $<\beta>$ of 0.8 % after a sudden increase in the stored energy and in soft X-ray signals without changing externally controllable parameters. The reason why the previous result is not reproducible has not been known. Even if R_{ax} is shifted more inward to 88.8cm, that is the $\sigma=1$ configuration in CHS, the confinement of the plasma with $<\beta>$ up to 0.8 % is not degraded, where the magnetic hill gets stronger. The same thing holds for the plasma with $<\beta>$ up to 0.6 % with the further inward shift of R_{ax} to 87.8cm. The decrease in the achieved $<\beta>$ is primarily due to the decrease in the plasma volume as R_{ax} is shifted inward. Mode analyses for the plasma with R_{ax} of 89.9cm show that coherent m=2 modes rotating in the ion diamagnetic direction appear at $<\beta>$ of about 1% where the position of iota of 0.5 is located near D_i of about 0.2. Burst-type oscillations are observed at lower $<\beta>$ as before. Because of the technical limitation that the IBW antenna can not reach the outermost magnetic surface of the strongly inward shifted configurations (R_{ax} of 88.8cm or more inward) for the initial breakdown, the plasma produced at R_{ax} of 89.9cm with low B_t that is not available for 53GHz ECH was shifted dynamically inward to R_{ax} of 88.2cm by controlling the poloidal field coil currents in 100 msec. During this phase the poloidal flux and the quadrupole component were

kept constant not to induce OH current and not to introduce an additional effect of plasma shape of elongation on confinement. It is shown that T_e and n_e are increased by the dynamic shift in spite of the reduced plasma volume. The reason of the increase has not been known yet, however it can be said at least that there is no confinement degradation.

4. Summary and Discussion

The NITB in the standard configuration with R_{ax} of 92.1cm has shown the improvement not only in electron energy but also in ion energy and in particle diffusion for the low n_e NBI plasma. Although the potential bifurcation phenomena including NITB have been studied in the standard configuration with HIBP, the NITB should be realized also for strongly inward shifted configurations because it is caused by the nonambipolar fluxes originating in CHS magnetic field structures. The NITB should be more prominent in strongly inward shifted configurations where the neoclassical transport is more suppressed [11]. The NITB mode is a promising candidate for improved confinement that is expected in helical systems having no symmetry in their magnetic field strength. The hysteresis inherent in bifurcation can be used to obtain improved plasmas with higher n_e. Compatibility between good particle trajectory and MHD stability holds for strongly inward shifted configurations, including the $\sigma=1$ configuration, of CHS with the low aspect ratio. From the physics point of view the strongly inward shifted configuration has a good prospect in the CHS future experiment.

References
[1] K. Matsuoka et al., 22nd EPS conference, Bournemouth (1995).
[2] K. Matsuoka et al., Fusion Eng. Design, 26 (1995) 135.
[3] S. Okamura et al., Nucl. Fusion, 35 (1995) 283.
[4] K. Toi et al., Plasma Phys. Control. Fusion, 38 (1996) 1289.
[5] K. Ida et al., Nucl.Fusion, 39 (1999) 1649.
[6] S. Okamura et al., Nucl. Fusion 39 (1999) 1337.
[7] A. Fujisawa et al., Phys. Rev. Lett., 82 (1999) 2669.
[8] A. Fujisawa et al., Plasma Phys. Control. Fusion, 41 (1999) A561.
[9] T. Minami et al., Plasma Phys. Control. Fusion, 44 (2002) A197.
[10] Y. Liang et al., to be published in Plasma Phys. Control. Fusion.
[11] M.F.Heyn et al., Plasma Phys. Control. Fusion, 43 (2001) 1311.

Kinetic and Fluid Simulations of the Collisionless Slab Ion Temperature Gradient Driven Turbulence

H. Sugama and T.-H. Watanabe

National Institute for Fusion Science / Graduate University for Advanced Studies
Toki 509-5292, Japan

W. Horton

Institute for Fusion Studies, The University of Texas at Austin
Austin, Texas 78712, USA

1. INTRODUCTION

In recent years, gyrokinetic and gyrofluid (or gyro-Landau-fluid) simulations [1] of plasma turbulence driven by microinstabilities such as the ion temperature gradient (ITG) mode [2] have been actively done in order to predict the anomalous transport coefficients in magnetically confined plasmas from the first principle. In the gyrofluid model, some closure relations are assumed to construct a truncated system of fluid equations from the gyrokinetic equation and their validity in nonlinear or turbulent regimes is not clear because conventional gyrofluid closure models such as the Hammett-Perkins (H-P) model [3] are originally derived so as to accurately reproduce gyrokinetic dispersion relations for linear modes. In fact, there exist some cases, in which the gyrokinetic and gyrofluid simulations show disagreements in their nonlinear results such as the saturated fluctuation levels and the turbulent transport coefficients.

In our previous work [4], we have presented the nondissipative closure model (NCM), which takes into account the time reversal symmetry of the collisionless kinetic equation. The NCM relates the parallel heat flux to the temperature and the parallel flow in terms of the real-valued coefficients in the unstable wave number space. The NCM was derived such that the closure relation is valid both for the unstable normal-mode solution and its complex-conjugate solution as well as for any linear combination of these solutions. A fluid system of equations with the NCM used reproduce the exact nonlinear kinetic solution of the three-mode ITG problem [5] while the H-P model fails in representing that solution. Then, the next question is whether the NCM can successfully describe strongly turbulent states of collisionless kinetic systems with a higher number of degrees of freedom. In the present work, in order to answer this question, we do both fluid and kinetic simulations of the two-dimensional slab ITG turbulence and investigate how accurately the fluid simulation using the NCM or the H-P model can reproduce results of the collisionless kinetic simulation under the same conditions.

2. BASIC EQUATIONS

The collisionless electrostatic gyrokinetic equation for ions in the uniform magnetic field B is written in the wave number (k) space as

$$\partial_t f_{\mathbf{k}} + i k_{\parallel} v_{\parallel} f_{\mathbf{k}} - \frac{c}{B} \sum_{\mathbf{k}'+\mathbf{k}''=\mathbf{k}} [\mathbf{b} \cdot (\mathbf{k}' \times \mathbf{k}'')] \Psi_{\mathbf{k}'} f_{\mathbf{k}''}$$

$$= i \left[\omega_{*i} \left\{ 1 + \eta_i \left(\frac{m_i v_{\parallel}^2}{2 T_i} - \frac{1}{2} \right) \right\} - k_{\parallel} v_{\parallel} \right] F_M \frac{e \Psi_{\mathbf{k}}}{T_i}, \tag{1}$$

where $F_M - n_0(m_i/2\pi T_i)^{1/2}\exp(-m_i v_\parallel^2/2T_i)$ is a background Maxwellian part of the ion distribution function, $f_k = f_k(v_\parallel,t)$ is a perturbation part integrated over the $\mathbf{v}_\perp$-space with the Maxwellian $\mathbf{v}_\perp$-dependence $\propto \exp(-m_i v_\perp^2/2T_i)$ assumed, and $\Psi_k \equiv \phi_k \exp(-b_k/2)$ $[b_k \equiv k_\perp^2 T_i/(m_i\Omega_i^2)]$. Here, inhomogeneities in the background density n_0 and temperature T_0 are taken into account only through $\omega_* \equiv (cT_i/eB)\mathbf{k}\cdot \mathbf{b}\times\nabla\ln n_0$ and $\eta_i \equiv d\ln T_i/d\ln n_0$ while n_0 and T_i in other places as well as ω_* and η_i are regarded as constants.

Taking the velocity moments of Eq. (1), we obtain fluid equations,

$$\partial_t n_k + ik_\parallel n_0 u_k - i\omega_* n_0\left(1 - \frac{b_k}{2}\eta_i\right)\frac{e\Psi_k}{T_i} - \frac{c}{B}\sum_{k'+k''=k}[\mathbf{b}\cdot(\mathbf{k}'\times\mathbf{k}'')]\Psi_{k'}n_{k''} = 0, \quad (2)$$

$$n_0 m_i \partial_t u_k + ik_\parallel(T_i n_k + n_0 T_k + n_0 e\Psi_k) - \frac{n_0 m_i c}{B}\sum_{k'+k''=k}[\mathbf{b}\cdot(\mathbf{k}'\times\mathbf{k}'')]\Psi_{k'}u_{k''} = 0, \quad (3)$$

$$n_0\partial_t T_k + ik_\parallel(2n_0 T_i u_k + q_k) - i\omega_* \eta_i n_0 e\Psi_k - \frac{n_0 c}{B}\sum_{k'+k''=k}[\mathbf{b}\cdot(\mathbf{k}'\times\mathbf{k}'')]\Psi_{k'}T_{k''} = 0, \quad (4)$$

where $n_k(t) \equiv \int_{-\infty}^{\infty}dv_\parallel f_k(v_\parallel,t)$, $n_0 u_k(t) \equiv \int_{-\infty}^{\infty}dv_\parallel f_k(v_\parallel,t)v_\parallel$, $n_0 T_k(t) \equiv \int_{-\infty}^{\infty}dv_\parallel$ $\times f_k(v_\parallel,t)(m_i v_\parallel^2 - T_i)$, and $q_k(t) \equiv \int_{-\infty}^{\infty}dv_\parallel f_k(v_\parallel,t)(m_i v_\parallel^3 - 3T_i v_\parallel)$.

Assuming the adiabatic electron response and using the quasineutrality condition give

$$\exp(-b_k/2)n_k - n_0\frac{e\phi_k}{T_i}[1 - \Gamma_0(b_k)] = \frac{e\phi_k}{T_c} \qquad (\text{for } k_\parallel \neq 0), \quad (5)$$

where Γ_0 is defined by $\Gamma_0(b_k) \equiv I_0(b_k)\exp(-b_k)$ with the 0-th-order modified Bessel function I_0. For the fluctuations with $k_\parallel = 0$, the electron density perturbation is often assumed to vanish and then the quasineutrality condition gives $\exp(-b_k/2)n_k - n_0(e\phi_k/T_i)[1 - \Gamma_0(b_k)] = 0$. When using this condition for $k_\parallel = 0$ with Eqs. (1) and (5) for the two-dimensional slab ITG turbulence simulation, we have found that a large zonal flow component, ϕ_k with $k_\parallel = 0$, is nonlinearly generated, suppresses linearly-unstable modes with $k_\parallel \neq 0$, and results in no turbulent transport [6]. Thus, efficiency of zonal flow generation and resultant transport coefficients are strongly influenced by what condition is used for the $k_\parallel = 0$ modes. In more practical cases of toroidal configurations, the zonal flow would be significantly reduced by the collisionless transit time magnetic pumping and by the collisional damping [7] although neither of these effects is included in Eq. (1). Here, in order to avoid the complexity brought about by the zonal flow and get finite turbulent transport, we put

$$f_k = \phi_k = 0 \qquad (\text{for } k_\parallel = 0), \quad (6)$$

and

$$n_k = u_k = T_k = \phi_k = 0 \qquad (\text{for } k_\parallel = 0), \quad (7)$$

in our kinetic and fluid simulations, respectively.

Now, a closed nonlinear kinetic system of equations are given by Eqs. (1) and (5) for $k_\parallel \neq 0$ and by Eq. (6) for $k_\parallel = 0$, which are used for kinetic simulation of the slab ITG turbulence in the present work. In order to obtain a corresponding closed fluid system, we need to express the parallel heat flow q_k in Eq. (4) in terms

of the lower-order moment fluid variables n_k, u_k, and T_k. In the H-P model [3], q_k is written in the diffusive form as

$$q_k = -n_0 \chi_{\parallel} i k_{\parallel} T_k, \tag{8}$$

where the parallel heat diffusivity is given by $\chi_{\parallel} = 2(2/\pi)^{1/2} v_t/|k_{\parallel}|$ with the ion thermal velocity $v_t \equiv (T_i/m_i)^{1/2}$. Then, Eqs. (2)–(5) for $k_{\parallel} \neq 0$, Eq. (7) for $k_{\parallel} = 0$, and Eq. (8) give a closed fluid system of equations in the H-P model. In the NCM, the parallel heat flow q_k in the unstable wave number region is given as

$$q_k = C_{Tk} n_0 v_t T_k + C_{uk} n_0 T_i u_k \qquad \text{(for linearly unstable modes)}, \tag{9}$$

while the dissipative closure relation as written in Eq. (8) should still be used in the stable wave number region. The real-valued coefficients C_{Tk} and C_{uk} are determined by requiring that the closure relation in Eq. (9) should exactly reproduce the kinetic dispersion relation [4].

3. SIMULATION RESULTS

Here, we consider a rectangular domain of $L_x \times L_y$ in the x-y plane with a uniform external magnetic field $\mathbf{B} = B(\hat{z} + \theta \hat{y})$ ($|\theta| \ll 1$), where $\hat{y}$ and $\hat{z}$ denote the unit vectors in the y- and z-directions, respectively. The system is assumed to be homogeneous in the z-direction ($\partial/\partial z = 0$). We employ the periodic boundary conditions in both x and y directions. Then, we can write $\mathbf{k} = k_x \hat{z} + k_y \hat{y} = 2\pi[(m/L_x)\hat{x} + (n/L_y)\hat{y}]$, $f_k = f_{m,n}$, and $\phi_k = \phi_{m,n}$ ($m, n = 0, \pm 1, \pm 2, \cdots$) and the parallel wave number is given by $k_{\parallel} = k_y \theta$. The background density and temperature gradients are assumed to exist in the x-direction, and their gradient scale lengths are given by $L_n = -(d \ln n_0/dx)^{-1} (> 0)$ and $L_T = -(d \ln T_i/dx)^{-1} (> 0)$, respectively.

Equations (1) and (5) for $k_{\parallel} \neq 0$ and (6) for $k_{\parallel} = 0$ are used as governing equations for the kinetic (or Vlasov) simulation, in which the fine-scale phase space structures such as the ballistic mode are resolved by employing 8,193 grid points for discretization of the velocity space, $-5 \leq v_{\parallel}/v_t \leq 5$ and using the nondissipative time-integration scheme [8]. For comparison to the kinetic simulation, two types of fluid simulations using different closure models are done. Both fluid simulations are based on Eqs. (2)–(5) for $k_{\parallel} \neq 0$ and Eq. (7) for $k_{\parallel} = 0$. However, one of them employs the NCM given by Eq. (9) for linearly unstable modes and the H-P dissipative closure given by Eq. (8) for linearly stable modes while the other uses the H-P closure for all modes. Here, for all simulations, we use the conditions $T_e/T_i = 1$, $\eta_i = L_n/L_T = 10$, $L_x = L_y = 20\pi\rho_i$ ($\rho_i \equiv v_t/\Omega_i$: the ion thermal gyroradius), and $\Theta \equiv \theta L_n/\rho_i = 2$.
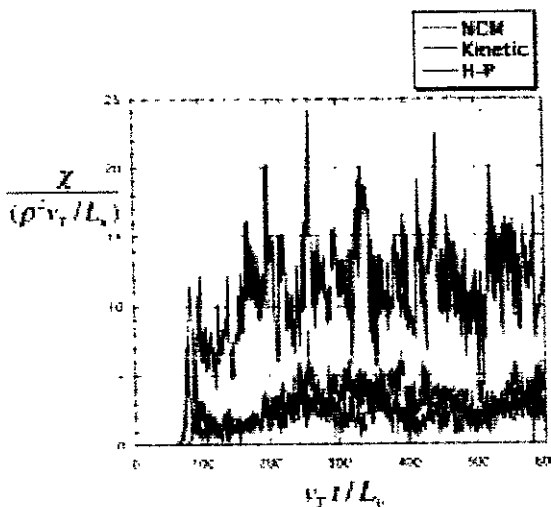
Figure 1 shows the normalized perpendicular heat diffusivity $\chi/(\rho_i^2 v_t/L_n)$ as a function of normalized time $v_t t/L_n$ obtained by the kinetic and fluid (NCM, H-P) simulations, where $\chi \equiv q_\perp \cdot \hat{x}/(n_0 T_i/L_T)$ and $q_\perp \equiv \frac{1}{2} n_0 \sum_k \text{Re}[T_k^* i(c/B) \mathbf{b} \times \mathbf{k} \Psi_k]$. In the saturated state of turbulence, χ obtained by the kinetic simulation is in a good agreement with χ from the fluid simulation using the NCM although χ obtained by the fluid simulation using the H-P closure for all modes are significantly larger than them.

Figure 2 shows the ion distribution function f_k divided by ϕ_k for $k_x = 0$ and $k_y = 0.4\rho_i^{-1}$ (which corresponds to the linearly most unstable mode). While $\text{Re}[f_k/\phi_k]$ at nonlinear or turbulent stages ($v_t t/L_n = 210, 400$) are similar to that of the linear

eigenfunction seen at an early stage $(v_t t/L_n = 50)$ except for superposition of fine structures due to the ballistic mode, $\mathrm{Im}[f_k/\phi_k]$ in the turbulent state has a different profile from that in the linear stage and oscillates around zero. Thus, the phases of f_k and $(n_k, u_k, T_k, q_k, \cdots)$ relative to ϕ_k may take either a positive or negative sign. This is similar to the case of the three-mode ITG problem [4] and the NCM is applicable to this situation more properly than the H-P model.

4. CONCLUSIONS

We have made a detailed comparison between kinetic and fluid simulations of the collisionless slab ITG turbulence. The validity of these closure models for quantitative prediction of the turbulent thermal transport is examined by comparing nonlinear results of the fluid simulations with those of the collisionless kinetic simulation of high accuracy. It is found from the kinetic simulation that the phase relation between the potential and the distribution function for the most unstable mode is different from that predicted by the linear unstable eigenfunction and is better described by the NCM than by the H-P model. This fact explains a reason for our simulation results that, in the steady turbulence state, the turbulent thermal diffusivity χ obtained by the H-P model is significantly larger than χ given by the NCM and that the latter is closer to χ found in the kinetic simulation.

REFERENCES

[1] A. M. Dimits, et al., Phys. Plasmas 7, 969 (2000).
[2] W. Horton, Rev. Mod. Phys. 71, 735 (1999).
[3] G. W. Hammett and F. W. Perkins, Phys. Rev. Lett. 64, 3019 (1990).
[4] H. Sugama, T.-H. Watanabe, and W. Horton, Phys. Plasmas 8, 2617 (2001).
[5] T.-H. Watanabe, H. Sugama, and T. Sato, Phys. Plasmas 7, 984 (2000).
[6] T.-H. Watanabe and H. Sugama, submitted to Phys. Plasmas.
[7] Z. Lin, et al., Phys. Plasmas 7, 1857 (2000).
[8] T.-H. Watanabe, H. Sugama, and T. Sato, J. Phys. Soc. Jpn. 70, 3565 (2001).

Fig.1. Normalized perpendicular heat diffusivity $\chi/(\rho_i^2 v_t/L_n)$ as a function of normalized time $v_t t/L_n$ obtained by the kinetic and fluid (NCM. H-P) simulations.
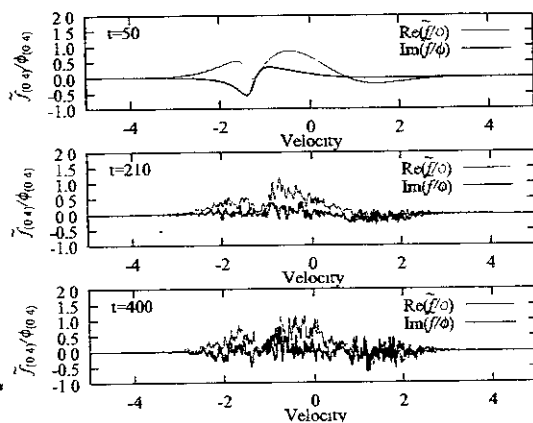
Fig.2. Ion distribution function f_k divided by ϕ_k at $v_t t/L_n = 50, 210, 400$ for $k_y = 0$ and $k_y = 0.4\rho_i^{-1}$ (which corresponds to the linearly most unstable mode).

Parameter Range of ICRF Heated Plasma on Large Helical Device

R.Kumazawa, T.Mutoh, T.Seki, K.Saito, T.Watari, M.Osakabe, S.Murakami, M.Sasao,
T.Watanabe. T.Yamamoto[1], Y.Torii[1], T.Notake[1], N.Takeuchi[1], H.Matsushita[1], T.Saida[2],
F.Shimpo, G.Nomura, M.Yokota, Zhao Yanping[3], H.Okada[4], M.Isobe, T.Ozaki,
K.Narihara, Y.Nagayama, S.Inagaki, S.Morita, A.V.Krasilnikov[5], H.Idei, S.Kubo,
K.Ohkubo, M.Sato, T.Shimozuma, Y.Yoshimura, K.Ikeda, Y.Oka, Y.Takeiri, K.Tsumori,
K.Nagaoka, N.Ashikawa, M.Emoto, H.Funaba, M.Goto, K.Ida, T.Kobuchi, Y.Liang[3],
S.Masuzaki, T.Minami, J.Miyazawa, T.Morisaki, S.Muto, Y.Nakamura, H.Nakanishi
Y.Narushima, K.Nishimura, N.Noda, S.Ohdachi, B.J.Peterson, A.Sagara S.Sakakibara,
R.Sakamoto, K.Sato, M.Shoji, H.Suzuki, K.Tanaka, K.Toi, T.Tokuzawa, K.Y.Watanabe,
I.Yamada, Y.Yoshinuma, K.Yamazaki, M.Yokoyama, K-Y.Watanabe, O.Kaneko,
K.Kawahata, A.Komori, N.Ohyabu, H.Yamada, S.Sudo, Y.Hamada, O.Motojima,
M.Fujiwara and LHD Experimental Group

National Institute for Fusion Science, Toki 509-5292, Japan
[1] Nagoya University, Nagoya 464-8601, Japan
[2] The Graduate University for Advanced Studies, Toki, Japan
[3] Institute of Plasma Physics Academia Sinica, Hefei 230031, P.R.China
[4] Kyoto University, Uji, Kyoto 611-0011, Japan
[5] Troitsk Institute for Innovating and Fusion Research (TRINITI), Troitsk, Russia

A difference in the confinement performance of high energy ions between the standard and the inward-shifted magnetic axis configurations on the Large Helical Device was experimentally observed in the ion cyclotron range of frequency (ICRF) heated plasma. It caused a difference in the transfer efficiency from high energy ions to a bulk plasma, which was compared with the Monte Carlo simulation result. The ratio of the stored energy of the high energy ions to that of the bulk plasma was measured employing an ICRF heating power modulation method.

1. Introduction

The ion cyclotron range of frequency (ICRF) heating has been successfully carried out on the Large Helical Device (LHD, the largest superconducting helical device, with R/a= 3.6~3.9m/0.6m, B=3T) [1-3]. A long pulse discharge of 2 minutes was achieved by ICRF heating only. The energy confinement time was found to be 1.5 times longer than International Stellarator Scaling 95 (ISS95) at the inward-shifted magnetic axis, i.e., R_{ax}=3.6m. This was derived from the fact that the displacement of deeply trapped particles in the helical ripple from the magnetic closed surface was reduced at R_{ax}=3.6m. The phenomenon is thought to be similar to that of the high energy ions accelerated by an RF electric field; the confinement of high energy ions is better and the energy transfer efficiency is expected to be higher than that at the standard configuration, i.e., R_{ax}=3.75m. The difference between the magnetic configurations was examined measuring the energy distribution of high energy ions.

The technique of RF power modulation was used to evaluate energy confinement time and heating efficiency [4]. This method was employed to deduce the ratio of the stored energy of high energy ions to the bulk plasma. It was determined from two phase differences; one was between the total plasma stored energy and the bulk plasma stored energy, and the other was a phase difference between the modulated RF power and the total plasma stored energy.

In this paper the confinement of high energy ions is discussed using experimental data obtained in a series of plasma discharges at the standard (R_{ax}=3.75m) and the inward-shifted (R_{ax}=3.6m) magnetic configurations. Then it is compared with the result obtained in the Monte Carlo simulation [5]. Then the measured ratio of the stored energy was reported for the plasma discharge with an ICRF power modulation method.

2. Experimental results

Tail temperature and transfer efficiency

A plasma consisting of He ions as the majority and H ions as the minority was employed in the series of experiments. The relation between tail temperature T_{tail} and effective temperature T_{eff} is plotted in Fig.1. T_{tail} was measured using a fast-neutral analyzer (Si-FNA) with an electrically cooled Silicon-diode detector [6] and the charge exchange process with ⁻He [7]. The Si-FNA measured ions with the perpendicular energy to the magnetic field line. T_{eff} was calculated using plasma parameters (n_H, n_e and T_e are the minority ion density, the electron density and the temperature) and the ICRF heating power P_A in the following equation [8];

$$T_{eff} \approx A \frac{\eta_H (n_H / n_e) P_A T_e^{3/2}}{(n_H / n_e) n_e^2 V_H}), \quad T_{tail} \approx \frac{\tau_E^{tail}}{\tau_s / 2} T_{eff}, \quad \frac{1}{\tau_E^{tail}} = \frac{1}{\tau_s / 2} + \frac{1}{\tau_E^{loss}}$$

Here η_H and V_H are the heating efficiency and the minority heating volume [9]. A wide range of T_{eff}, to be precise from 10keV to 200keV was found at R_{ax}=3.75m; however the range of T_{eff} at R_{ax}=3.6m was from 10 to 60keV,which was caused by an insufficient reduction of the minority ion density. A saturation of T_{tail} was found at R_{ax}=3.75m; this reflects a shorter energy loss time. When the energy loss time τ_E^{loss} was taken into account and the tail energy time τ_E^{tail} was determined, T_{tail} was calculated using the above equation.
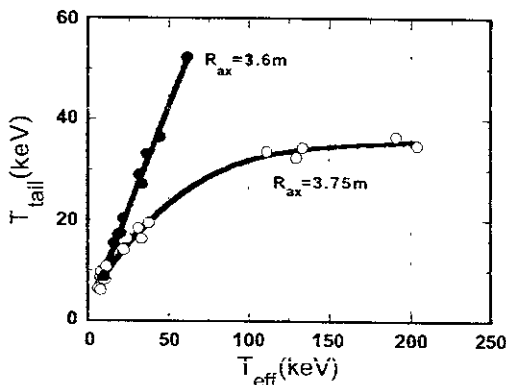
Fig.1 Relation between T_{tail} and T_{eff} at
R_{ax}=3.6m and 3.75m.
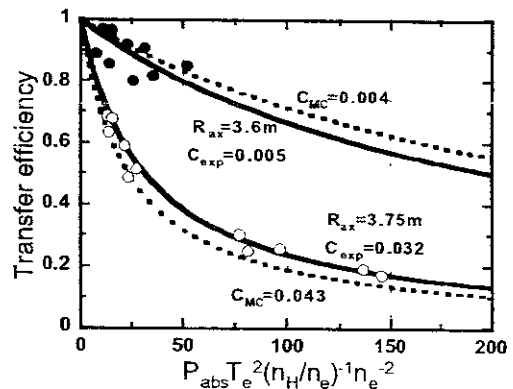
Fig.2 Dependence of transfer efficiency on
$P_{abs} T_e^2 (n_H/n_e)^{-1} n_e^{-2}$ at R_{ax}=3.6m and 3.75m.

The transfer efficiency η_{trns} was defined as what fraction of the energy flows from high energy ions to the bulk plasma;

$$\eta_{trns} = \frac{P_{trns}}{P_{abs}} = \frac{T_{tail}}{T_{eff}} = \frac{1}{1 + CP_{abs}T_e^2 (n_H / n_e)^{-1} n_e^{-2}}$$

It was also expressed as the ratio of T_{tail} to T_{eff}. In the Monte Carlo simulation η_{trns} was scaled as in the above equation. Here the numerical factor C depends on the magnetic axis position and the magnetic strength. It was determined using experimental data for two cases as shown in Fig. 2, where the abscissa is $P_{abs}T_e^2(n_H/n_e)^{-1}n_e^{-2}$. C_{exp} was determined to be 0.032 at R_{ax}=3.75m and 0.005 at R_{ax}=3.6m, respectively. C_{MC} in the Monte Carlo simulation was also 0.043 at R_{ax}=3.75m and 0.004 at R_{ax}=3.60m [5].

High energy tail fraction

An analysis of the plasma discharge with the RF power modulation predicts a ratio of the stored energy of high energy ions to that of the bulk plasma using two phase differences. One was between the bulk plasma W_b and the total plasma stored energy W_p including the store energy of high energy ions, and the other was between the modulated RF power P_A and W_p. The relations between δW_p and δW_b, and between δP_A and δW_p are expressed in the following complex equation [4],

$$\frac{\delta W_P}{\delta W_b} = 1 + \frac{3}{2}\frac{AR_{tb}}{\eta_{trns}} + i\frac{3}{2}\omega\tau_{se0}/2$$

$$\frac{\delta W_P}{\delta P_A} = \eta_{trns}\tau_{se0}/2\eta_0 \frac{1 + \frac{3}{2}(i\omega\tau_{se0}/2 + \frac{AR_{tb}}{\eta_{trns}})}{-BR_{tb} + (i\omega\eta_{trns}\tau_{se0}/2 + 1)(i\omega\tau_{se0}/2 + \frac{AR_{tb}}{\eta_{trns}})}$$

$$A = \frac{3}{2} + (1 - \beta), \quad B = \frac{\eta' T_0}{\eta_0} + \frac{3}{2}$$

ω and β are the applied modulation frequency and a numerical factor derived from the dependence of the energy confinement time on the temperature; β =-1.44 at ISS95. η_0 is the heating efficiency and η' is its derivative of temperature [4]. The phase difference between δW_p and the bulk plasma was θ_{pb} and the phase difference between δP_A and δW_p was θ_{pA}; δW_p was used as the diamagnetic loop and δW_b was used as ECE signal because of no observed modulated electron density. The time evolutions of P_A, W_p and W_b in the case of the low electron density plasma with n_e=2~3x10^{18}m^{-3} are shown in Fig. 3(a). The averaged RF power was P_A=270kW and the modulation rate was 30%. θ_{pb} and θ_{pA} were 20 degrees and -56 degrees at t=1.0s and n_e=2.2x10^{18}m^{-3}, and at t=2.0s and the higher electron density, i.e.,

$n_e=3\times10^{18}$m^{-3}, θ_{pb} and θ_{pA} were 11 degrees and -36 degrees as shown in Fig.3(b). The measured ratio of W_t to W_b was deduced to be R_{tb} =0.4~0.2 using measured phases in the above equation. This value was assessed in another way by using the electron slowing down time $\tau_s/2$ and half of the ISS95 confinement time at the collisionless regime in $R_{ax}=3.75$m [10]. The ratio of $\tau_s/2/\tau_{E0}/2$ was calculated to be 0.4~0.2.
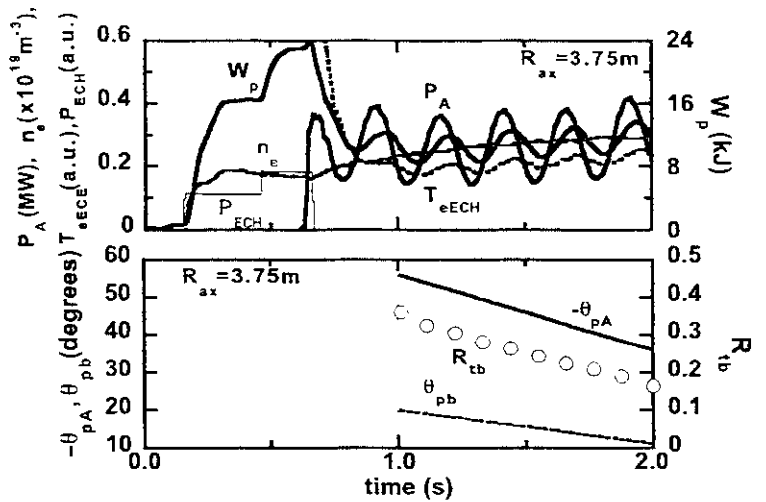
Fig.3(a) Time evolutions of P_A,W_p and T_{eECE} at $R_{ax}=3.75$m.
(b) Time evolutions of measured phase difference θ_{pA} and θ_{pb} and R_{tb}.

3. Summary

The ICRF heating experiments on the LHD was carried out successfully. The confinement characteristics of high energy ions accelerated by ICRF electric field were examined measuring the energy distribution with the Si-diode detector. As predicted in the orbit calculation, the better confinement of the high energy ions at the inward-shifted configuration compared with that at the standard configuration was proved. These experimental data agree with the transfer efficiency obtained in the Monte Carlo simulation.

The ratio of the stored energy of the high energy component W_t to that of the bulk plasma W_b was measured in the ICRF power modulated plasma. The ratio agreed with that deduced from the ratio of the electron slowing down time to the energy confinement time.

Acknowledgement

References
[1] Mutoh T et al Phys. Rev. Lett. 8 5 4530
[2] Watari T et al Nucl. Fusion 4 1 325
[3] Kumazawa R et al Phys. Plasmas 8 2139
[4] Torii Y et al Plasma Phys. Controlled Fusion 4 3 1191
[5] Murakami S et al Nucl. Fusion 3 9 1165
[6] Osakabe M et.al Rev. of Scientific Inst. 7 2 590 & 788
[7] Krashilnikov et al Nucl. Fusion 4 2 759
[8] Stix T H Nuclear Fusion 1 5(1975) 737
[9] Saito K et al Nucl. Fusion 4 1 1021
[10] Yamada H et al Plasma Phys. Controlled Fusion 4 3 A55

Two Dimensional Soft-X ray and AXUVD Tomography Based on Magnetic Flux Surfaces

Y. Liu[1], A.Yu.Kostrioukov[3], K. Nagasaki[2], Y. D. Pan[1], B.J.Peterson[3]

[1]South Western Institute of Physics, Chengdu, China

[2]Institute of Advanced Energy, Kyoto University, Japan

[3]National Institute for Fusion Science, Japan

1. Introduction

A tomographic algorithm taking magnetic flux surfaces into account is used to reconstruct an emission image. Improvement of the quality of reconstructed images has been obtained using a feedback technique to compensate numerical errors. This tomography technique has been applied in soft x-ray measurements on HL-1M Tokamak and Heliotron J, and used for plasma radiation imaging on the Large Helical Device (LHD)[1] by using AXUVD (bolometer like semi conductive detectors) arrays [2].

2. Method used for soft X-ray and bolometric inversion

2.1 Dividing and expansion under the basis of vacuum flux surfaces

The basic principle of tomography is to reconstruct the emitted radiation from a plasma cross-section along a large number of collimated chord measurements. The reconstruction algorithm employed here is so-called hybrid methods [3]. We divide the emitting region into annular areas under the basis of real magnetic flux contours. These annular areas can be considered as pixels, as shown in Fig.1. Line integrals

$f(p_i,\varphi_i)$ can accurately be represented by a summation of the contribution, g_k, from each pixel along the line of sight

$$f(p_i,\varphi_i) = \int_{L_i} g(r,\theta)dL \approx \sum_k a_{ik} g_k \quad (1)$$

where p is the distance from the origin to the tangential point of line of sight to the corresponding surface, the chord angle φ is the polar co-ordinate of the point of tangency. Equation (1) is equivalent to have chosen a series of piecewise linear functions to represent the detected signals. These functions vanish at plasma boundary, i.e., they satisfy the basic requirement of orthonormality in the same way as Bessel functions. The local emissivity in a pixel, g_k, can be solved by using a 'peeling away' technique given in Ref[4].

To model the variation of emissivity within a pixel in the angular direction, we expand the emissivity on each pixel in Fourier
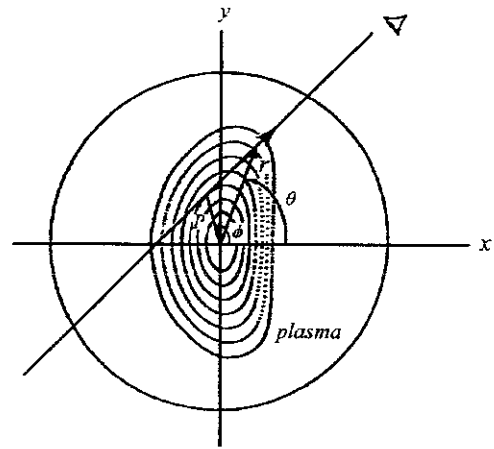
Fig.1. Co-ordinate system for reconstruction of a 2-D image. The emitting region can be divided into annular pixels with real magnetic

series. Then the local emissivity within a pixel is:

$$g_k = g_{k0} + \sum_m g'_{km} \sin m\theta + g'_{km} \cos m\theta \qquad (2)$$

The number of observation directions limits the number of Fourier modes. Higher modes as far as $\sin 2\,\theta$ mode are neglected if two existing arrays are used.

2.2 Feedback technique

To reduce the error and prevent the error from propagating into the inner pixel, we use a feedback technique to compensate for the error at each pixel. Since the Radon transform for emission (Eq.(1))is linear, if the inversion procedure is represented by the operator $\Re$, such that $g = \Re(f)$, the pseudo signals recalculated from the reconstructed emissivity function g' is given by $f' = \Re^{-1}(g')$, then:

$$g' - g = \Re(f') - \Re(f) = \Re(f' - f) \qquad (3)$$

This leads to a more accurate solution:

$$g = g' - \Re(f' - f) \qquad (4)$$

In other words, the difference between the measured and reconstructed line-integrated signals is fed back as an input data for the inversion process. If the reconstruction itself is stable, the feed back process makes the difference between experimental and reconstructed chord integrated data negligible.

3. Numerical Test

The technique of the reconstruction is examined numerically using a perturbed structure. The source function has a circular hot spot over flat region in the center [5].
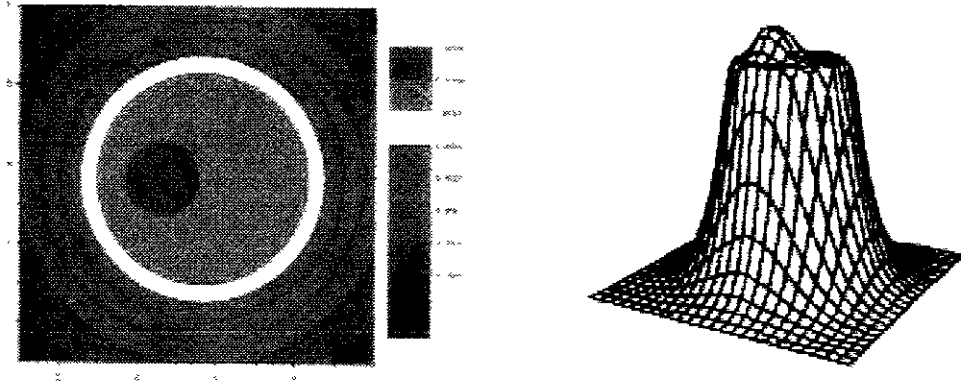
Fig.2. (a) Contour plot of the test source function and (b) surface plot of the

Fig.2 shows the contour plot of the test source function and the hidden-line perspective plot of the reconstructed image for the case of small size hot spot ($r_{spot} \approx 10\%$ of r_s).

4. Application to AXUVD measurement on LHD

Fig.3 shows two AXUVD arrays (20 channels each) installed on a semi-tangential cross-section in LHD. Part of the emitting volume was only seen from the right side (4-O array). The plasma shape strongly depends on the magnetic axis position, R_{ax}. For smaller R_{ax} the part not seen from above was bigger, which made the tomography procedure more difficult. In addition, high spatial resolution requirement near the boundary, strong poloidal asymmetries in radiation distribution and the far deviation from circular shape in the edge region make a serious challenge for the inversion technology.
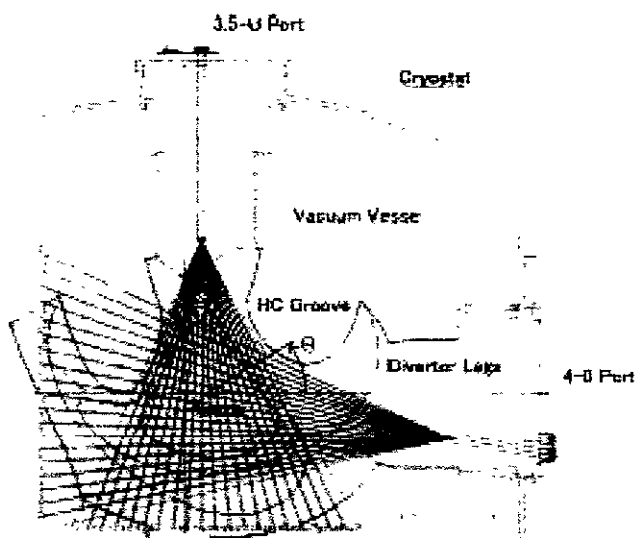
Fig.3. Lines of sight of the bolometric tomography on LHD.
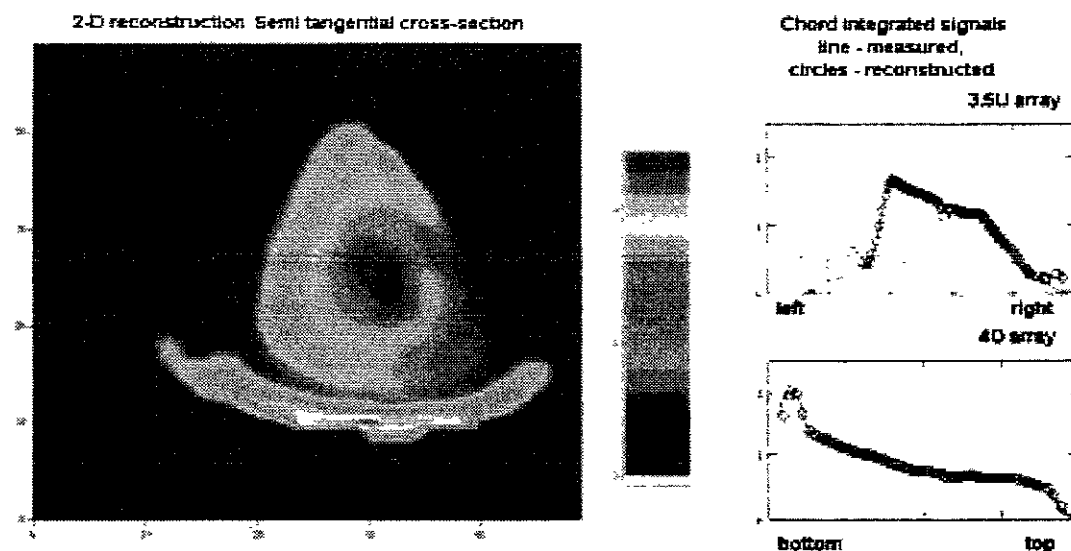
Fig. 4. 2-D bolometric emissivity profile reconstruction in Shot 31721 t=2 s. The bright region at the bottom is due to 3.5L gas puffing.

The tomography algorithm described above provided reasonable two-dimensional profiles of plasma emission and a good agreement between experimental and simulated chord integrated emission for different conditions. Fig.4 shows a hollow profile with additional peripheral emission caused by the gas puffing from the bottom nozzle. Small differences between reconstructed and measured chord integrated profiles (4O array) were caused by reconstruction artifacts. Fig.5 shows the emissivity for the same discharge at the moment when the gas puffing was off.
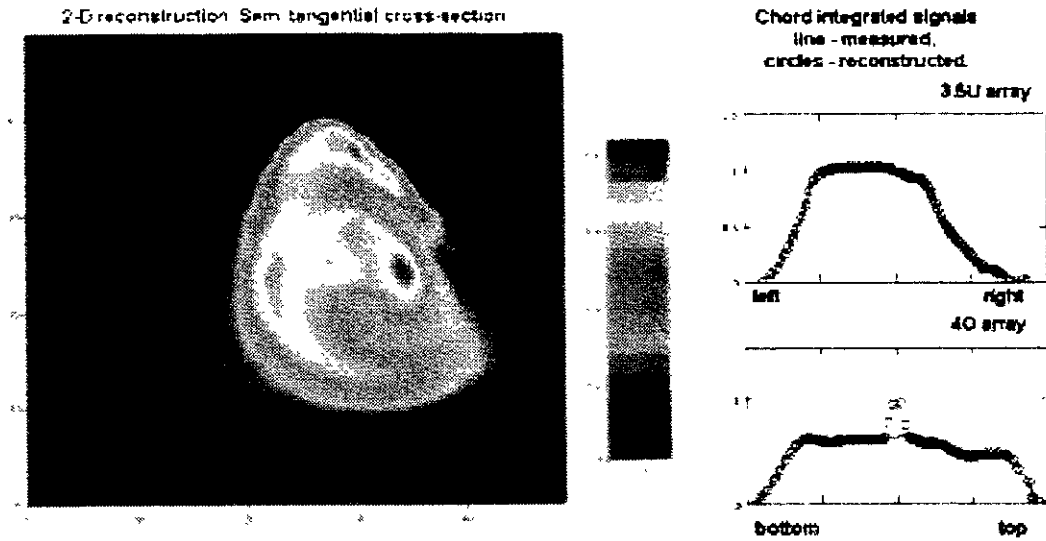
Fig. 5. 2-D emissivity bolometric profile reconstruction, shot 31721, t=3.5 s.
The gas puffing was off.

5. Discussion

The main advantage of the method employed is that the boundary condition is naturally met by solving the equation in the outermost pixel. Taking the complicated real plasma shape into account makes the algorithm start from a grid that is closer to the true plasma radiation contours. It is suitable to be applied in measurements of soft x ray and total radiation on the LHD and Heliotron J with widely arbitrary cross sections. Furthermore, we modified this tomographic algorithm with a feedback procedure. As a result, the 2-D technique was powerful enough to provide reasonable images in the most of the cases. However, since the number of detector arrays is limited, only a finite number of Fourier components can be used in the expansion. In some cases (strong asymmetry or contours of constant radiation emissivity deviate far from magnetic flux surfaces) the reconstruction was not so reasonable, i.e. the difference between experimental and reconstructed chord integrated data drastically diverges in the central part of the image.

6.Conclusions

Numerical test and the results of the 2-D tomography technique applied to the experimental data showed that the algorithm is powerful enough to reconstruct complicated asymmetric emissivity distribution.

References

[1] A.Komori et al., Plasma Phys. Control Fusion 42 (2000) 1165.

[2] A.Yu.Kostrioukov et al., Submitted to Rev. Sci. Instrum., 2002.

[3] P.Smeulders, Nucl.Fusion 26, 267 (1986).

[4] R.S.Granetz, P.Smeulders, Nucl.Fusion28, 457 (1988)

[5] Y.Nagayama et al., Rev.Sci.Instrum.65, 3415 (1994)